Integration of electro-chemical FET-based sensors
in silicon- and polymer- based organs-on-chip

Anna-Danai Galiti

Delft University of Technology

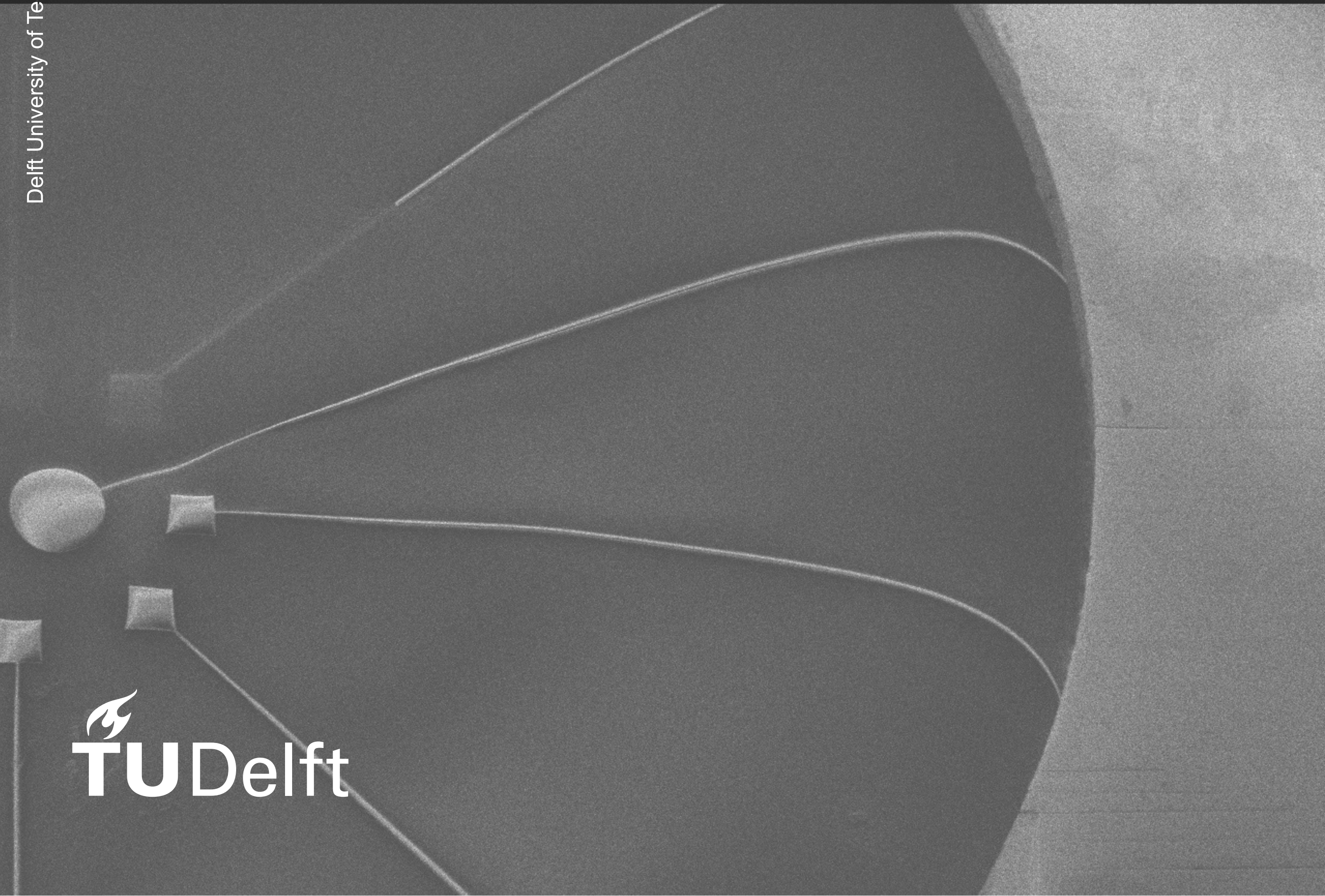

Integration of electro-chemical FET-based sensors

in silicon- and polymer- based organs-on-chip

by

Anna-Danai Galiti

to obtain the degree of Master of Science
at the Delft University of Technology,
to be defended publicly on Wednesday April 21, 2021 at 13:30 AM.

Student number:	4936841
Supervisors:	dr. Massimo Mastrangeli
	Hande Aydogmus

This thesis is confidential and cannot be made public until April 15, 2022.

TU Delft

Abstract

Currently, preclinical drug testing and disease modelling are based on static cell cultures and animal models that often fail at predicting the human pathophysiology. Alternatively, Organ-on-Chips (OoCs), dynamic microphysiological platforms, can be employed to recapitulate organ functions and mimic the cell's microphysiological environment. OoCs also promote the study of transport mechanisms and tissue barriers, such as the blood-brain barrier (BBB), a critical structure responsible for the regulation of the brain fluid microenvironment. Monitoring the ionic environment of the BBB and its variation due to the effect of drug testing is thus critical, indicating the need for integrated sensing elements.

The rapid evolution of silicon technology and microelectronics has contributed to the development of field-effect transistors (FETs) for use as biosensors, ever since their first appearance in the 1970s. Such devices can provide real-time and label-free detection of target bioanalytes with high sensitivity. There are several types of FET-based biosensors based on different geometries and utilising various materials, but currently, no optimal consensus for a biocompatible FET-based biosensor with high sensitivity and reliability has been established.

In the present thesis, floating gate FET-based sensors implementing flexible electrodes suspended on an optically transparent sensing area were designed and successfully fabricated for application on blood-brain barrier ion environment monitoring. Before the designing process, a thorough literature study on FET-based alternative solutions compatible with the BBB-on-chip application gave an overview of the available technology. It also indicated a lack of theoretical background behind the sensor's operation mechanisms. To face this issue, theoretical and simulation models were created based on the floating-gate MOSFET operation. Additionally, the electrical double layer (EDL) role, only included in models in the presence of a reference electrode is examined.

The novelty of the sensor configuration lies with the implementation of an additional planar electrode in the sensing area of the OoC, tackling the issue of the external reference electrode use. Possible models describing the interaction between the additional electrode and the FGFET are created for comparison with experimental data. The novel sensor is designed aiming towards optimised sensitivity while also examining the effect of different configurations on the behaviour of the planar electrode. Dual-gate operation of the fabricated sensor in electrolyte indicates an increase of the output signal up to 16% compared to single-gate operation. In contrast to model predictions, the sensor does not operate in saturation mode, rendering the mathematical models ineffective. The simulation-based model is suggested for following applications after fine-tuning based on experimental data. Overall, a strong basis of the theoretical background was established, making ground for future studies.

Preface

The present thesis marks the completion of my master studies at TU Delft. This project, starting in April 2020, found the world changing and me, fortunately enough, trapped with my family in Greece. As a journey, with its ups and downs, it gave me adventures and a lot of knowledge. It was an amazing learning experience and I would not miss the chance of thanking all the people who despite the distance, directly or indirectly, pushed this project forward.

First of all, I would like to extend my most sincere gratitude to my supervisor Massimo Mastrangeli for giving me the opportunity of working on this exciting project and for supporting me every step of the way. I would also like to thank my daily supervisor for her guidance. Thank you Hande for your never-ending patience and pushing me to want to learn more, I could have hardly asked for a better (or cooler) mentor.

I would also like to express my gratitude towards the personnel and my colleagues at EKL for their advises and their help, and even in some cases the fun we had together. Here, I would like to give my special thanks to my little Shriya and Merlin for always being there and giving me some much needed respite.

This journey started with the support of my family and ends with the support of my closest friends. In no particular order, thank you Sevasti, Ntenia, Kosta, Dimitri, Fani, Entela, Kiriako, Sevda and many many more for being a part of my life and making me smile. You all hold a very special place in my heart. Finally, I should not forget to thank my parents and brother for the continuous support during my long studies, their bad jokes and their love.

Thank you all for showing me that hard work yields results and making me believe in myself.

Anna-Danai Galiti
Delft, April 2021

Contents

List of Figures

List of Tables

1

Introduction

In the rapidly evolving domain of medical technology, advancements in sensing applications play a paramount role in ensuring people's wellbeing. Bioelectronic interfaces are commonly used for medical and pharmaceutical applications, indicating the high demand for biosensors. Especially in the field of drug testing, the critical monitoring of the microphysiological environment and the recording of cell activity are the authority of biosensors. Approximately a century ago, the first two-dimensional cell cultures were developed, but failed to recapitulate tissue-specific behaviour, thus leading to more complex models for drug testing. The other big player in the field, animal-based models, also exhibit limited drug effect predictivity mainly due to the phylogenetic distance between said models and human physiology. Microfluidic organs-on-chip (OoCs) are ambitious platforms that combine cell cultures in a dynamic environment with physiological cues, while supporting in-situ monitoring with biosensors to overcome the limitations of conventional methodologies in preclinical drug testing.

This thesis illustrates the process of developing an organ-on-chip (OoC) from concept to fabrication and characterisation, with an end-point application in blood-brain barrier (BBB) tissue monitoring. The OoC implements electrochemical sensors on the same platform, based on the field-effect transistor (FET) configuration, a sophisticated device that can be utilised for measuring biochemical signals. Unfortunately, the first part of the project had to be carried out remotely due to unforeseen obstacles as a result of the COVID19 pandemic, leading to an extended literature and theoretical study, while the later on-field work was also limited due to pandemic-related restrictions. The fabrication took place at the Else Kooi Lab (EKL) cleanroom facilities of the Electrical Engineering, Mathematics and Computer Science (EEMCS) Department, at TU Delft.

The current chapter serves as an introduction to the OoC state-of-the-art and introduces the essential background behind the BBB physiological anatomy and function. Subsequently, the problem statement of the present work is described, followed by its translation to concrete requirements and research questions, which constitute the target objective of the thesis. Finally, the outline of this report is given.

1.1. Organ-on-Chip

Two-dimensional cell cultures were the first platforms for preclinical drug testing. Problems associated with these structures, such as the inability to recapitulate tissue specific behaviour and failure at in-vivo drug effect prediction, led to the development of more complex models. The more recent three-dimensional (3D) cell cultures allow better cell-to-cell interaction, accompanied by higher drug effect predictability. However, 3D cell cultures fail at forming tissue interfaces comprised of different types of cells, such as endothelial cells in contact with connective tissue. The absence of physiological cues in the aforementioned models is a critical flaw. 3D cultures lack mechanical and electrical stimuli as well as the interaction with fluid elements mimicking the function of the blood and immune system [1].

On the path towards higher physiological relevance, as illustrated in Fig 1.1, tissue samples are also used for preclinical drug testing, with animal-based models being the most relevant method. Animal-

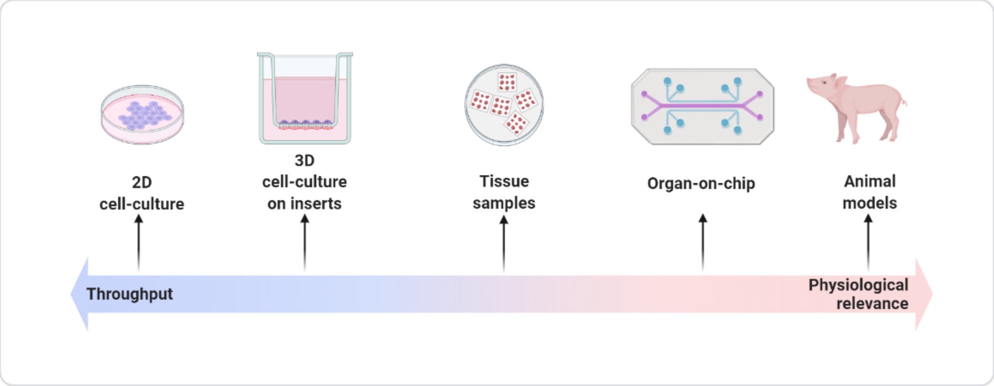

Figure 1.1: Schematic illustrating the platforms finding application in preclinical drug testing studies and presented from the less towards the more physiologically relevant. Created with BioRender.com.

based drug testing is a common tool during drug assessment as it replicates both single- and multi-organ function [2]. However, the biosimilarity gap between animal models and human physiology results in significant drug failure on human trials [3]. Commonly, animal models fail at predicting adverse effects, while also drug-side effects demonstrated on animal models do not necessarily translate into adverse effects on the human organism. These false positive and false negative results indicate the need for a novel strategy towards more effective drug testing.

Microfluidic organs-on-chip (OOC) pursue combining the extracellular cues of organ systems with 3D human cell cultures to optimise preclinical drug testing. By implementing human cells, it is possible to mimic patient-specific pathophysiology in vitro and work towards personalised treatment [1]. Thus, OOCs can check both drug effectiveness for specific treatments and the absence of adverse effects, such as toxicologic events. An overview of the OoC application towards personalised medicine is illustrated in Fig 1.2.

Cells are cultured inside continuously perfused, microfluidic chambers, incorporating physiologically relevant stimuli, such as fluid shear stress and mechanical compression. The complex mechanical environment of tissues is replicated on OOC platforms in vitro, aiming at recapitulating the human physiology in minimal functional units in a controlled manner, but not in a whole-organ level. Electrical physiological cues can also be replicated on these in-vitro platforms, while also the interaction between different cell types can be promoted [2], [4]. Parallel microchannels can be separated by porous substrates/membranes, acting as the skeleton for the formation of cell interfaces. Different cell types can be cultured on either side of the membrane and thus OOCs allow the study of transport mechanisms and tissue barriers, such as the BBB [1].

Currently, the function of OOCs is based on organ- or tissue-architecture and study pathologies in a short time frame (less than approximately one month). Physiologically, some functions such as cognitive behaviour between brain cells and the mechanical function of connective tissue are based on macroscale architectures and thus, cannot be modelled on a chip. OOCs can however include small organ sections which can respond to chemical and electrical stimuli, and recapitulate specific organ-level functions [1].

By imitating the physiology of functional tissue, an interesting scenario arises for connecting individual OOCs through microfluidic vasculature. This way, various in vitro tissue-specific models can be linked to form wider human subsystems, possibly allowing off-target drug toxicity identification during preclinical studies. This idea for a “human-body-on-a-chip” introduces an extra level of biological relevance by using connective pathways between individual organ models, which can also extend the viability of the system and imitate human homeostatic mechanisms [3]. The inclusion of complex biological systems, such as the immune or endocrine system, in a “human-body-on-a-chip” will offer a significant advantage

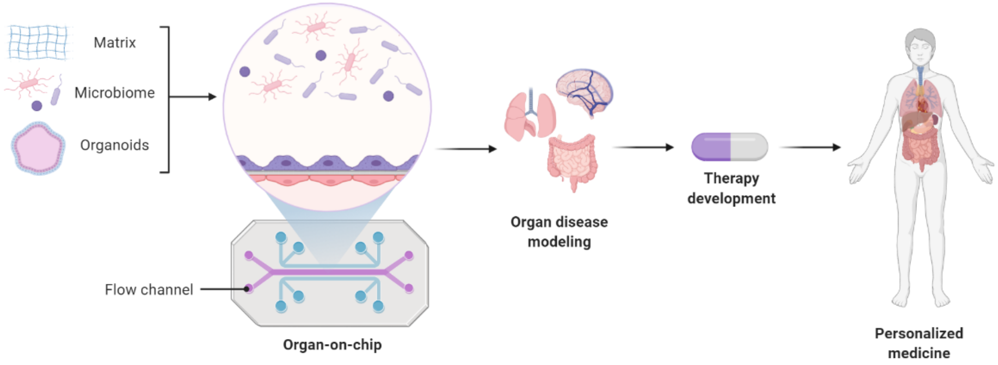

Figure 1.2: Illustration showing the path of OoCs towards personalized medicine. Created with BioRender.com.

over animal models but remains quite challenging. Up to this point, controlling cell interactions on OOCs to maintain the structure and function of one unit has already proven a significant challenge [2].

OOCs come in a combination of materials, they are usually glass- and/or silicon-based, accompanied by polymers, ceramics, or biological materials, depending on the requirements of the studied tissue. The original OOC fabrication method was based on a modified photolithography process for microchip fabrication, and thus came the “chip” part of the “organ-on-chip” name. Photolithography allows the formation of various patterns that are also compatible with cell structures, which is why soft lithography is commonly used for microfluidic structure fabrication. The patterns are initially designed on silicon chips and then used as a mould for flexible materials. Liquid polymers are poured into the silicone mould, and after polymerisation a polymer stamp is formed. Most commonly, poly-dimethylsiloxane or PDMS, a highly compliant and deformable material is used for biocompatible scaffolds and microfluidic systems. PDMS is optically transparent, allowing real-time monitoring of cell cultures and fluid flow and oxygen permeable, making it an ideal candidate for biological applications [1], [3].

Nevertheless, the microfabrication of OoCs can be time-consuming due to the various process steps and the manual assembly, especially in the case of polymers [5]. However, this fabrication allows the integration of sensors that can monitor and gather data form cell cultures and their environment, in contrast with 3D cell cultures which have been proved challenging to monitor. It is important to note that at this point, OoC technology can not replace animal models, but can yield additional data towards a better insight on drug effectiveness and improved preclinical drug testing methods.

1.2. Blood-Brain Barrier

The central nervous system (CNS) function heavily relies on the highly controlled fluid microenvironment of the brain. The well-regulated chemical composition and ion concentration in this microenvironment are critical for effective neural signalling [6]. Three protective mechanisms regulate the internal environment of the brain: the blood-brain barrier (BBB), the blood-cerebrospinal fluid barrier (BCSFB) and the arachnoid barrier. The main interface for blood-CNS exchange is the blood-brain barrier rendering it responsible for ion balance, nutrient transport, and inhibition of unwanted substances. This barrier was first studied by Paul Ehrlich in 1885, and its critical function led to numerous following studies towards identifying the BBB structure and function.

The main building blocks of the BBB are endothelial cells that form the brain capillary walls. As shown in the capillary cross-section of Fig 1.3, endothelial cells fully enclose the circumference of the capillary, while tightly connected to each other, forming “tight junctions” that impede the transfer of solutes from the blood plasma to the brain extracellular fluid. Other types of cells are also part of the barrier’s structure, forcing bloodborne substances to pass through two more cell layers before reaching the neural tissue. A thick lamina layer surrounds each capillary and astrocyte ‘feet’ connect to the capillaries [7]. The reduced permeation of solutes from the BBB to the cerebrospinal fluid is accompanied by

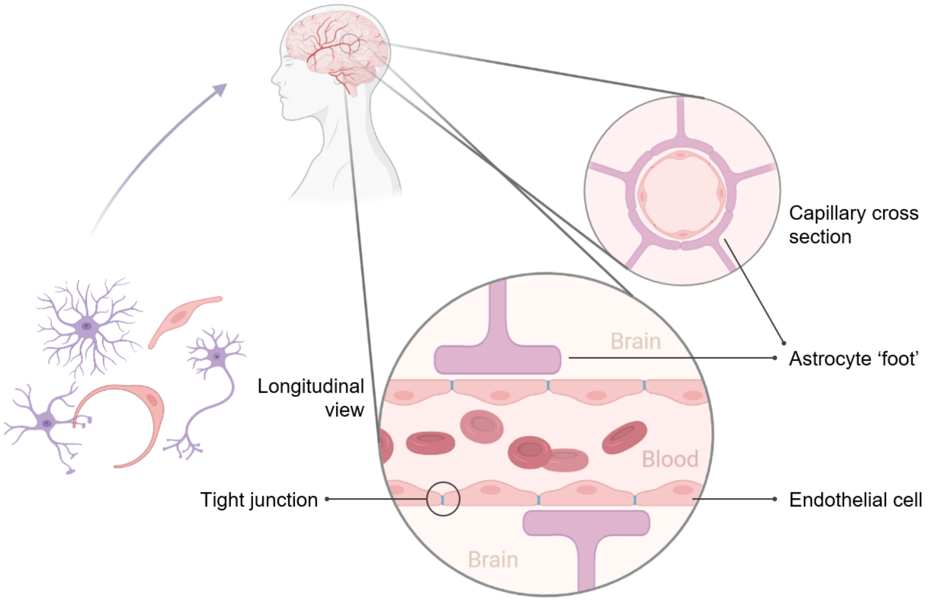

Figure 1.3: Illustration of the BBB anatomy including the various types of cells. Created with BioRender.com.

restricted ion transfer. This restricted movement of ions or charged molecules through the barrier results in high in-vivo electrical resistance (approximately 1800 Ωcm^2 [8]), which can be measured as an indicator of barrier tightness. Transendothelial electrical resistance or TEER measurements provide a quick, non-invasive and possibly real-time barrier assessment without the use of labels, such as fluorescent dyes.

The tight endothelial junctions form a physical barrier for bloodborne substances, but existing mechanisms allow the transportation of essential solutes, making BBB a metabolic barrier. To maintain a constant microenvironment for the CNS, BBB is a dynamic, highly selective barrier. Some substances like water, respiratory gases and essential nutrients pass through the barrier to the neural tissue, fulfilling the considerable neural metabolic demands. Fat-soluble molecules can also enter neurons, explaining how substances like nicotine, alcohol and anaesthetics affect the neural system. On the contrary, water-soluble substances like some proteins, toxins, metabolic wastes, and most pharmaceutical drugs are prohibited from entering neural tissue. The concentration of critical ions like H^+ , Ca^{2+} and Mg^{2+} is actively regulated by the BBB and disruption of physiological BBB function can lead to ionic imbalance. The concentrations of some solutes on the two sides of the barrier are shown in Table 1.1.

Table 1.1: Typical concentrations of some selected solutes in plasma and cerebrospinal fluid (CSF), as extracted from Begley et al. [9]

Solute	**Units**	**Plasma**	**CSF**	**Ratio**
Na^+	mM	140	141	1
K^+	mM	4.6	2.9	0.63
Ca^{++}	mM	5.0	2.5	0.5
Mg^{++}	mM	1.7	2.4	1.4
Cl^-	mM	101	124	1.23
$Glucose$	mM	5.0	3.2	0.6
$Albumin$	mg/ml	42	0.192	0.005
$Immunoglobulin(IgG)$	mg/ml	9.87	0.012	0.001
pH		7.4	7.3	

Barrier dysfunctions might affect the regulation of the neural microenvironment and contribute to a developing pathology. In most cases, the correlation between BBB impediment and pathology is not necessarily cause and effect, like in Alzheimer's and Parkinson's disease. However, BBB dysfunction is associated with numerous other CNS pathologies. Change in the permeability of the barrier due to tight junction openings, breakdowns or transport mechanism impediments is commonly associated with diseases such as multiple sclerosis (MS), hypoxia, ischemia and diabetes. Reversibly, BBB abnormalities can result from a CNS pathology like ischemic stroke and traumatic brain injury. Monitoring of the barrier function as well as identifying sites of disturbance can be critical for compromising developing neurological disorders and can form a crucial strategy for brain-focused drug therapy [6], [10], [11].

Some scientific groups studied the combination of OoC platforms with the BBB and focused on the microfluidic chamber configuration, cultured cell type, shear stress application and TEER measurements. The lack of monitoring the cell environment, first on the basis of ion exchange between different cell types, can be overcomed by integrating electrochemical sensors. Complex and critical biological structures like the BBB indicate the need for sensing elements to achieve a deeper understanding of physiological tissue interactions.

1.3. Problem Definition

Targeting the BBB that selectively regulates the passage of analytes and drugs into the nervous system, an electrochemical sensor platform that will monitor the effect of drugs on the BBB microphysiological ionic environment is developed. In a previous effort, floating-gate based FET sensors were integrated into an OoC platform following standard CMOS process technology for application in monitoring ion exchange in cell culture environments [12]. This OoC platform, whose structure is shown in Fig 1.4, implements eight FET-based sensors, four n-type and for p-type, to produce output as a response to both positive and negative sensing charges. Each sensor/transistor system comprises two basic parts, the sensing area and the transducing section of the device. The active device contains the electrical parts and lays on the Si substrate, while an electrode extension connected to the transducer is suspended on the PDMS sensing area. A sensing well is formed in the middle of the chip composed of PDMS, thus providing a flexible and optically transparent platform. All eight transistors lay their extensions on the same sensing area, where cell culturing is supported.

For this project, the basis established by the previous OoC platform is used as a stepping stone for the development of the novel BBB-on-chip. Emphasis is given on the theoretical background behind the underlying mechanisms of the sensor's operation, for the creation of models that effectively predict such behaviour. Said models are used for the determination of the final design. The integration of a planar electrode on the flexible sensing well and the study of its interaction with the FGFET asserts the novelty of the sensor.

1.3.1. Requirements

In order for the sensor platform to be compatible with OoC applications, and thus for interaction with cell cultures in physiological media, the following criteria were chosen:

Biocompatibility: The sensor must be able to operate in the environment of the OoC platform and co-exist with cells without eliciting any undesirable effects. The term biocompatibility might be a vague one, but it also includes criteria like low operation voltage of the sensor to avoid hydrolysis and damage to biological specimens [13], [14].

Mechanical Flexibility: Materials that are characterised by Young's moduli similar to moduli of soft biological tissues are safe for material-cell interaction, in contrast with rigid, stiff materials that can damage cells and tissues during their interaction. Soft materials are also deformable and flexible, which are factors that promote biocompatibility [15].

Optical Transparency: The sensing area of the device should be transparent allowing various optical microscopy techniques for studying the interaction between biological specimen and the device [16]. This factor is of high importance for biological studies.

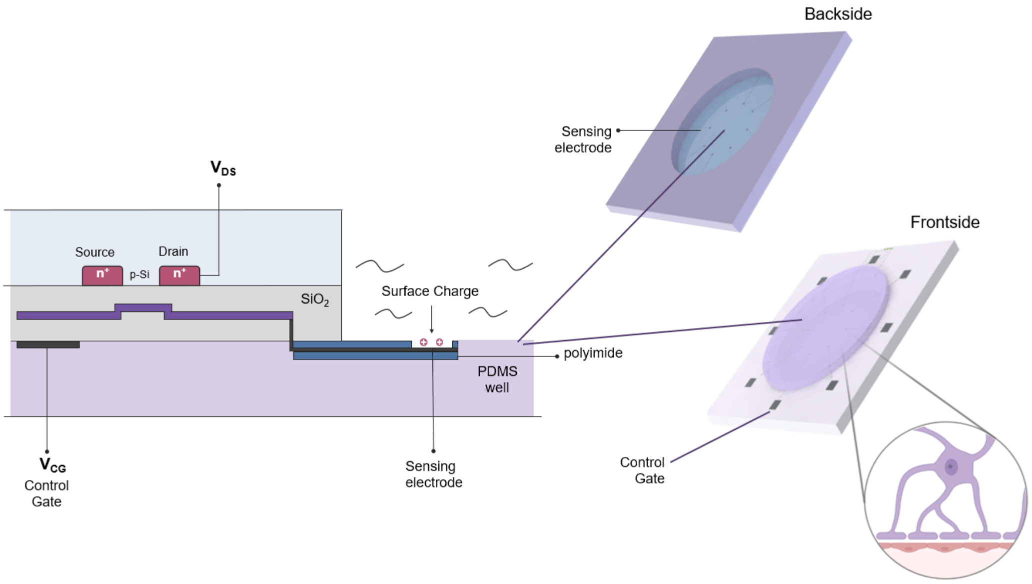

Figure 1.4: Cross-sectional schematic, frontside and backside of the previously fabricated OoC. The PDMS well forms the sensing area where cell cultures are supported.

Sensitivity: The sensitivity of the sensor derives from its output characteristics and indicates the output signal change in respect to varying input signal. For example, the sensitivity of a pH sensor is commonly defined as the change of the output voltage in respect to pH variation $\Delta V/pH$. The sensor must exhibit a significant response to ionic variation in the measurement medium.

CMOS Compatibility: Complementary metal–oxide–semiconductor (CMOS) techniques are well- established and support the cost-efficient mass production and standardisation of reliable, miniaturised sensors, as well as promote the integration of said devices in dense arrays for parallel sensing [17], [18]. CMOS techniques are useful tools for sensor fabrication, even though some applications often require a few non-standard steps, such as post-processing. It should be noted that the integration of flexible structures, such as polymeric membranes, often requires some manual processing.

Operation Stability, Durability: Exposure to wet environments can affect the transistor stability by causing degradation of the exposed sensor parts. Depending on the sensor structure, the device might also be sensitive to environmental parameters like temperature, humidity and pH, limiting the performance stability [14]. For OoC applications, the physiological relevance of the measurement medium is important, indicating that the transistor's electrical parts must be protected from the hostile measurement environment.

Use of reference electrode: An external reference electrode commonly accompanies biosensors in wet condition measurements. An electrode in the form of the conventional bulky Ag/AgCl rod-like electrode or a noble metal wire is dipped in the measurement medium to gate the sensing area and according to theory enhance sensitivity [18]. It is clear that these electrodes are not integrated to the sensor platform, impeding CMOS compatibility and sensor portability. The implementation of an external electrode should be thus avoided.

1.3.2. Constraints

During the designing of the BBB-on-chip, some practical constraints should be taken into account. The limitations of the cleanroom equipment and the availability of materials dominate the decisions around the final design of the sensor. Red metal use should be limited, if possible, to avoid further complicating the fabrication process. Furthermore, the use of lower resolution photolithography masks should be examined, when allowed by the design dimensions, aiming at minimising the fabrication cost.

1.3.3. Research questions

This thesis aims at developing a biocompatible FET-based biosensor with high performance and reliability while combining wafer-scale, CMOS compatible fabrication with an isolated and mechanically flexible sensing area. The project initially examines whether the fabrication of such a sensor is possible and in a deeper level, targets:

- The construction of effective mathematical models based on electrostatic theory for the prediction of the sensor's behaviour in various measurement media and justification of the new design.
- The creation of simulation models using either electrical- or physics-based software to counteract any shortcomings or oversights of the theoretical models and aid the determination of the final design.
- Studying the electrical double-layer (EDL) formation at charged electrode/electrolyte interfaces and its effect on the sensor's operation. More specifically, examining whether the EDL formation on a floating-gate electrode can be considered valid.
- Tackling the external reference electrode impediment. In other words, aiming at developing a sensor that effectively operates without the use of an external reference electrode or integrating the electrode during the fabrication process.

1.4. Report outline

The structure of the report is presented as follows. Chapter 2 introduces the results of an extended literature study on FET-based devices compatible with OoC applications. In Chapter 3, the necessary theoretical background for later interpretation of the results is presented, and the models used for the design determination are explained and verified. The complete process of the final design determination for the new generation of OoCs is analysed in Chapter 4. In Chapter 5, the fabrication process is explained step by step, including issues that hindered the procedure, and the fabricated OoCs are presented in an overview. The results of the process wafer failure investigation, accompanied by chip characterisation measurements, follow in Chapter 6. The report ends with Chapter 7, where the project is briefly discussed in its entirety, and prospective future efforts are examined.

2

Literature Study

In this chapter, a condensed form of the literature study accompanying this project is presented. Following the evolution and the growing interest in FET-based biosensors, a literature study was conducted, aiming at the identification and categorization of such devices suitable for OoC implementation. The identified devices were categorized based on geometry and gate material and were compared based on the following criteria: biocompatibility, mechanical flexibility, optical transparency, sensitivity, CMOS compatibility and operation stability. Identifying all possible FET configurations for biosensing is a demanding and nearly impossible task, but this literature study provides a better insight into available structures. A short introduction to the basic limitations of electrochemical FET-based sensors and the electrical double layer formation is later presented. An overview of the identified structures is shown in Fig 2.1.

2.1. FET-based biosensors

A biosensor is defined as a device capable of converting a biochemical reaction into a measurable electrical signal [19]. Structurally, a biosensor is composed of two functional parts, the bio-recognition element which is also called bioreceptor and the transducer [17], [20], [21]. Biosensing applications include detection of target analytes from ions to macromolecules, such as DNA strands, while also real-time monitoring of biological environments [22], [23]. Especially in the case of constantly regulated environments that promote cell viability/longevity, like in OoC platforms, long-term recordings are also possible [24], [25].

A specific structure of interest is the field-effect transistor (FET), which is a sophisticated device that can be utilized for measuring biochemical signals [26], [27]. The first FET-based biosensor was already developed by the 1970s by Bergveld et al. [28] for pH measurements with numerous FET-based alternatives following over the years. Such devices have been widely studied owing to the variety of materials used and performance reliability. A common field of interest is the sensitivity improvement of said devices and the functionalization of sensing areas towards selectivity improvement [29], [30], [31].

2.2. Silicon-based FETs

Silicon-based sensors are the natural evolution of modern electronics and take advantage of complementary metal-oxide-semiconductor (CMOS) fabrication. Even though not favorable for disposable sensors due to the costly fabrication, they are highly reliable and reproducible [13], [32], [33]. The inorganic semiconductor stiffness is also a concern for biomedical applications, but several studies have shown interest in developing flexible structures [15]. Thus far, conventional FET biosensors have been used to detect several analytes such as ions, DNA, proteins and peptides, and they have also used for cell activity recording [22]. One or more cells can be either directly deposited on the gate electrode or the gate dielectric of the FET, or placed in a chamber in contact with the sensors, while also combining microfluidics for maintaining the viability of cells towards long-term studies [25]. Thus far, such applications are limited to in-vitro conditions due to limited biocompatibility of the top layer of inorganic FETs [27].

2.2.1. Ion-sensitive FETs (ISFETs)

Ion-sensitive FETs (ISFETs), or gateless FETs, are the most extensively studied amongst all the different types of FET-based biosensors. The ISFET structure is based on the removal of the metallic gate of conventional MOSFETs, resulting in the gate dielectric interacting directly with the electrolyte containing the target analyte and the placement of a reference electrode in the aqueous solution [28]. The basic structure of ISFETs can be seen in Fig 2.2.b. and it also offers the ability to enhance the gate dielectric with a chemically sensitive layer depending on the sensing application [22], [24], [34]. ISFETs can be considered electrically identical to MOSFETs, which means that the ISFET operation principles are based on the modulation of the drain current I_{DS} resulting from charge density alterations at the electrolyte/oxide interface. The reference electrode, typically Ag/AgCl, is used to apply the gate voltage V_G and bias the device, so that the target ions or charged biomolecules accumulate at the electrolyte/gate insulator interface. These charges can not pass through the passivation layer of the ISFET, but similarly to MOSFETs, create an electrical field perpendicular to the layers of the structure which modifies the effective gate voltage V_{GS} [18], [21], [35].

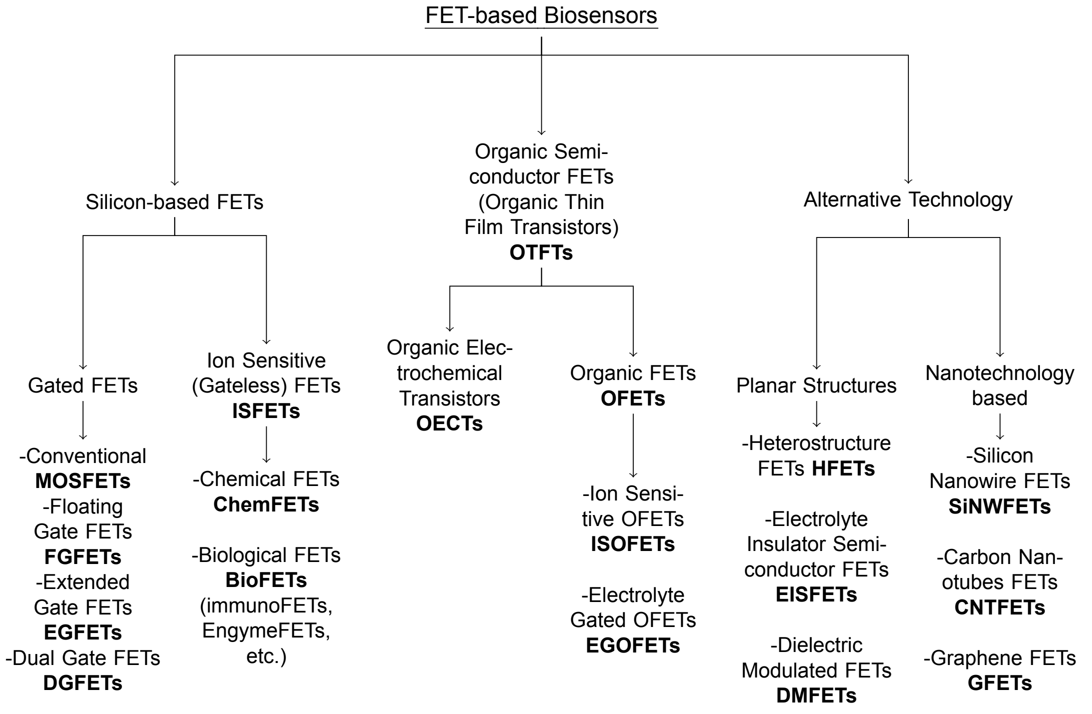

Figure 2.1: Diagram summarizing field-effect transistor based biosensors that show potential for OoC applications. The biosensors are grouped into categories based on structure geometry and gate material.

Negatively (or positively) charged entities accumulating on the sensing layer of an n-type ISFET (or p-type) result in a decrease of the drain current. The effect of the charged molecules can also be studied from the transistor's I-V characteristics [36]. More detailed information on the ISFET theory as well as their technology and instrumentation can be found in the review paper by Bergveld [18].

The reference electrode sets the operation voltage of ISFETs, which must be maintained during the measurement period. For a stable potential to be established, the reference electrode is a thermodynamic half-cell that accommodates a reversible cell-electrode reaction when in electrolytic contact with the analyte. Such electrodes contain two or more conducting phases which exchange charge carriers, with usually one phase being the carrier conductor and the other the electrolyte. The name of said electrodes derives from these phases e.g. Ag(s)/AgCl, while ignoring other involved phases. The Ag/AgCl reference electrodes are the most widely-used, mainly on account of environmental compatibility and as seen in Fig 2.2.c. consist of a metal lead, hardly soluble metal salt (AgCl), a reservoir containing the related anion (KCl), all encapsulated in one unit with an optional diaphragm at the bottom. These structures are bulky and must be fabricated separately from the sensor, impeding thus the miniaturization and cost-effectiveness of silicon-based sensors. The embodiment of reference electrodes to the fabrication procedure is critical, but for now classical reference electrodes dominate the market [37], [38].

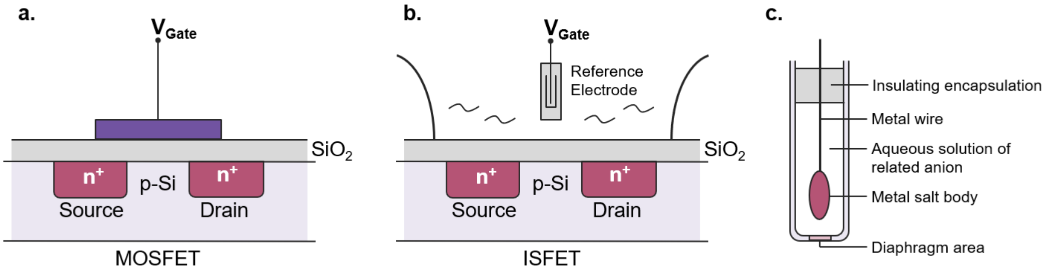

Figure 2.2: General representation of: **a.** the MOSFET structure, **b.** the ISFET structure and **c.** a conventional reference electrode and its components.

Both sensitivity and selectivity of ISFET devices are largely determined by the chemical and physical characteristics of the outer gate insulator. Especially for the pH sensitive ISFET, the most studied ISFET device, several types of H^+ sensitive layers have been used on top of the original silicon dioxide, such as SiO_2, Si_3N_4, Al_2O_3 or Ta_2O_5 [34], [39]. However, exposure to electrolyte or even harsher environments, in the case of biological media, can result in poor transistor stability and fast degradation of the exposed layers [14]. Therefore, during the ISFET designing process most modifications aim towards solving encapsulation issues, so that the device can effectively operate in wet environments with minimization of the post-processing, while still being suitable for mass production [18].

Currently, the fabrication of CMOS compatible ISFETs is associated with extending the gate of the ISFET to the top metal, thus forming floating electrodes, and by having the passivation layer (usually silicon nitride and/or silicon oxynitride) act like the chemically sensitive membrane [40]. Despite their widespread use, drawbacks other than fabrication-related ones are still potent, including an external reference electrode. To overcome the low sensitivity of ISFETs, various sensitive membranes were studied, but the sensitivity can still not overcome the Nernst limit at 59 mV/pH [22], [36]. When these membranes are chemically sensitive to specific ions, the devices are called chemically-sensitive FETs (ChemFETs). Biological FETs (BioFETs) implement biorecognition materials such as single-stranded-DNA, proteins and enzymes for sensing applications and also act as cell-based biosensors. BioFETs can be divided into categories based on their biological target like the enzyme-modified FETs (EnFETs or Enzyme-FETs), immunologically modified FETs (ImmunoFETs) and cell-based FETs. Cell-based ISFETs are formed by depositing a cell directly onto the gate insulator of the transistor, in order to study the metabolism of the cell or record extracellular potential measurements. An overview of some major historical landmarks on the evolution of ISFETs and their subcategories can be found in Table 2.1.

Table 2.1: Significant landmarks on the history of ISFET technology

1970	ISFET concept, pH measurements in neurophysiological environment [28]
1976	Concept of EnFET [41]
1978	Concept of ImmunoFET [42]
1980	First realized EnFET[43]
1981	First tissue-MOSFET device [44]
1983	First extended-gate FET [45]
1984	First attempt towards CMOS compatible ISFET [46]
1991	First neuron-transistor [47]
1997	Concept of Beetle-FET [48]
1997	First attempt of direct DNA-hybridization detection [49]
2003	First commercialized ISFET-based pH sensor [18]

2.2.2. Metal-oxide-semiconductor FETs (MOSFETs)

In the case of a MOSFET biosensor (or insulated gate FET - IGFET), a metallic electrode is deposited on the insulating surface and thus the gate is electrically isolated from the other electrodes (see Fig 2.2.a.). In a nutshell the MOSFET's drain current is modulated by the voltage applied through the gate. When the IGFET is used as a biosensor, the changes of the surface charge density of the gate, due to binding of the target analyte, lead to a shift of the threshold voltage V_T. In this way, the charged entities on the gate surface result in a measurable electrical signal [22]. This literature study indicated that the only biological-related IGFET applications are pH and DNA hybridization detection. DNA detection is common in numerous biosensor types, presumably as negatively charged oligomers cause a significant threshold voltage shift in p-channelled MOSFETs [50]. It is not clear whether other biological targets can also induce significant FET response.

2.2.3. Extended-gate FET (EGFET)

The extended-gate FET (EGFET), as seen in Fig 2.3.a. follows the same operation principles with ISFETs, but separates the transducing from the sensing part of the biosensor. A metal signal line is extended from the transistor's gate and a sensing membrane is deposited on the end of the line [51], [52]. The decoupling of sensing and transducing part of the biosensor allows independent designing of each part and simplifies the fabrication of the device. EGFET studies indicated that low-resistance materials, such as SnO_2, TiO_2, ZnO, TiN, anodized AlO_x and indium tin oxide (ITO) are preferable for the sensing layer to avoid electrical signal attenuation [52], [53]. In contrast with conventional MOSFET biosensors, EFGETs have successfully been used for label-free detection of both ions and biological molecules including proteins, urea, glucose and DNA, as well as for En-FET and Immuno-FET applications. Research groups have studied the fabrication of extended electrodes on flexible substrates such as PET and PEDOT ([51], [52], [54]), while others focus their efforts on the fabrication of low-cost, disposable electrodes ([53], [55], [56], [57]).

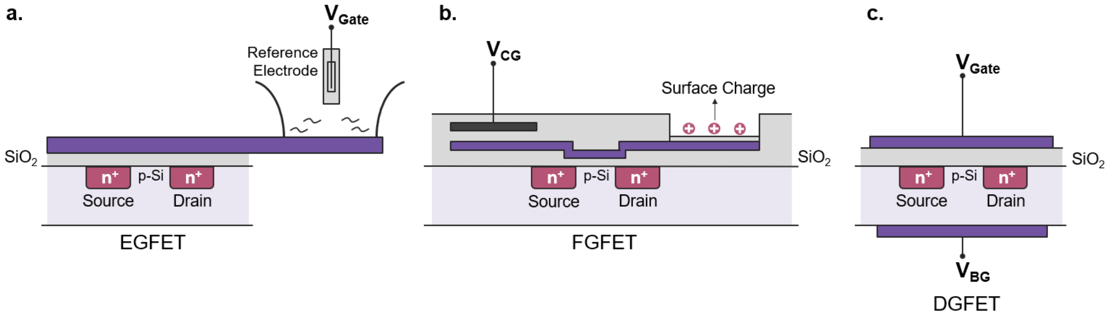

Figure 2.3: Schematic representation of **a.** the generic structure of an extended-gate FET (EGFET), **b.** a floating-gate FET-based sensor geometry (FGFET), and **c.** dual-gate FET (DGFET) sensor.

2.2.4. Floating-gate FETs (FGFETs)

The floating gate FETs (FGFETs), first introduced as memory cells, are composed of a fully electrically insulated metallic gate electrode that is capacitively coupled to a second gate electrode. The floating gate electrode acts as a charge storage element following the charge conservation principle, and is governed by the secondary control gate [58]. By exposing a part of the floating gate to a measurement medium, as for example in Fig 2.3.b., the FGFET can act as a biosensor. The independently driven control gate sets the operating point of the device, and as the charged analytes interact with the sensing gate, the induced electric field causes charge separation inside the floating electrode. This effect modulates the FG potential and as a consequence the drain current I_{DS} [59], [34]. In the FGFET configuration, no external reference electrode is needed to bias the floating gate, but some studies tested the combination of ISFET ionic interaction with the FGFET double-gate geometry [60], [61], [31]. FGFETs have been successfully used for the detection of analytes ranging from ions to biomolecules, such as glucose and urea (see Table A.1), as well as for cell monitoring [62], [63],[64].

2.2.5. Dual-gate FETs (DGFETs)

Compared to a conventional FET, dual-gate structures employ an additional back gate that interferes with the operation of the device (see Fig 2.3.c.). Dual-gate FETs (DGFETs) consist of two capacitively coupled gates, one placed on the top and usually the thicker at the bottom of the transistor. The back gate formation requires post-processing, as the back of the transistor must be opened and filled with a dielectric [34]. The gate coupling effect is considered to increase the drain current for shorter channels and it is reported that DGFETs exhibit an enhanced shift of the threshold voltage V_T, when measured from the back gate [65]. DGFETs can operate with or without a reference electrode immersed in electrolyte, by biasing the device through the two gates. Thus, the performance of DGFET sensors depends both on the capacitive effect, influenced by the gate and gate oxide thickness, and the sensing area configuration [66]. Similarly to MOSFETs, the only identified DGFET biosensing applications involve pH and DNA detection.

2.3. Organic Semiconductor-based FETs

The idea of using organic materials as the active component of transistors was first realized for gas sensors [67], with liquid detection applications following later [68]. These materials combine the electrical properties of semiconductors and the favorable properties of plastics, such as mechanical flexibility, solubility and physico-chemical adjustability [69]. However, organic semiconductor-based transistors are not expected to reach the performance and stability of their inorganic counterparts. Organic semiconductors are characterized by limited carrier density and low carrier mobility, which are counteracted by applying high operation voltages [13], [59]. Several studies focus on developing organic semiconductor-based FET biosensors that operate on low voltages, by either implementing new materials or designing new configurations [70], [71]. The fabrication of organic-based transistors usually involves printing techniques or thermal evaporation at low-temperatures, with no cleanroom facilities requirement and a variety of available inexpensive substrates, such as glass, metal foils, plastics and papers. Organic semiconductors are suitable for the fabrication of flexible biosensors, but with low reproducibility and fast degradation, especially during liquid media measurements. In most cases, such devices are marketed for disposable application thanks to their low fabrication cost and environmental friendliness [72],[73], [33].

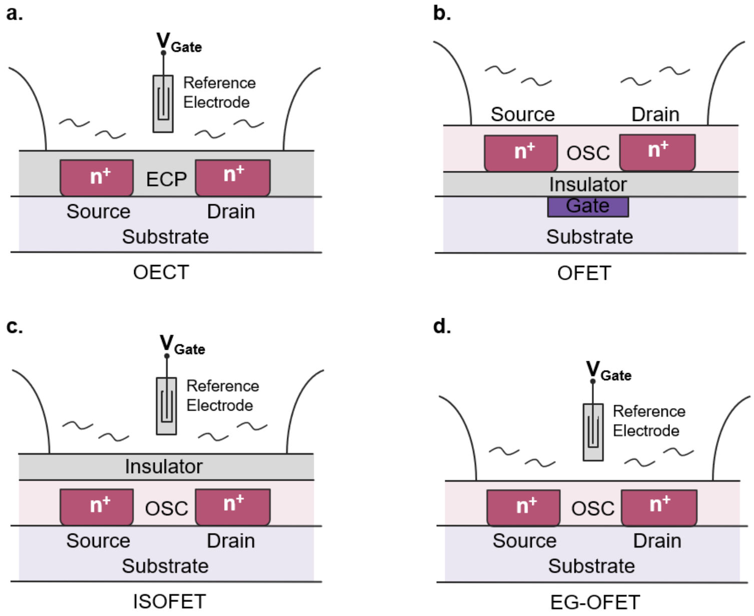

Figure 2.4: Basic structures of organic semiconductor-based FET biosensors: **a.** Organic Electrochemical Transistor, **b.** Organic FET, **c.** Ion sensitive organic FET, **d.** Electrolyte gated FET. ECP stands for electrically conducting polymer, and OSC for organic semiconductor.

2.3.1. Organic electrochemical transistors (OECTs)

Organic electrochemical transistors (OECTs) use a conducting polymer as the connection between the source and drain electrodes, while the external gate electrode is separated from the polymer by an electrolyte (see Fig 2.4.a.). The OECT operation is based on the conductivity modulation of the active layer by electrochemical doping (or de-doping) of the polymer, which involves ion transport in (or out) of the active layer from (or to) the electrolyte. The external gate electrode controls the behaviour of the conduction channel and OECT sensors operate at low voltages, reaching below 1V, thus prohibiting the risk for unwanted redox reactions in aqueous media [74], [75]. They are commonly used as enzyme biosensors, because enzymatic reactions cause a local change of pH and most OECT polymers are sensitive to pH alteration [13], [36].

2.3.2. Organic FETs (OFETs)

In the case of a thin organic semiconducting channel separated from the gate electrode by an insulating layer instead of electrolyte as shown in Fig 2.4b., an organic FET (OFET) is formed. The operation of OFETs is similar to that of conventional FET transistors. It is based on the regulation of carrier density in the active channel which is exposed to the target analytes, by controlling the applied gate voltage [76]. In contrast with OECT devices, OFET sensors operate on high voltages that generate high electric fields close to the source and drain electrodes and increase the risk of hydrolysis [14], [13]. The performance of OFETs is influenced by the properties of the dielectric-semiconductor interface, including the semiconductor layer thickness, as well as the properties at the grain boundaries of the organic semiconductor [33], [77].

2.3.3. Ion-sensitive organic FETs (ISOFETs)

The ion-sensitive FET geometry is also used for organic semiconductor-based FETs, by omitting the gate electrode from the bulk of the OFET and implementing a reference electrode instead. As shown in Fig 2.4.c., the dielectric layer is exposed to the electrolyte, in contrast with OECTs where the semiconducting polymer comes in contact with the measurement medium. The operation of ISOFETs is similar to that of ISFETs as the drain current is modulated by the electric field across the insulating layer. The potential of the electrolyte/insulator interface is affected by accumulation of ions or charged molecules, which results in variations of the drain current [78], [13]. Similarly to inorganic ISFETs, the gate insulator material plays a significant role in the performance of the device and By immobilizing biorecognition elements on the insulator, ISOFET sensors can detect a variety of biomolecules [13].

2.3.4. Electrolyte-gated OFETs (EG-OFETs)

The concept of electrolyte-gated OFETs (EG-OFETs) for sensing application emerged later than the other organic-based transistors and they are often classified as a subcategory of OFETs. They consist of an external gate electrode immersed in an electrolyte that comes in direct contact with the organic semiconductor, as seen in Fig 2.4.d. EG-OFETs are structurally similar to OECTs, but their working principles are different. The operation of EG-OFETs involves capacitive processes and no charge exchange between electrolyte and semiconductor, whereas OECT operation is based on electron transfer from electrolyte to active layer [33]. The working principle of EG-OFETs is tightly connected to the formation of an electrical double layer (EDL) at both the electrolyte–semiconductor and the electrolyte–gate interfaces, which acts as a dipole preventing charge transfer across the interface [13]. As a result of the double-layer formation, EG-OFETs present higher gate capacitance than other solid dielectric gated OFET types, hence EG-OFETs can operate at low voltages. The detection mechanism in EG-OFET sensors is based on the double layer capacitance variation induced by the interaction with target analytes such as DNA strands, enzymes, and proteins [79].

2.3.5. Floating- and extended-gate OFET variants

A variance of the floating gate configuration, the organic charge-modulated FET (OCMFET) has two gates, an elongated floating electrode capacitively coupled to a control electrode. In this design, part of the floating gate acts as the sensing area of the device [23]. The function of the OCMFET is based on field-effect modulation induced by target analytes and not on the modification of the organic semiconductor properties. The accumulation of electrical charge from target analytes on the sensing area results in a shift of the threshold voltage V_T that can be recorded without high operation voltages [80],

[71]. OCMFET devices have been successfully tested as pH and DNA hybridization sensors and they have also been used for neuronal activity recording applications [70], [72], [81], [82].

The implementation of an extended gate leads the path for organic-based biosensors with flexible and potentially disposable sensing electrodes. This configuration separates the sensing device part, thus making the choice of gate dielectric less critical and commonly utilizes a reference electrode [83], [16]. Such devices usually operate on low voltages and have been studied for detection of proteins, saccharides, amino acids as well as for immunosensing applications [84], [85], [86].

2.4. Alternative FET-based structures

2.4.1. Heterostructure GaN/AlGaN FETs (HFETs)

Some studies have focused on using other materials for the active part of the device or the gate area. For example, Heterostructure GaN/AlGaN field-effect transistors (HFETs) are planar devices, where the conducting channel is formed by the two-dimensional electron gas (2DEG) at the interface of the heterostructure, as shown in Fig 2.5.a. The electrical properties of the heterostructure lead to high mobility and density of the charge carriers, the 2DEG electrons. Furthermore, the HFET conductive channel is formed very close to the surface of the device, thus making the device significantly sensitive to external parameters like stress and proximal electrical charges [87], [88]. The chemically inert surface of an AlGaN/GaN HFET makes them highly stable in aqueous solutions, and can be functionalized with chemical receptors, so that target biomolecules can bind in close proximity with the conductive channel or cells can be directly placed on the gate [89], [90]. These structures can have two gate configurations, either using a gate electrode on top of the AlGaN layer or operating gateless by immersing a reference electrode in the measurement medium.

2.4.2. Electrolyte–insulator–semiconductor FETs (EISFETs)

electrolyte–insulator–semiconductor (EIS) FET structures were initially studied as capacitive biosensors, but can also detect the binding between immobilized receptors and target analytes. They translate the biochemical signal into a change in capacitance, in the same way a binding event would lead to a threshold voltage shift in conventional FET biosensors [91], [92]. This mechanism made EIS structures useful initially for pH measurements and later for DNA hybridization as well as protein detection and as capacitive immunosensors [93], [49], [91], [94]. There are two types of EIS-based biosensors, planar EIS FETs and FETs that utilize porous silicon (pSi). Porous silicon is frequently used as the transducer material of the device, because it provides a larger active surface area compared to planar EIS transistors, which leads to an increase of the maximum capacitance. The sensitivity of the devices is also enhanced by the use of porous silicon, as receptors are immobilized onto the pore walls and thus the binding of analyte molecules inside the pores protects them from leaching out [93], [95].

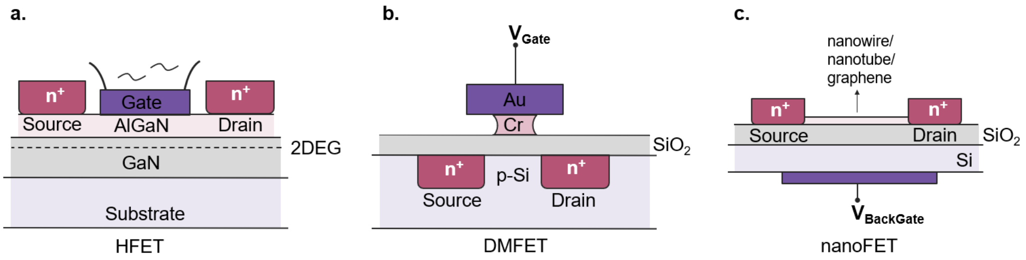

Figure 2.5: a. Schematic representation of: **a.** an AlGaN/GaN heterostructure FET biosensor, **b.** a dielectric modulated FET structure, and **c.** a generic nanostructure-based FET sensor, where either a nanowire, nanotube or graphene connects the source and drain terminals. 2DEG stands for two-dimensional electron gas.

2.4.3. Dielectric modulated FETs (DMFETs)

Dielectric modulated FETs or DMFETs are quite similar to conventional MOSFETs with the difference that there are nanogaps filled with air at the edge of the gate electrode. These nanogaps can be either planar or vertical, like the one shown in Fig 2.5.b. [36]. Similarly to EIS devices with porous silicon, the functionalized nanocavities act as the biorecognition sites where target analytes are immobilized covering a significant percentage of the cavity volume and thus increasing the sensitivity of the device [96]. The binding effect results in a shift of the threshold voltage V_t that depends on two factors, the modulation of the gate dielectric constant (and capacitance) and the target's charge [97]. Based on this principle, DMFET devices have been used to detect DNA and proteins, the last being weakly charged molecules. In the case of protein detection, the charge effect is insignificant on the modulation of the threshold voltage, and the sensor operation is mainly based on the dielectric constant change [98], [97].

2.4.4. Silicon nanowire FETs (SiNWFETs)

Both one-dimensional nanomaterials like silicon nanowires and carbon nanotubes, and two-dimensional materials, such as graphene, can be combined with FETs, mainly by implementing nanostructures on the gate area as the transducer, in the way depicted in Fig 2.5. The high surface-to-volume ratio of nanostructures permits accumulation of more analytes per unit area, in contrast with analytes interacting only with the sensing surface area in the case of planar structures [99], [100].

A typical silicon nanowire (SiNW) biosensor utilizes a nanowire as the channel between the source and drain electrodes, which can be directly functionalized with receptor molecules. In this configuration, the SiNW is both the sensing component and the conduction channel of the device, while surface interactions due to the binding of target analytes on the SiNW affect the measured drain current [101]. The nanowire carrier density alteration is caused by charge transfer and/or electrostatic gating [102]. The sensitivity, as well as the electrical properties of semiconducting nanowires, can be controlled and reproduced with high accuracy by manipulating the dopant concentration, growth and diameter of the wires [103], [101], [104]. SiNWFET sensors have been developed for protein, DNA and small molecule detection as well as for virus, early-cancer and biomarker detection [25], [103]. Nevertheless, even though a SiNW-based device has been efficiently used for single virus detection, the nanowire dimension is unsuitable for the detection of cells [103].

2.4.5. Carbon nanotubes FETs (CNTFETs)

Carbon nanotubes (CNTs) are single-atom-thick, quasi-one-dimensional structures characterized by electrical properties such as low resistance and high charge carrier mobility that render them promising sensing components [105]. They are divided into two categories, multi-walled CNTs (MWCNTs) with metallic conductive properties and single-walled CNTs (SWNTs) which exhibit metallic or semiconducting electrical properties depending on their diameter and chirality [30], [103]. SWNTFET structures can be composed of either individual SWNTs or random SWNT networks positioned between the source and drain electrodes. Their operation principles are complex, involving both the field-effect and electron transfer, but the interaction between analytes and CNT surface alters the CNT band structure, resulting in drain current modulation [106], [107]. There are several CNTFET devices for DNA, protein and single-molecule detection, while CNTFETs have also been used for cell monitoring [103], [105].

2.4.6. Graphene-based FETs (GFETs)

Graphene, the ”youngest” cousin of carbon nanotubes, is a two-dimensional ultra-thin carbon honeycomb lattice with exceptional and highly controllable electrical properties that can be utilized as the transduction material for FET devices. Single-layer graphene possesses high carrier mobility and large carrier concentrations, and offers a larger detection area than nanotubes [108], [30]. In a graphene-based FET (GFET), the graphene sheet acts as the semiconducting channel between the source and drain electrodes and charged analytes can directly bind on the graphene film. The analytes act either as electron donors or acceptors and alter the conductivity of the channel [103], [109]. Graphene nanosheets, similarly to nanotubes, are highly sensitive to surface charge and so unwanted charged entities are expected to significantly affect the graphene conductance upon binding [108]. Graphene-based FETs have been used to detect several biomolecules such as DNA, glucose and proteins, and bacterial activity recording. Similarly to CNTFETs, most GFETs follow the external gate electrode configuration, but there are also cases that utilize a back gate [109], [110].

2.5. Nernst limit and Debye screening effect

The first papers on FET-based sensors report that the pH response of the devices is described by inserting the Nernst equation into the MOSFET operation equations [18]. By treating the ions of the electrolyte as points with no physical dimensions, it can be hypothesized that the application of a gate potential leads to ion accumulation near the electrode's surface. There, the repulsion between counter-ions generates the formation of a wide diffusion layer in proximity to the gate. The pH of the electrolyte affects the number of protons that can accumulate on the gate area and consequently influences the surface potential of the gate [34]. The Nerstian law describes the response of the sensing component

$$E = E_0 + \frac{RT}{zF} ln[i] \tag{2.1}$$

where E is the measured surface potential in Volts,
E_0 is a constant depending on the external electrode,
R is the gas constant,
T is the absolute temperature in Kelvin,
z is the signed ionic charge,
F is the Faraday constant,
and $[i]$ is the molar concentration of the free ions.

The Nernstian model indicates that the relation between surface potential of the electrode and pH response is linear with a slope of 59 mV/pH. This is the so called Nernst limit of MOSFET sensitivity [39]. Experiments show sub-Nernstian slopes, which are accounted for in later theoretical models.

More advanced theories consider pH sensitivity due to both ion site-binding on the gate insulator and formation of an electric double layer (EDL) close to the sensing surface. Liquid electrolytes contain ions of different sizes and charge, which accumulate in an anisotropic fashion at the sensing surface/electrolyte interface, thus forming the double-layer [39]. According to the Gouy–Chapman theory [111] outer charges then form a diffuse layer between the Helmholtz planes at the bulk of the electrolyte (see Fig 2.6.a.). Before taking into account the mobile solvated ions that form the diffusion layer, Helmholtz [112] theorized that the interfacial capacitance of the EDL C_I depends on several parameters as indicated by the equation

$$C_I = A\frac{\epsilon_o \epsilon_r}{d_{OHP}} \tag{2.2}$$

where ϵ_o is the permittivity of free space,
ϵ_r is the permittivity of the electrolyte,
A is the sensing component/electrolyte interface area,
and d_{OHP} is the distance between the outer Helmholtz plane (OHP) and the metallic gate electrode.

It was understood that the double layer acts a capacitance, so a simple capacitor equation of the form $Q = C/V$, where Q is the surface charge due to accumulated ions on the gate area, C is the double layer capacitance at the interface and V is the surface potential (equivalent to the one written down as E in eq. 2.1), can efficiently explain experimental results [113]. Consequently, the sensitivity to pH measurements can be described as

$$\frac{\Delta\Psi}{\Delta pH_{bulk}} = -2.3\alpha\frac{RT}{F} \tag{2.3}$$

with

$$\alpha = \frac{1}{(2.3kT/q^2)(C_s/\beta_s) + 1} \tag{2.4}$$

where Ψ is the surface potential,
$\Delta\Psi$ is the pH change of the bulk solution,
α is a sensitivity factor with values from 0 to 1,
C_s is the double layer capacitance,
and β_s is the surface buffer capacity.

The correlation between eq 2.3 and the Nernst model is described by the sensitivity factor α. High α values (approaching 1) correspond to the maximum Nernstian sensitivity, while lower α values explain the sub-Nernstian behavior [18], [34].

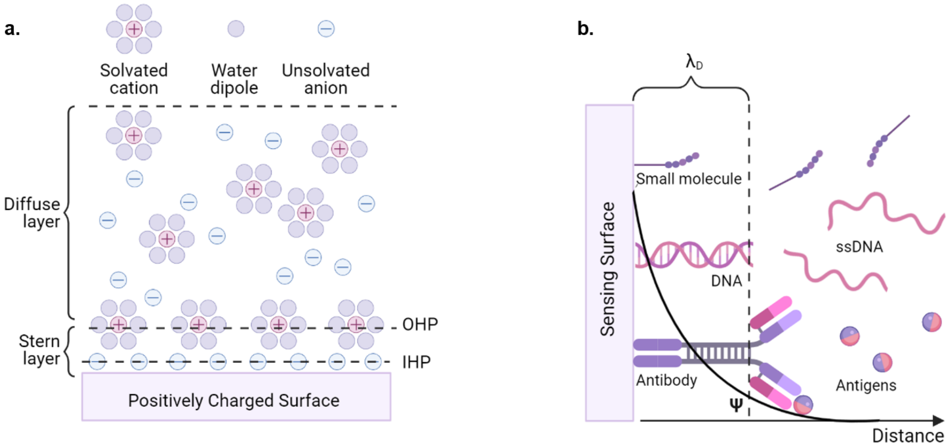

Figure 2.6: **a.** Illustration of the electric double layer at the electrolyte-charged surface interface, showing the inner (IHP) and outer Helmholtz plane (OHP), and the diffusion layer. **b.** A schematic depiction of the electrical double layer's length for different target molecules (not scaled). The distance of one Debye length λ_D is noted, while the surface potential Ψ is exponentially decreasing with distance. Created with BioRender.com.

The same double-layer affects the performance of FET devices when detecting biological analytes as well. When large charged-macromolecules in an ionic solution are immobilized on the sensing area, the free-moving small counter-ions of the electrolyte accumulate around the target-molecules, thus forming a cloud of opposite charge. This screening of the target-molecules by electrolyte counter-ions depends on the distance between the sensing surface and target molecule [34]. The further from the sensing surface, the less the screening effect. The distance where the electrical signal reaches 1/e of its initial value is defined as one Debye length λ_D [114]. This means that the detection of charges or biomolecules is only possible within the range of one Debye length, which strongly impedes the sensing ability of FET devices [17], [21]. The Debye length λ_D for an electrolytic buffer solution is described by the equation

$$\lambda_D = \left(\frac{\epsilon_{e1}\epsilon_0 kT}{2z^2q^2I}\right)^{1/2} \tag{2.5}$$

where ϵ_{e1} is the dielectric constant of the electrolyte,
ϵ_0 is the vacuum permitivity,
k is the Boltzmann constant,
z is the electrolyte ion valency,
q is the elementary charge,
and I is the ionic strength of the solution.

The equation indicates that the Debye length is inversely proportional to the square root of I, which means that reduced ionic concentration increases the Debye length. Typically, the screening length is in the order of 1nm, but it can increase in the case of highly diluted solutions [13]. Furthermore, the screening length dependence on the distance from the sensing surface designates that larger molecules correspond to stronger screening effects (Fig 2.6.b.). As the electrical signal of one macromolecule can only result from the part of the target that is in the range of one Debye length, long molecules and the use of linkers for the binding of the targets further impede biological measurements[34]. For example, highly sensitive detection of DNA is not possible in a physiological solution where $\lambda_D = 0.8nm$, because most of the charge will be further away from the screening length [92]. On the other hand, smaller molecules like aptamers can lead to protein detection with high sensitivity [105].

The Debye screening effect is a fundamental limitation of FET sensors, so considerable efforts have been made to overcome this issue [22]. In the review article by Kaisti *et al.* it is mentioned that successful efforts have been noted for label-free detection of large molecule complexes (like antibody-antigen), but there is no standard method of overcoming the screening effect yet [34].

2.6. Comparison

Here, the results of the comparison between the identified FET-based devices are presented and summarised in Table 2.2.

Table 2.2: Comparison table between the devices discussed in this study. Some basic remarks are noted for each category of biosensors in regard to the comparison criteria. No optimal sensor can be identified from this table.

	Biocompatibility	**Flexibility, Optical Transparency**	**Sensitivity**
Silicon-based FETs	ISFETs and FGFETs used as cell-based sensors. Lack of studies in physiological media	Made of rigid materials. Possible use of flexible extended gate electrodes.	Devices like CMFETs and EGFETs show improved performance. DGFETs exhibit super-Nernstian responses
Organic Semiconductor-based FETs	Mostly high operation voltages. OECTs and OCMFETs applications as cell-based sensors. No physiological media studies	Inherently flexible and transparent structures. They can be fabricated on several substrates.	Organic-semiconductors have poorer electrical properties than Si, with structures like the OCMFET improving their performance. They are marketed as cheap, disposable biosensors.
Planar alternative FETs	Non-toxic HFETs are suitable for cell-based sensors and have achieved detection in physiological media	Non-flexible structures	EISFETs and DMFETs increase the surface-to-volume ratio towards improving sensitivity. HFETs exhibit high SnR.
Nanotechnology-based FETs	C nanotube- and graphene-based sensors are suitable for cell monitoring.	Graphene-sensors have been fabricated on flexible substrates.	Nanotechnology-based FETs are promising thanks to the high surface-to- volume ratio, especially when a back-gate is implemented.

	CMOS Compatibility	**Operation Stability**	
Silicon-based FETs	They can take full advantage of CMOS compatibility.	The drain and source electrodes must be protected from the electrolyte. Some geometries promote physical separation between sensing area and active device.	
Organic Semiconductor-based FETs	Fabrication is mostly based on soft lithography methods.	Poor stability for direct electrolyte/semiconductor contact. The separation of the sensing area overcomes this issue.	
Planar alternative FETs	EISFETs are compatible, DMFETs require some off-standard steps, while HFETs are based on materials other than Si.	No stability issues were reported.	
Nanotechnology-based FETs	Other than the nano-structure, the transistor is based on Si technology.	No stability issues were reported.	

2.6.1. Biocompatibility, Flexibility and Optical Transparency

Several FET-based sensors have been used for extracellular activity recording, including ISFETs, floating gate FETs, heterostructure FETs and CNT,graphene-based FETs. Silicon-based structures have been studied as cell-based sensors despite their rigidity, a disadvantage compared to organic-based sensors that promote flexibility. On the contrary, the high operation voltage of the latter not only increases hydrolysis risk, but is also dangerous for the surrounding cells. The operation voltage is noted as a biocompatibility indicator in the summary tables in appendix A. The common and persistent impediment of FET-based biosensors is the Debye screening effect that inhibits detection in electrolytes with high ionic strength. Detection in physiological media is critical for organ-on-chip applications which aim at accommodating sensor-cell interaction, but only a few studies successfully detected analytes in physiological media like serum and urine (with poor sensor performance). Most studies choose highly diluted electrolytes to increase the Debye screening length λ_D so that firstly the detection is possible and secondly for achieving higher sensitivity. By overcoming this screening effect, FET-based biosensors are expected to be commercialized and replace other platforms like enzyme-linked immunosorbent assays (ELISA).

2.6.2. Sensitivity

As indicated by the identified studies, there is no standardized way of quantifying sensitivity with different alternatives including measuring the variation of the threshold voltage ΔV_T, gate voltage ΔV_{GS}, drain current ΔI_{DS} or transconductance ΔG before and after introducing the target analyte in the electrolyte. For pH sensing, sensitivity is commonly defined as the threshold voltage shift ΔV_T in respect to pH variation, in mV/pH. However, even with a standardized way of measuring sensitivity, the direct comparison between different studies is not possible unless the same measurement medium is used. Up to this point, sensitivity is merely an indicator of the sensor's performance rather than a means of direct comparison between different structures. Another sensor performance indicator is the limit-of-detection (LOD), which corresponds to the lower concentration of analyte that the sensor can detect in electrolyte. The limit-of-detection is also affected by the Debye screening effect.

The sensing performance of FET-based devices can be improved by either amplifying the field-effect and/or by increasing field susceptibility. Devices that utilize gate extensions, floating gates or the dual gate configuration follow the first strategy, while structures and materials such as porous silicon, nanowires and nanotubes provide a higher surface-to-volume ratio. The summary tables in appendix A indicate improved performance for more recent FET geometries compared to conventional ISFETs and highly promising performances for nanomaterial-based sensors. The performance is lower for organic semiconductor-based sensors, with only one device exhibiting super-Nernstian response. Nanotechnology-based FET biosensors show low detection limits, reaching the femtomolar range (100pM at the lowest), while they perform better than other sensors that take advantage of bigger effective areas, such as DMFETs and EISFETs with porous silicon. An interesting comparison based on Table A.3 indicates that the nanowire-based sensor by Zheng et al. (with a sensitivity of 0.9pg/mL) is more effective than the heterostructure-FET by Wang et al. (100ng/mL) in the detection of analytes in undiluted serum.

2.6.3. CMOS Compatibility

The inherent advantage of silicon-based technology is based on the widely studied fabrication techniques and processing methods. Initially, ion-sensitive FETs were not fully CMOS compatible, but they are currently developed so that no post-processing or material removal is needed, with the exception of the external reference electrode fabrication. Organic semiconductor-based sensors are developed by different methods, mainly soft lithography-related, heterostructure FETs are based on the AlGaN/GaN interface and DMFETs require material removal steps to form the gaps of the sensing area. EISFETs and porous silicon fabrication is CMOS compatible, and in the case of nanotechnology-based FETs, most of the times the main part of the transistor is based on silicon technology.

2.6.4. Operation Stability

When the sensing area is placed on top of the active sensor, the continuous interaction between electrolyte and device can lead to fast material degradation and unstable sensor operation. ISFETs utilize the gate oxide as the sensing layer, so the source and drain electrodes should be protected from electrolyte exposure to maintain the reliability of the sensor. Organic semiconductors are inherently more vulnerable to electrolytes since they might absorb charge carriers and alter their electrical properties, thus affecting the output of the device. Devices such as OECTs, OFETs and electrolyte gated-OFETs which utilize the organic semiconductor as the sensing area are vulnerable to degradation and exhibit limited operation durability. As a result, such devices are usually marketed as disposable and low-cost sensors. To overcome this issue, other geometries like the OCMFET and the extended gate OFET were developed, so that the sensing area is independent of the active part of the sensor. Heterostructure FETs exhibit operational stability even for measurements in physiological buffers, while for the other planar structures (EISFETs and DMFETs) no stability issues were noted. Similarly, nanotechnology-based sensors do not show instability issues when in contact with an electrolyte.

2.6.5. Reference Electrode Alternatives

Table 2.3: The table sums up all studies that either have flexible structures or operate without the use of an external reference electrode. The type of the biosensor, the selective layer and the detection target of the studies are also noted.

Device	Detection Layer	Target	Flexibility	Reference Electrode	Reference
MOSFET	SiO_2	DNA	Non flexible	Gate electrode on gate oxide	Dashiell et al. [115]
MOSFET	PLL +DNA probes	DNA hybridization	Non flexible	Gate electrode on gate oxide	Fritz et al. [116]
MOSFET	thiolated-ssDNA probes	DNA hybridization	Non flexible	Gate electrode on gate oxide	Kim et al. [117]
EGFET	NH_3 plasma	pH	Flexible electrodes	Reference electrode	Yang et al. [52]
EGFET	boronic acid modified RuO_x	pH glucose	Flexible substrate	Yes	Singh et al. [51]
EGFET	anti-HbA1c anti-Hb	HbA1c Hb	Non flexible	Differential measurements	Bian et al. [57]
FGFET	thiolated DNA strands	DNA hybridization	Non flexible	Control gate	Barbaro et al. [58]
FGFET	thiolated DNA strands	DNA hybridization	Non flexible	Control gate	Barbaro et al. [118]
FGFET	nitride layer	ions	Non flexible	Control gate	Chengwu et al. [119]
FGFET	SiO_2	ions	Non flexible	Control gate	Chen et al. [26]
CvMOS	poly-Si	ions	Non flexible	Control gate	Shen et al. [120]
DG-ISFET	SiO_2	pH	Non flexible	Back gate	Park et al. [65]
OFET	Ta_2O_5	pH	Flexible structure	Integrated Ag/AgCl electrode	Gao et al. [121]
ISOFET	Mylar insulator	pH	Flexible, Mylar-based	Reference electrode	Loi et al. [122]
ISOFET	SiN:H on	pH	Flexible	Reference electrode	Diallo et al. [123]
EGOFET	streptavidin	biotinylated IgG	Flexible electrodes	Reference electrode	Minamiki et al. [84]
EGOFET	artificial phosphoprotein receptor	α-casein	Flexible electrodes	Reference electrode	Minamiki et al. [124]
EGOFET	anti-CgA antibody	hCgA	Flexible electrodes	Reference electrode	Minamiki et al. [125]
EGOFET	ITO/PET	pH	Flexible electrodes	Reference electrode	Tang et al. [126]
EGOFET	PEGs	GFAP	Flexible	No reference electrode	Song et al. [127]
EGOFET	NH_2-group SAM	pH	Flexible	Control gate	Caboni et al. [83]
EG-FGFET	ssDNA probes	DNA hybridization	Non flexible	Control gate	White et al. [128]
EG-FGFET	DNA aptamer	ricin	Non flexible	Control gate	White et al. [129]
EG-FGFET	carboxylic acid-terminated SAM	pH	Non flexible	Control gate	Thomas et al. [130]
HFET	biotin	streptavidin (SA)	Non flexible	Gate electrode on gate oxide	Kang et al. [88]
HFET	single stranded DNA (ss-DNA)	DNA hybridization	Non flexible	Gate electrode on gate oxide	Kang et al. [131]
HFET	biotin SA	SA interferonγ (MIG)	Non flexible	Gate electrode on gate oxide	Gupta et al. [87]
SiNWFET	biotin	SA	Non flexible	Back gate	Cui et al. [106]
SiNWFET	peptide nucleic acid (PNA)	DNA mutation site	Non flexible	No reference electrode	Hahm et al. [104]
SiNWFET	Abl protein	ATP binding or inhibition	Non flexible	No reference electrode	Wang et al. [132]
SiNWFET	monoclonal antibodies (mAbs)	cancer markers	Non flexible	Wires connected to nano-wire	Zheng et al. [133]
SWNTFET	Aminated ssDNA	DNA hybridization	Non flexible	Back gate	Martinez et al. [107]
SWNTFET	PSA antibodies	prostate specific antigen (PSA)	Non flexible	Si substrate as gate	Li et al. [134]
GFET	graphene amines (GAs)	single bacterial cell	Non flexible	Si substrate as gate	Mohanty et al. [110]
GFET	BSA antibodies	bovine serum albumin (BSA)	Non flexible	Si substrate as gate	Ohno et al. [109]

There are FET-based sensors for which by definition the gate voltage is applied through an external reference electrode immersed in the electrolyte, with first and foremost the ion-sensitive FET. Bergveld realized that the external electrode is a practical problem during his first studies on ISFETs, but despite that, the conventional ISFET remains the most widely used FET sensor structure. Devices like ISFETs and their organic counterparts (ISOFETs), OECTs and electrolyte-gated OFETs need the external reference electrode to operate, while other structures such as the ISFGFET extended-gate FETs can operate either by using the external electrode or by an alternative mechanism. For these devices a second gate, called the control gate is used to modulate the main gate electrode voltage. The control gate configuration is also used by devices that exclusively function without the external electrode, like some floating-gate FETs and the charge-modulated FETs. However, the two gates are capacitively coupled, adding parasitic capacitances to the device.

FET-based devices with a metallic gate electrode deposited on top of the gate oxide, in contrast to the buried, electrically insulated floating gate electrode, also operate without an external electrode. Such devices are the conventional MOSFET sensor as well as EISFETs and DMFETs. Similarly, AlGaN/GaN based sensors can also function without a reference electrode, but some studies investigated the external gate bias configuration [135], [136], [137]. Another interesting alternative is using a back gate placed below the substrate or biasing the substrate to act as a back gate. This strategy has been followed for silicon-based sensors and forms the dual-gate FETs, but is also used in nanotechnology-based sensors. Finally, secondary electrodes like the control or the back gate can be avoided by implementing differential measurements between two identical sensors. Studies that investigate sensor operation without using an external gate electrode are summed up in Table 2.3.

2.7. Steps towards the BBB-on-chip

The overview of existing FET-based biosensors revealed some interesting designs that can inspire the next generation of the BBB-on-chip electrochemical sensor.

Some interesting FET-based configurations were identifying through the literature study, for application on the next generation of the BBB-on-chip electrochemical sensor. One of the main design parameters for the sensor is the embodiment or avoidance of the cumbersome reference electrode. Towards this end, differential measurements between two structurally identical transistors can reduce noise and lead to increased sensitivity. In the Bergveld ISFET review, this configuration is called REFET (Reference FET) and follow two types of measurements. In the first case, the aim is for one of the transistors to be completely insensitive to the measurement sample and for the other to be able to detect the target analyte. This is already challenging, as an electric double layer is expected to form on the insulated/insensitive transistor making the two transistors electrically non-identical. In the second case, two identical transistors are exposed to different samples, one with constant concentration and the other varying [18]. In a different configuration, Caboni *et al.* fabricated floating-gate transistors that share source and control-gate terminals to avoid common-mode noise [83]. However, differential measurements require an amplifier accompanied by a signal processing system to control signal amplification better, further complicating the design of the device [57], [66].

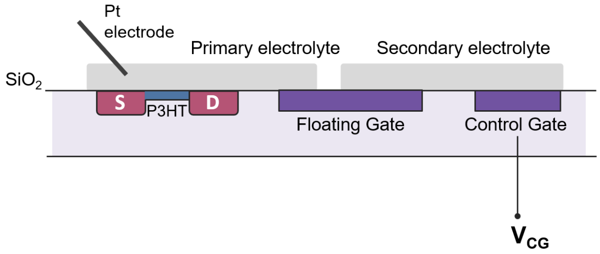

Figure 2.7: The electrolyte-gated FGFET (EG-FGFET) structure developed by White et.al.. An organic semiconductor (P3HT) forms the transistor's channel. The control gate is coupled to the floating gate through an ion gel (secondary electrolyte) and the floating gate modulates the channel though another ion gel (primary electrolyte). A platinum wire is immersed in the primary electrolyte.

Dual-gate FETs also show promising performances and their operation has been studied enough to be explained by theoretical models, but it is not clear why they have limited bio-related applications. The isolation of the sensing area and the implementation of flexible structures is essential for the BBB-on-chip, but it is not known if a dual-gate device would still operate effectively with an extended upper gate. The advantage of the two gates is the double modulation of the channel, with one interface on strong and the other on weak inversion, aiming at better channel control [34], [65].

Some studies made attempts at planar embodiment of the reference electrode [55], [121], [138], while another scientific team used the control-gate electrode in a planar geometry. This organic FET, the electrolyte-gated FGFET (EG-FGFET) combines an organic semiconductor channel with two gate electrodes and two electrolytes. The EG-FGFET structure is shown in Fig 2.7, where a high-capacitance ion gel acts as a gate dielectric and couples the semiconductor with the floating gate. The other side of the floating electrode is coupled to the control gate through an aqueous electrolyte [129]. A high-capacitance ion gel is chosen instead of solid dielectrics that exhibit lower capacitances to achieve higher threshold voltage shift [128]. EG-FGFETs operate on low voltages and their operating mechanism, still under investigation, is associated with capacitive effects and work function changes due to the target analyte/floating gate interaction [130]. In an effort of implementing a reference electrode in the fabrication of the BBB-on-chip the latter structure was further examined.

2.8. Final Remarks

The comparison Table 2.2 indicates that there is no optimal sensor geometry that exhibits high sensitivity and operation stability, which is also flexible, biocompatible and relies on CMOS fabrication techniques. Other criteria could be included, such as cost and material availability and it depends on the reader which aspect has a higher weight of importance. Nevertheless, the literature search indicated a variety of available technology for FET-based biosensors, including information on the selective layer options for detection of specific targets (look at Appendix A) for future studies.

Overall, the major FET-based sensor issues are already known, and more research should focus on the detection of analytes in physiological media and the implementation of flexible structures that promote biocompatibility. In some cases, focusing into the theoretical background and operation principles of the devices is suggested, as some structures' operation is not yet clearly comprehended. Similarly to the Debye screening limitation, other phenomena still hinder the sensitivity of FET biosensors and no certain method of overcoming them has been reported. Finally, the formation of the electrical double layer (EDL) on the sensing area/electrolyte interfaces and its effect on the sensing ability of the devices is not clear and thus commonly excluded from the theoretical models. Consequently, one of the main pillars of this project is studying the underlying mechanisms behind the developing sensor, while specifically aiming towards better comprehension of the EDL phenomenon.

In conclusion, the literature study revealed that each device architecture is associated with different advantages and drawbacks, leading to the conclusion that the combination of different device elements can be advantageous. The previously developed electro-chemical OoC incorporated floating-gate based FETs, in combination with floating-electrode extensions on a flexible and optically transparent membrane. This combined architecture benefits from regulating the sensor's operation by a control-gate instead of a reference electrode, while avoiding contact of the transducing part with the measurement medium and supporting a measurement environment compatible for cell cultures. Inspiration for taking this architecture a step forth, came through identifying structures of interest, such as the electrolyte-gated FGFET with the implementation of coplanar electrodes in the place of parallel capacitor plates. The mechanisms behind coplanar capacitors and electrolyte-gating are discussed in the following chapter.

3

Theoretical Background

This chapter introduces the necessary theoretical background that establishes the basis to further understand the operational principles of the main components of the BBB-on-chip. This includes an analytical description of the floating-gate FET operation, the theory behind ion-sensitive FGFETs and the inclusion of the electrical double layer effect, the establishment of coplanar capacitance theory and an introduction to pseudoreference electrodes. Each theoretical introduction is accompanied by a mathematical model, built for the next step of this thesis. A reasoning is provided for each presented model and their validity is tested based on experimental data. Assumptions that were introduced during model construction as well as possible shortcomings are discussed.

3.1. Floating-gate FET operation

The first generation OoC electro-chemical sensor is based on the floating gate configuration and operates on saturation mode. The structure of the sensor is schematically respresented in Fig 3.1. According to theory, on saturation mode the channel gets pinched off with a constant drain current passing through, called the saturation drain current I_D [139]. The equation that follows describes how the drain current is defined by the geometrical characteristics of the sensor and modulated by the applied voltages

$$I_D = \frac{1}{2}\mu_n C_{ox}\frac{W}{L}(V_{FG} - V_{TH})^2 \tag{3.1}$$

where μ_n is the electron mobility (for n-type transistor), C_{ox} is the gate oxide capacitance per unit area, and W and L are the width and length of the channel respectively. V_{FG} is the voltage of the floating gate and V_{TH} is the threshold voltage. It is indicated that the drain current I_D not only depends on the floating gate voltage V_{FG}, but it is also affected by the geometrical characteristics of the transistor and the materials of the device.

3.1.1. Floating-gate voltage

Subsequently, the floating gate potential is determined by the control- and sensing-electrode input, and by the residual charge inside the FG, Q_{F0}, that was trapped during the fabrication of the device [58], [140]. This trapped charge can affect the threshold voltage of the device V_{TH}, but techniques for identifying and if need be, removing the residual charge are known [26]. The insulated floating gate ensures uniform modulation of the semiconductor channel [63] and follows the charge conservation principle, stating that the floating gate charge must remain constant

$$Q_{F0} = Q_i + Q_{CG} + Q_{FB} \tag{3.2}$$

$$Q_{F0} = Q_i + C_{CF}(V_{FG} - V_{CG}) + C_{FB}V_{FG} \tag{3.3}$$

$$Q_{F0} = Q_i + V_{FG}(C_{CF} + C_{FB}) - C_{CF}V_{CG}) \tag{3.4}$$

$$V_{FG} = \frac{C_{CF}}{C_{CF} + C_{FB}}V_{CG} + \frac{Q_{F0} - Q_i}{C_{CF} + C_{FB}} \tag{3.5}$$

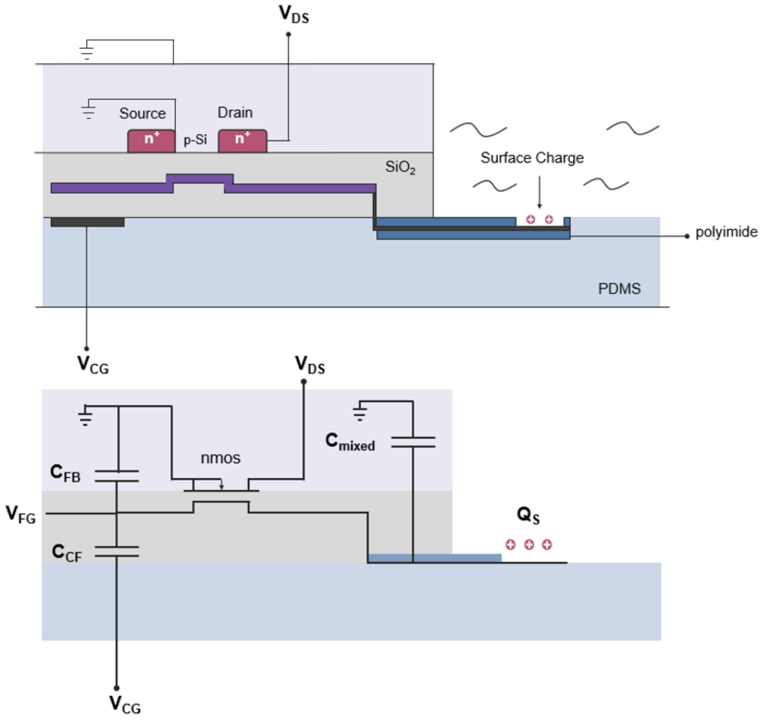

Figure 3.1: On top, cross-sectional schematic of the FGFET sensor including the different layers of materials. On the bottom, the corresponding electrical circuit. The capacitances of the system are incorporated in the mathematical model.

where Q_i is the induced charge on the oxide of the floating gate due to the sensing charge Q_s. Equation 3.5 practically shows how the control-gate regulates the voltage of the floating electrode while induced charge Q_i variations cause V_{FG} alterations. Standard electrostatic equations can describe the capacitances

$$C_{CF} = A_{CF}\frac{\epsilon_{ox}}{t_{p1p2}} + C_{fringe}P_{CF}, \qquad C_{FB} = A_{CF}\frac{\epsilon_{ox}}{t_{ox}} \tag{3.6}$$

where, A_{CF} is the floating gate area, t_{ox} is the thickness of the field silicon oxide, while t_{p1p2} is the oxide thickness between the two gate electrodes. The dielectric constant of the oxide is ϵ_{ox}. The fringe effect capacitance also contributes to the capacitance between floating and control gate, where P_{CF} is the perimeter of this capacitor.

3.1.2. Additional parasitic capacitance

The operation of the floating gate-based device is modulated by the control gate at the expense of signal attenuation due to the additional capacitive coupling between the floating and control gate electrodes. Additional parasitic capacitances can be added to the previous equations in an effort to predict the device operation with higher accuracy. A parallel plate capacitor is also formed between the floating gate and the source, and drain electrodes, C_{GS},C_{GD} respectively. The effect of these parasitic capacitances is commonly ignored in theoretical models due to the small source and drain terminal surface area (A_{GS},A_{GD}) compared to the floating gate area.

The structure of the OoC sensor dictates that the titanium part of the floating electrode extension is encapsulated in polyimide. A part of this sandwiched structure lays over the silicon substrate, thus forming a mixed dielectric capacitor between the titanium extension and the silicon body C_{mixed}, as seen in the diagram of Fig 3.1. This structure corresponds to two capacitors in series with the polyimide dielectric stacked over the silicon oxide. The mixed capacitance can be expressed as

$$C_{mixed} = \frac{\epsilon_{ox}\epsilon_{poly}A_{mixed}}{\epsilon_{poly}t_{p1p2} + \epsilon_{ox}t_{poly}} \tag{3.7}$$

where A_{mixed} is the area of the mixed dielectric capacitor plates, t_{poly} is the thickness of the polyimide layer and ϵ_{ox}, ϵ_{poly} the corresponding dielectric constants. The final form of equation 3.5 including all parasitic capacitances is similarly derived, resulting in

$$V_{FG} = \frac{C_{CF}}{C_{tot}} V_{CG} + \frac{C_{GD}}{C_{tot}} V_D + \frac{Q_{F0} - Q_i}{C_{tot}} \tag{3.8}$$

$$\text{where} \quad C_{tot} = C_{CF} + C_{parasitic} \quad \text{and} \quad C_{parasitic} = C_{FB} + C_{GS} + C_{GD} + C_{mixed} \tag{3.9}$$

Here V_D is the drain voltage that enters the equation after including capacitance C_{GD}. This model assumes that the connection between aluminium and titanium parts of the electrode is ideal without affecting the charge redistribution in the floating electrode.

3.1.3. Threshold voltage shift

Further, the assumption that the effect of the natural oxide on the titanium sensing pads is negligible means that when a charge Q_s binds on the sensing pad, it induces an opposite charge on the inner surface of the extension electrode $Q_s = -Q_i$. This charge causes a shift of the threshold voltage

$$V_{CG} - V_{THF} = V_{FG} - V_{TH} \tag{3.10}$$

$$V_{CG} - V_{THF} = \frac{C_{CF}}{C_{tot}} V_{CG} + \frac{C_{GD}}{C_{tot}} V_D + \frac{Q_{F0} - Q_i}{C_{tot}} - V_{TH} \tag{3.11}$$

$$V_{THF} = V_{TH} + (1 - \frac{C_{CF}}{C_{tot}}) V_{CG} - \frac{C_{GD}}{C_{tot}} V_D - \frac{Q_{F0} - Q_i}{C_{tot}} \tag{3.12}$$

$$V_{THF} \cong V_{TH} - \frac{C_{GD}}{C_{tot}} V_D - \frac{Q_{F0} - Q_i}{C_{tot}} \tag{3.13}$$

We consider that the parasitic capacitance is negligible in respect to the control capacitance, $C_{CF}/C_{tot} \cong 1$. Thus, the threshold voltage shift can be expressed as

$$\Delta V_{TH} = -\frac{\Delta Q_i}{C_{tot}} \tag{3.14}$$

as the rest of the terms remain constant. The equation indicates that both positive and negative charge cause a threshold voltage shift and thus the sensor can detect both entities.

3.1.4. Effect of the sensing area

The charge variation ΔQ_i as a result of the sensing charge Q_s, determines a superficial charge variation $\Delta\sigma_s$ on the sensing area. The distinct parts of the floating gate are also characterized by superficial charge variations, namely on the transducing part (A_T), the part underneath the control gate (A_{CF}) and the remaining parts of the electrode (A_R). Following once more the charge conservation principle

$$\Delta Q_i = -\Delta Q_s = \Delta Q_T + \Delta Q_{CF} + \Delta Q_R \tag{3.15}$$

$$\Delta Q_i = \Delta\sigma_T A_T + \Delta\sigma_{CF} A_{CF} + \Delta\sigma_R A_R \tag{3.16}$$

The charge is regulated by the control gate and has a fixed value ($\Delta\sigma_{CF} = 0$), and the area of the remaining floating gate parts is negligible compared to the area of the control gate ($A_R \ll A_{CF}$). So, at steady state the sensing charge variation only affects the transistor area and

$$\Delta Q_i = -\Delta\sigma_s A_s = \Delta\sigma_T A_T = \Delta Q_T \tag{3.17}$$

The assumption that only an insignificant charge redistribution happens on the non-critical parts of the floating gate was experimentally verified by Spanu et al. [81]. Thus, the following equation for the threshold voltage shift ΔV_{TH} can be safely derived by combining eq 3.14, 3.17

$$\Delta V_{TH} = -\frac{\Delta Q_T}{C_{tot}} = \frac{\Delta\sigma_s A_s}{C_{tot}} \tag{3.18}$$

is indicating the linear dependence between the transducting response of the sensor ΔV_{TH} and the sensing area size A_s.

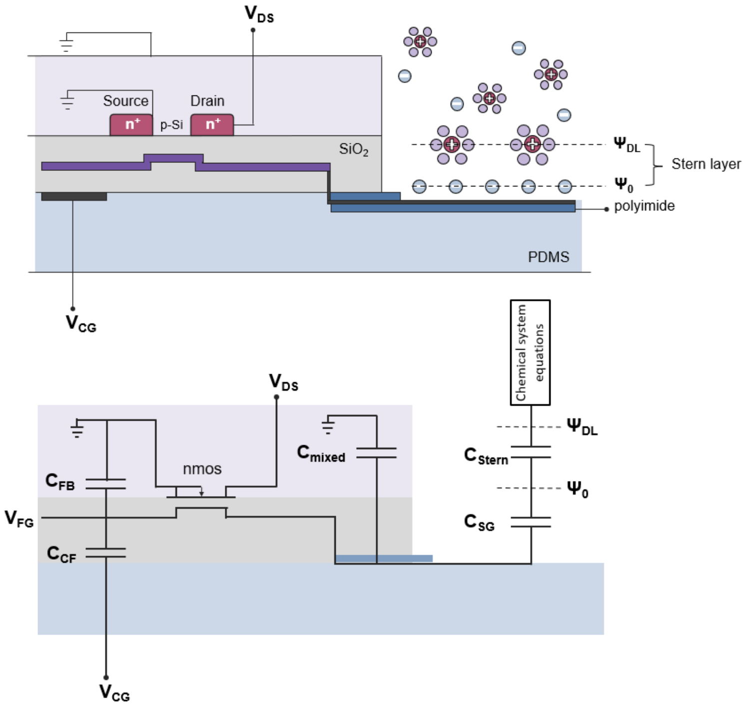

Figure 3.2: Cross-sectional schematic of the ISFGFET and its equivalent circuit. The solution in contact with the sensing pad is modeled as the capacitance C_{SG} between the inner Helmholtz plane and the electrode and capacitance C_{Stern} resulting from the Stern layer formation.

3.2. Ion-sensitive FGFET operation

The ISFET variant of the floating gate configuration has also been studied in an effort to combine the ionic interaction of ISFETs with the double-gate geometry of FGFETs. In this configuration, the device has two modes of operation: either applying the operation voltage through the control gate or by using a reference electrode immersed in the electrolyte. The electrolyte comes in contact with the sensing part of the floating gate, and the polarisation of the electrode modulates the drain current [60],[61]. Electrolytes permit free movement of ions but are electron and hole insulators. This is why when in contact with a charged electrode, ions of the opposite charge migrate towards the electrode, forming the two Helmholtz planes which constitute the electrical double layer (EDL), as explained in Section 2.5.

Upon contact between an electrolyte and the sensing pad of the BBB-on-chip FGFET, an electrical double layer is also expected to be formed at the electrode/electrolyte interface. This EDL capacitor can reach capacitance values up to three orders of magnitude higher than oxide dielectrics and is expected to play a significant role in the operation of the sensor [141]. Nevertheless, the effect of the EDL is only inserted into the mathematical models when a reference electrode is used, and yet all FET-based sensors are subjected to the Debye screening limitation, a phenomenon associated with EDL formation. There is, thus, an apparent need for identifying whether or not the inclusion of the EDL in theoretical models will increase their predictive performance.

3.2.1. Floating gate voltage and threshold voltage shift

Beginning with the basic principle of charge conservation for the floating gate electrode, similarly to the previous section, and including all parasitic charges

$$Q_{F0} = Q_s + Q_{CG} + Q_{FB} + Q_{GD} + Q_{GS} + Q_{mixed} \tag{3.19}$$

Here, the sensing charge Q_s that binds on the sensing pads is the charge of the capacitor between the inner Helmholtz layer and floating gate extension C_{SG}, as indicated in Fig 3.2. This is not a conventional parallel-plate capacitor but rather a metal/oxide/solution structure and is not well understood yet. The applied voltage on this capacitor is equal to the difference $\Psi_0 - V_{ref}$, where V_{ref} is the reference electrode voltage. The purpose of using the conventional bulky reference electrodes is mainly to maintain the applied voltage without fluctuations. By following a similar analysis to the previous section, it turns out that

$$V_{FG} = \frac{C_{SG}}{C_{tot}}(\Psi_0 - V_{ref}) + \frac{C_{CF}}{C_{tot}}V_{CG} + \frac{C_{GD}}{C_{tot}}V_D + \frac{Q_{F0}}{C_{tot}} \tag{3.20}$$

where $C_{tot} = C_{SG} + C_{CF} + C_{parasitic}$ and $C_{parasitic} = C_{FB} + C_{GS} + C_{GD} + C_{mixed}$ (3.21)

The voltage shift when all parameters are constant and the ISFGFET reacts only to the electrolyte effect, is derived from eq 3.20 by differentiating

$$\Delta V_{TH} = \frac{C_{SG}}{C_{tot}}\Delta\Psi_0 \tag{3.22}$$

indicating that the capacitance ratio C_{SG}/C_{tot} is an important design criterion that determines the performance of the sensor. This coupling ratio between C_{SG} and C_{tot} takes values between 0 and 1, limiting the sensitivity of the sensor in terms of threshold voltage shift because of the electrolyte effect.

3.2.2. Chemical system equations

The effect of the Stern layer is also introduced in the system as an additional capacitor C_{Stern}, shown in Fig 3.2. The potential on the upper limit of the Stern layer Ψ_{DL} is related to the other parameters of the model by

$$\sigma_{DL} = \frac{C_{Stern}}{A_s}(\Psi_0 - \Psi_{DL}) \tag{3.23}$$

where σ_{DL} is the surface charge of the double layer and A_s the sensing area. According to the model in [31], the Stern layer capacitance C_{Stern} is typically calculated assuming a dielectric constant of $10\epsilon_0$ and a charge separation of 50 nm. Following the previous equation, the double layer potential can be expressed as

$$\Psi_{DL} = \Psi_0 - \frac{\sigma_{DL}A_s}{C_{Stern}} \tag{3.24}$$

The surface charge of the sensing layer is expressed as

$$\sigma_{SG} = \frac{C_{SG}}{A_s}(V_{FG} - \Psi_0) \tag{3.25}$$

The total surface charge is then a combination of both double layer surface charge σ_{DL} and sensing surface charge σ_{SG} as

$$\sigma_0 = \sigma_{DL} - \sigma_{SG} \tag{3.26}$$

By combining eq 3.25 and 3.26 an expression for the sensing surface potential Ψ_0 is derived

$$\Psi_0 = V_{FG} - \frac{\sigma_{SG}A_s}{C_{SG}} = V_{FG} + \frac{(\sigma_0 - \sigma_{DL})A_s}{C_{SG}} \tag{3.27}$$

At this point, we have expressions for the critical voltages that modulate the operation of the FGFET. In order for the electrochemical system to be solved, one more equation is needed to describe the double layer surface charge, so according to the Grahame equation

$$\sigma_{DL} = \frac{2\epsilon_w\epsilon_0 kT}{e\lambda_D} sinh\left(\frac{e(\Psi_{DL} - V_{ref})}{2kT}\right) \tag{3.28}$$

where ϵ_w is the dielectric constant that characterises the electrolyte, assuming for simplicity equal to the constant of water, and λ_D is the Debye screening length.

A detailed overview of the chemical aspect of pH ISFGFET sensing is provided by Jayant et al. [142]. The protonated or deprotonated hydroxyl groups of the electrolyte bind to the inorganic oxide of the sensing area, forming a charged layer. This charged layer attracts counter ions, thus resulting in the electrical double layer. In this paper, theoretical models over the formation of the charged layers are described, focusing more on the chemical aspect. For this project, mathematical models are created based on the equations of the previous sections and considering a sensing charge Q_s, instead of pH, as an input.

Table 3.1: Basic equations describing the FGFET operation model

Parameter	**Equation**	**Description**
Geometry-related		
C_{CF}	$A_{CF}\frac{\epsilon_{ox}}{t_{p1p2}} + C_{fringe}P_{CF}$	Control gate-Floating gate capacitance [F]
C_{FB}	$A_{CF}\frac{\epsilon_{ox}}{t_{ox}}$	Floating gate-Silicon body capacitance [F]
C_{GS}	$A_{GS}\frac{\epsilon_{ox}}{t_{ox}}$	Floating gate-Source terminal capacitance [F]
C_{GD}	$A_{GD}\frac{\epsilon_{ox}}{t_{ox}}$	Floating gate-Drain terminal capacitance [F]
C_{mixed}	$\frac{\epsilon_{ox}\epsilon_{poly}A_{mixed}}{\epsilon_{poly}t_{p1p2}+\epsilon_{ox}t_{poly}}$	Mixed dielectric capacitor [F]
Model Input	$Q_s = -Q_i$	Sensing charge [C]
Model Output		
V_{FG}	$\frac{C_{CF}}{C_{tot}}V_{CG} + \frac{C_{GD}}{C_{tot}}V_D + \frac{Q_{F0}-Q_i}{C_{tot}}$	Floating gate voltage [V]
ΔV_{TH}	$-\frac{\Delta Q_i}{C_{tot}}$	Threshold voltage shift [V]
I_D	$\frac{1}{2}\mu_n C_{ox}\frac{W}{L}(V_{FG} - V_{TH})^2$	Drain current [A]

3.3. Mathematical model validation

The equations derived in the previous sections form two different theoretical models:

- the FGFET model, where the sensing operation is based on the binding of sensing charge Q_S, without taking into account the chemical phenomena between sensing electrode and electrolyte.
- the ISFGFET model which includes the effect of the electrical double layer formation.

These models are going to be compared with experimental measurements by the end of the project, to determine which model better predicts the sensor's behaviour and indicating whether the inclusion of the EDL effect is advantageous. The critical equations that describe each model are shown in Tables 3.1 and 3.2 for the reader's convenience. At first, the models are validated by using measurement data from previously fabricated sensors. The measurement set-up is described in Chapter 6. Consequently, the prediction ability of the models can be examined, to justify their use in the designing process discussed in the next chapter.

3.3.1. FGFET model validation

The effectiveness of the simple FGFET model is tested by a simple Matlab script and a simulation software, the advanced design system (ADS) by Keysight Technologies. Modelling a floating node configuration can be challenging, especially in the case of SPICE simulators, so in a previous effort a bachelor graduation project undertook the modelling of the FGFET-based sensor in ADS. The schematic overview of the ADS circuit and more information on the ADS model are presented in Appendix B. Overall, the difference between the Matlab script and the ADS simulation is the way the output, namely the drain current I_{DS} and the floating gate voltage V_{FG}, are derived. In the script they result from equations, while in ADS they are the simulation's output.

In Fig 3.3, the transfer characteristics derived from the ADS model are presented. On the left, the ADS model is compared with the Matlab script and the measurement and it illustrates an efficient fit, while being more accurate for higher drain voltage V_{DS} values in relation to the Matlab model. On the right, the effect of the added parasitic capacitances of section 3.1.2 is examined. It is illustrated that for the dimensions of the fabricated transistor, the extra parasitic capacitances due to source, drain and first polyimide layer are insignificant. This result agrees with previous FGFET-studies where the effect of these parameters is considered negligible. Nevertheless, the examination of their effect is strongly

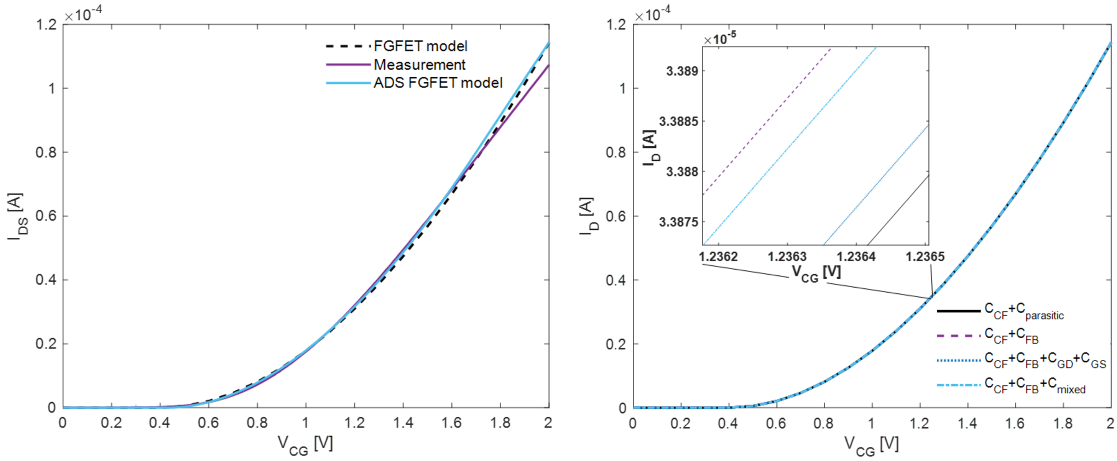

Figure 3.3: On the left, transfer characteristics of previously fabricated FGFET-based sensor in dry conditions are compared to the FGFET equation model including all parasitic capacitances and the ADS-based model including the effect of interconnect resistances. The applied drain voltage is V_D=100mV. On the right, the effect of the secondary parasitic capacitances is illustrated as predicted by the Matlab model.

recommended, as it varies based on the geometry of the FGFET, and it can be easily implemented to the models.

The ADS platform provides an easy and fast way to extract both the transfer and output characteristics of a transistor. The Matlab scripts only describe the operation of the FGFET on saturation mode and thus, the output characteristics are only examined in the ADS model. Figure 3.4 illustrates the ADS simulation data in comparison with measurement data in dry conditions for different values of control-gate voltage V_{CG}. The fit is satisfactory, indicating that just by tuning MOSFET parameters while following the transistor's geometry, the ADS model can be used for predictive purposes. It has to be noted that even though the fabrication of the FGFET sensor in cleanroom facilities promises high replicability, there is a high chance that an FGFET with the same dimensions will have a slightly different performance. Nevertheless, it is expected that both Matlab and ADS models yield a meaningful insight into the operation of the FGFET sensor.

The ADS model can also incorporate the effect of the interconnect resistances by considering

$$R = \frac{l}{\sigma A} \tag{3.29}$$

where l is the length of the interconnecting electrode, A the cross-sectional area of the conductor and σ the electrical conductivity of the material, in this case aluminum. On the right of Fig 3.4, the role of the connecting electrodes is examined. As expected, the inclusion of these resistances in the ADS model predicts lower performance, but not significantly.

3.3.2. ISFGFET model validation

The ISFGFET model is based on the equations that summarised in Table 3.2. It describes the behaviour of the sensor in wet conditions. An electrolyte is needed for the formation of the EDL in proximity to the sensing area. That is under the assumption that the double layer can be formed without applying a voltage through a conventional reference electrode but as a result of the polarised floating electrode. For illustrative purposes, the result of the mathematical model is shown in comparison with the previously plotted measurement and the corresponding ADS model in Fig 3.5. The sensor's operation varies between dry and wet conditions, indicating higher drain current values when in contact with an electrolyte. This is expected as charged entities from the electrolyte in proximity to the sensing area will affect the charge redistribution in the floating electrode. The ISFGFET model can not, by definition, express the sensor's behaviour under dry conditions.

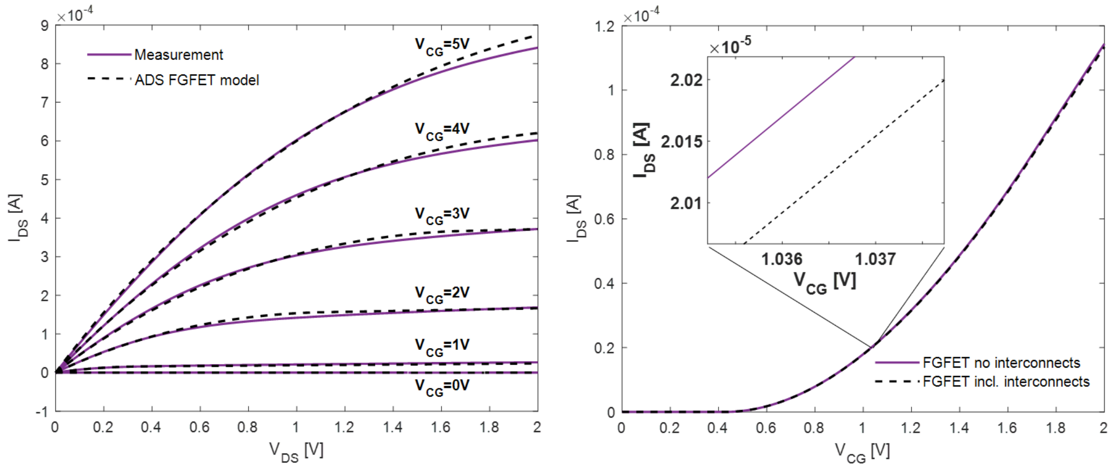

Figure 3.4: On the left, output characteristics of previously fabricated FGFET-based sensor in dry conditions and the corresponding ADS-extracted data. On the right, the effect of the interconnect resistance based on the ADS model is shown.

The input of the Matlab ISFGFET model is the sensing charge Q_S, while the previously created ADS ISFGFET model considers pH as the input (more information can be found in Appendix B). In Fig 3.5, the results of both models are plotted together, indicating different behaviours. In contrast with the dry measurement, both models predict the sensor's output under wet conditions where ions from the electrolyte bind on the sensing area, thus inducing a threshold voltage shift. A different behaviour was expected for the ADS model, as the concentration of protons $[H^+] = 10^{-1}[mol/m^3]$ in the solution is significant and still the output closely resembles the dry measurement results. For future work, measurements in wet conditions, initially with neutral buffers, can help identify which model replicates the sensor's behaviour better.

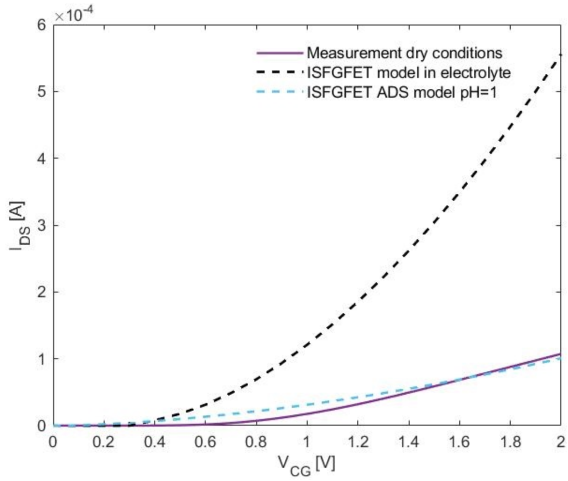

Figure 3.5: Transfer characteristics of previously fabricated FGFET-based sensor in dry conditions compared to the results of two models. The mathematical ISFGFET model illustrates the sensor behaviour under wet conditions, assuming that the bound sensing charge Q_S is approximately zero. The ADS model derives the drain current based on the medium pH and not based on the bound charge. In all cases, the applied voltage is V_{DS}=100mV.

3.4. Coplanar Capacitance Theory

Among the FET-based configurations examined during the literature study, a structure implementing coplanar capacitors was identified, as shown in Fig 3.6. In this structure, developed by White et al. [128], two planar electrodes take the place of the conventional parallel plate capacitor formed between

Table 3.2: Basic equations describing the ISFGFET operation model, including the effect of the electrical double layer (EDL)

Parameter	Equation	Description
Geometry-related		
C_{SG}	$A_s \frac{\epsilon_{TiO_2}}{t_{TiO_2}}$	Sensing gate capacitance [F]
C_{CF}	$A_{CF} \frac{\epsilon_{ox}}{t_{p1p2}} + C_{fringe} P_{CF}$	Control gate-Floating gate capacitance [F]
C_{FB}	$A_{CF} \frac{\epsilon_{ox}}{t_{ox}}$	Floating gate-Silicon body capacitance [F]
C_{GS}	$A_{GS} \frac{\epsilon_{ox}}{t_{ox}}$	Floating gate-Source terminal capacitance [F]
C_{GD}	$A_{GD} \frac{\epsilon_{ox}}{t_{ox}}$	Floating gate-Drain terminal capacitance [F]
C_{mixed}	$C_{mixed} = A_{mixed} \epsilon_{ox} \epsilon_{poly} + \frac{1}{\epsilon_{poly} t_{p1p2} + \epsilon_{ox} t_{poly}}$	Mixed dielectric capacitor [F]
C_{Stern}	$A_s \frac{10\epsilon_0}{50nm}$	Stern layer capacitance [F]
Model Input	$\sigma_0 = \frac{Q_s}{A_s}$	Sensing area surface charge [C/m^2]
Model Output		
V_{FG}	$\frac{C_{SG}}{C_{tot}}(\Psi_0 - V_{ref}) + \frac{C_{CF}}{C_{tot}} V_{CG} + \frac{C_{GD}}{C_{tot}} V_D + \frac{Q_{F0}}{C_{tot}}$	Floating gate voltage [V]
ΔV_{TH}	$\frac{C_{SG}}{C_{tot}} \Delta \Psi_0$	Threshold voltage shift [V]
I_D	$\frac{1}{2} \mu_n C_i \frac{W}{L} (V_{FG} - V_{TH})^2$	Drain current [A]
Ψ_{DL}	$\Psi_0 - \frac{\sigma_{DL}}{C_{Stern}}$	Double layer potential [V]
Ψ_0	$V_{FG} + \frac{\sigma_0 - \sigma_{DL}}{C_{SG}}$	Sensing surface potential [V]
σ_{DL}	$\frac{2\epsilon_w \epsilon_0 kT}{e\lambda_D} sinh\left(\frac{e(\Psi_{DL} - V_{ref})}{2kT}\right)$	Double layer surface charge [C/m^2]
σ_0	$\sigma_{DL} - \sigma_{SG}$	Total surface charge [C/m^2]

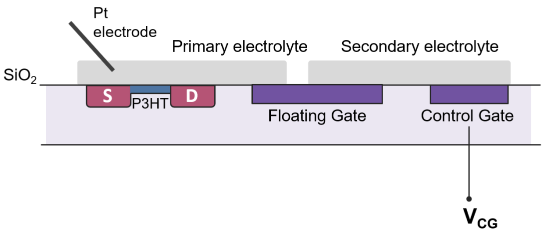

Figure 3.6: The electrolyte-gated FGFET (EG-FGFET) structure developed by White et.al.. An organic semiconductor (P3HT) forms the transistor's channel. The control gate is coupled to the floating gate through an ion gel (secondary electrolyte) and the floating gate modulates the channel though another ion gel (primary electrolyte). A platinum wire is immersed in the primary electrolyte.

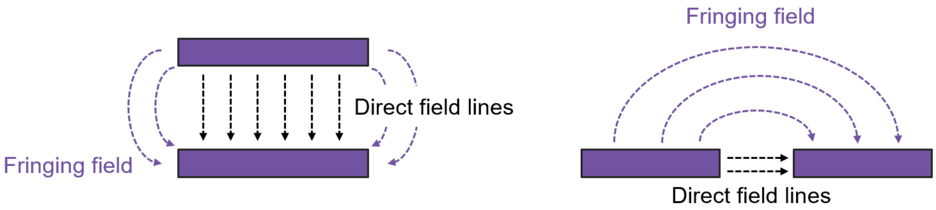

Figure 3.7: Cross-sectional illustration of the difference between parallel-plate capacitor and coplanar configuration of electrodes. The lines indicate the direction of the electric field.

floating and control gate. The planar electrodes are connected through an aqueous electrolyte and the device behaves like a conventional FGFET. Thus, the coplanar capacitor has been proven operational, but the theory behind its function is yet to be discussed. For illustrative purposes, the difference on the resulting electric fields between a parallel plate capacitor and a coplanar one is shown in Fig 3.7.

The capacitance between two coplanar flat conductors is considered the sum of direct field capacitance on the x-axis as shown in Fig 3.8 and the fringing effect. When two conductor plates of length l, width w and thickness h are placed one next to the other at a distance $d = 2a$, the voltage V as a result of the direct electric field E can be expressed as

$$V = -\int_0^{2a} \vec{E} \cdot \overrightarrow{dl} = E \cdot 2a \tag{3.30}$$

so the capacitance resulting from the direct field is

$$C = \frac{Q}{V} = \frac{\sigma A}{E2a} = \frac{\epsilon A}{2a} \tag{3.31}$$

where A is the cross-sectional area of the direct field capacitor and the permittivity ϵ is equal to σ/E according to the first Maxwell's equation.

As the dimensions of the conductor plates get smaller towards the micro- and nano-scale the fringing effect gets more significant [143]. Coplanar electrodes can detect changes in their dielectric environment thanks to the fringing effect. As a result, coplanar capacitors find application as proximity sensors and can be used for dielectric material properties characterisation [144]. Conformal mapping techniques derive the distribution of the electric field around the two planar electrodes, as analytically described by Chen et al. [145]. Assuming that the width of each electrode w is negligible in comparison with its length l ($l \gg w$) (in the z-direction) and that they have the same dimensions, the capacitance can be calculated according to

$$C_{cp} = \frac{Q}{2V_0} = \frac{2\epsilon_r \epsilon_0 l}{\pi} ln\left[\left(1+\frac{w}{a}\right) + \sqrt{\left(1+\frac{w}{a}\right)^2 - 1}\right] \tag{3.32}$$

where Q is the charge on one electrode, ϵ_r the relative permittivity of the dielectric and a is half the distance between the two electrodes $a = d/2$, as seen in Fig . The coplanar capacitance C_{cp} does not depend on the height of the electrodes and equation 3.32 is strictly valid only when $w \gg a$. For higher values of the w/a ratio, the coplanar capacitance is identified through analytical methods and not through a closed-form solution.

Considering the design of the sensor in Fig 3.2 intact, an additional planar electrode can be placed in proximity to the sensing pad on the PDMS well. In this configuration, a coplanar capacitor with C_{cp} expressed by equation 3.32 is formed between the new electrode and the sensing pad. The sensor can thus operate on three modes:

- by applying voltage through the conventional control gate
- by applying voltage through the planar electrode

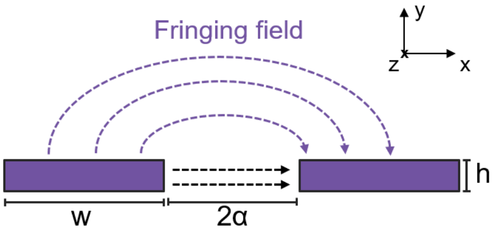

Figure 3.8: Cross-sectional illustration of coplanar electrode configuration with geometric parameters. a is the half distance between the electrodes.

- by applying voltage to both electrodes, a dual-operation mode

3.4.1. Coplanar capacitor mathematical model

There are two possible implementations of the coplanar capacitance in the FGFET model explained in section 3.3. Firstly, it can be assumed that the charge Q_s binding on the sensing pad is the charge of the coplanar capacitor

$$Q_s = C_{cp}2V_{cp} = \frac{2\epsilon_r\epsilon_0 l}{\pi} ln\left[\left(1+\frac{w}{a}\right)+\sqrt{\left(1+\frac{w}{a}\right)^2-1}\right]2V_{cp} \tag{3.33}$$

As a result, the voltage applied on the planar electrode V_{cp}, for definite electrode dimensions, controls the bound charge on the sensing area Q_s. This means that by following the charge conservation principle

$$Q_{F0} = Q_s + Q_{CG} + Q_{FB} + Q_{GD} + Q_{GS} + Q_{mixed} \tag{3.34}$$

and inserting the equation for the coplanar capacitance C_{cp}, after following the same steps as before, it turns out that

$$V_{FG} = \frac{C_{cp}}{C_{tot}}V_{cp} + \frac{C_{CF}}{C_{tot}}V_{CG} + \frac{C_{GD}}{C_{tot}}V_D + \frac{Q_{F0}}{C_{tot}} \tag{3.35}$$

where

$$C_{tot} = C_{cp} + C_{CF} + C_{FB} + C_{GD} + C_{SD} + C_{mixed} \tag{3.36}$$

It is indicated that the floating gate voltage V_{FG} is affected by both control gate and planar electrode terminals in this configuration. As already mentioned, when a voltage is applied to the planar electrode, the sensing charge is determined and remains constant. Thus, the threshold voltage shift ΔV_{TH} is expected to be a function of V_{cp}.

In order to mathematically prove that, we derive an expression for the threshold voltage shift V_{TH}. The same principle with the FGFET model is followed. Based on equation 3.10 and adjusting for the current structure

$$V_{CG} + V_{cp} - V_{THF} = V_{FG} - V_{TH} \tag{3.37}$$

$$V_{THF} = V_{TH} + \left(1-\frac{C_{CF}}{C_{tot}}\right)V_{CG} + \left(1-\frac{C_{cp}}{C_{tot}}\right)V_{cp} - \frac{C_{GD}}{C_{tot}}V_D - \frac{Q_{F0}}{C_{tot}} \tag{3.38}$$

Assuming $C_{CF} >> C_{tot}$ and $C_{cp} << C_{tot}$, the effective threshold voltage V_{THF} is

$$V_{THF} = V_{TH} + \frac{C_{cp}}{C_{tot}}V_{cp} - \frac{C_{GD}}{C_{tot}}V_D - \frac{Q_{F0}}{C_{tot}} \tag{3.39}$$

All terms of the equation above are constant and a threshold voltage shift is only noted for altering values of V_{cp} and V_D

$$\Delta V_{TH} = \frac{C_{cp}}{C_{tot}}V_{cp} - \frac{C_{GD}}{C_{tot}}V_D \tag{3.40}$$

The operation principle of the sensor is still the same with the conventional FGFET device. Thus, the same equation could be directly derived from equation 3.14 by substituting $-\Delta Q_i = \Delta Q_s$ with $C_{cp}V_{cp}$.

Table 3.3: Basic equations describing the FGFET model including a planar electrode

Parameter	**Equation**	**Description**
Geometry-related		
C_{CF}	$A_{CF}\frac{\epsilon_{ox}}{t_{p1p2}} + C_{fringe}P_{CF}$	Control gate-Floating gate capacitance [F]
C_{FB}	$A_{CF}\frac{\epsilon_{ox}}{t_{ox}}$	Floating gate-Silicon body capacitance [F]
C_{GS}	$A_{GS}\frac{\epsilon_{ox}}{t_{ox}}$	Floating gate-Source terminal capacitance [F]
C_{GD}	$A_{GD}\frac{\epsilon_{ox}}{t_{ox}}$	Floating gate-Drain terminal capacitance [F]
C_{mixed}	$C_{mixed} = A_{mixed}\epsilon_{ox}\epsilon_{poly} + \frac{1}{\epsilon_{poly}t_{p1p2}+\epsilon_{ox}t_{poly}}$	Mixed dielectric capacitor [F]
C_{cp}	$\frac{2\epsilon_r\epsilon_0 l}{\pi} ln\left[\left(1+\frac{w}{a}\right)+\sqrt{\left(1+\frac{w}{a}\right)^2-1}\right]$	Coplanar capacitance between sensing pad
	$+\frac{\epsilon_r\epsilon_0 wh}{2a}$	and planar electrode [F]
Model Input	$Q_s = C_{cp}2V_{cp}$	Sensing charge [C]
Model Output		
V_{FG}	$\frac{C_{cp}}{C_{tot}}V_{cp} + \frac{C_{CF}}{C_{tot}}V_{CG} + \frac{C_{GD}}{C_{tot}}V_D + \frac{Q_{F0}}{C_{tot}}$	Floating gate voltage [V]
ΔV_{TH}	$\frac{\Delta Q_s}{C_{tot}}$	Threshold voltage shift [V]
I_D	$\frac{1}{2}\mu_n C_i \frac{W}{L}(V_{FG} - V_{TH})^2$	Drain current [A]

3.4.2. Second coplanar mathematical model

In the second case, coplanar capacitance is formed between sensing and planar electrode, but the charge binding on the sensing pad is considered an independent phenomenon. This means that both terms Q_s and Q_{cp} are inserted in the charge conservation principle, yielding

$$Q_{F0} = Q_s + Q_{CG} + Q_{FB} + Q_{GD} + Q_{GS} + Q_{mixed} + Q_{cp} \tag{3.41}$$

and similarly to the previous derivations

$$V_{FG} = \frac{C_{cp}}{C_{tot}}V_{cp} + \frac{C_{CF}}{C_{tot}}V_{CG} + \frac{C_{GD}}{C_{tot}}V_D + \frac{Q_{F0} - Q_i}{C_{tot}} \tag{3.42}$$

where

$$C_{tot} = C_{CF} + C_{FB} + C_{GD} + C_{SD} + C_{mixed} + C_{cp} \tag{3.43}$$

So, the total parasitic capacitance remains the same, but an additional term is added in the floating gate voltage equation. According to the new V_{FG}, the threshold voltage shift is

$$V_{THF} = V_{TH} + \left(1 - \frac{C_{CF}}{C_{tot}}\right)V_{CG} - \left(1 - \frac{C_{cp}}{C_{tot}}\right)V_{cp} - \frac{C_{GD}}{C_{tot}}V_D - \frac{Q_{F0} - Q_i}{C_{tot}} \tag{3.44}$$

$$V_{THF} = V_{TH} - \frac{C_{cp}}{C_{tot}}V_{cp} - \frac{C_{GD}}{C_{tot}}V_D - \frac{Q_{F0} - Q_i}{C_{tot}} \tag{3.45}$$

$$\Delta V_{TH} = -\frac{\Delta Q_i}{C_{tot}} \tag{3.46}$$

assuming that the drain voltage V_D and coplanar voltage V_{cp} are constant.

The two models do not show significant differences, especially considering that the coplanar capacitance is expected to be significantly lower than the control gate capacitance. However, even minor variations between the models can give an insight on how to better replicate the behaviour of the sensor.

Table 3.4: Basic equations describing the second FGFET model including a planar electrode

Parameter	**Equation**	**Description**
Model Input	$Q_s = -Q_i$	Sensing charge [C]
Model Output		
V_{FG}	$\frac{C_{cp}}{C_{tot}}V_{cp} + \frac{C_{CF}}{C_{tot}}V_{CG} + \frac{C_{GD}}{C_{tot}}V_D + \frac{Q_{Fo}-Q_i}{C_{tot}}$	Floating gate voltage [V]
ΔV_{TH}	$-\frac{\Delta Q_i}{C_{tot}}$	Threshold voltage shift [V]

3.4.3. Coplanar models validation

In comparison with the simple FGFET model of section 3.3, the coplanar model includes an additional parasitic capacitance C_{cp}, which becomes more significant for dielectric materials with higher relative permittivity. For clarity, the equations describing the mathematical model for an FGFET structure additionally implementing a planar electrode are shown in Table 3.3.

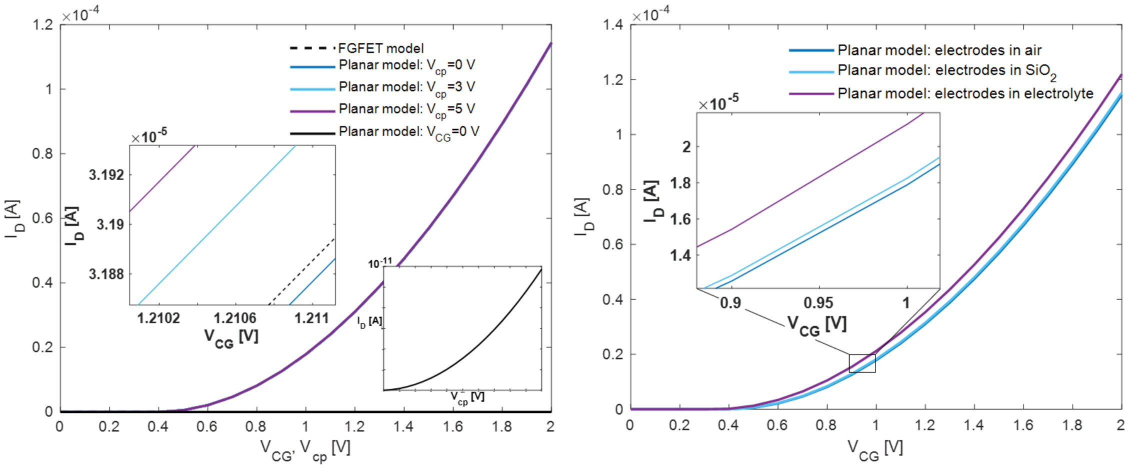

Figure 3.9: Transfer characteristics derived from the first coplanar model. It is assumed that the sensing charge is determined by the coplanar capacitor C_{cp}. On the left, the results of biasing the control gate V_{CG} for different values of planar electrode voltage V_{cp}. The results of operating the device based solely on V_{cp} are also illustrated. On the right, the effect of the sensing well medium is examined. In all cases, the applied voltage is V_{DS}=100mV.

The dimensions of the FGFET in the model remain the same, while assuming coplanar electrode dimensions as following: a length l of 3mm, a width w of 150 μm and a separation of $2a$ 160 μm. These arbitrary dimensions were chosen to check the effect of the model while still being compatible with the general dimensions of the sensor. The electrodes should fit into the well area and the width should not be impeding the visibility of the well.

For model validation, the transfer characteristics deriving from the Matlab script with the equations of Table 3.3 are plotted. By applying voltage only through the new planar electrode V_{cp} (V_{CG}=0), the FGFET behaves like a transistor and enters saturation regime (see Fig 3.9 .left). However, the drain current I_D values are in the order of 10^{-11} A. This is explained by the low C_{cp} $10^{-14}F$, a value comparable to the parasitic capacitance between source (and drain) terminal and the silicon body $C_{GD,GS}$. In this operation mode, the critical capacitance of the structure remains the one between control and floating gate C_{CF}. Thus, operation based solely on biasing the planar electrode is not promising.

The effect of biasing both control gate and planar electrode are shown on the left part of Fig 3.9. The FGFET operation is modulated by the control gate voltage V_{CG}, with the coplanar voltage V_{cp} causing a slight shift on the drain current values. For higher V_{cp} a shift towards higher I_D values is indicated, while in the case of V_{cp}=0 there is a shift towards lower values. The difference is that for the coplanar model the total parasitic capacitance is higher than that of the FGFET model.

The effect of the dielectric separating sensing pad from the planar electrode is examined on the right part of Fig 3.9. Utilising different dielectrics is translated into applying different relative permittivities ϵ_r. This is rather a simplistic approach that ignores chemical interactions between the electrodes and the electrolyte or the liquid measurement medium. As seen in Fig 3.9, media with higher relative permittivities, such as an electrolyte lead to steeper transfer characteristics. So far, the implementation of a coplanar electrode yields slightly higher drain current values, on double-bias operation.

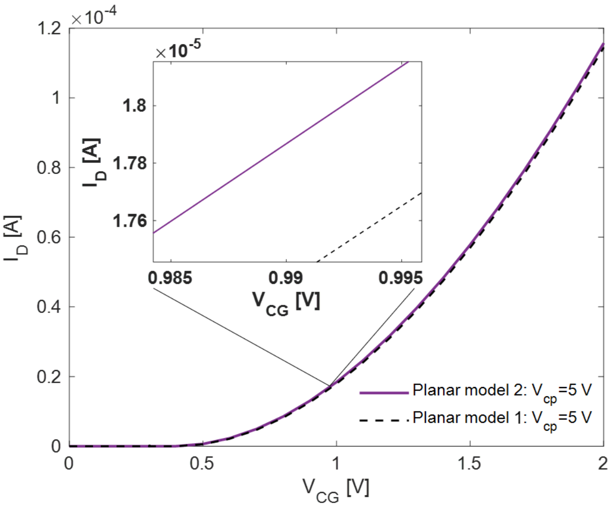

Figure 3.10: Transfer characteristics derived from the first and second coplanar model. The sensor operates by applying bias on both control gate and coplanar electrode. The applied drain voltage is V_{DS}=100mV.

For this model, the mathematical expressions for the floating gate voltage and threshold voltage shift are noted for convenience in Table 3.4. The comparison between the two models is illustrated in Fig 3.10. As expected, the two models predict very similar behaviour, with the second one indicating slightly higher drain current values for the same value of Q_s. The second model predicts an extra charge that modulates the floating gate voltage, other than the charge induced by the coplanar capacitor.

3.4.4. Coplanar electrode configuration in ADS

Both previous models indicate that an extra parasitic capacitance C_{cp} is inserted in the system. This capacitance can easily be incorporated in the ADS FGFET model, as seen in the ADS schematic in appendix B. A DC voltage source corresponding to the applied voltage V_{cp} on the planar electrode is implemented on one of the capacitor terminals. On the other terminal, the node is connected to the floating gate. The geometric parameters of the planar electrode are inserted into the model and the equations describing the operation of the sensor are modified based on tables 3.3, 3.4. Both mathematical and ADS model are based on the same system of equations, so a similar output is expected, as seen in Fig 3.11.

3.5. Pseudoreference electrode theory

The development of fully miniaturised platforms such as the organ-on-chip has led to planar reference electrode implementation. Several scientific teams have worked towards this aim, including efforts identified during the literature search [37]. Five studies integrated a reference, or more cor-

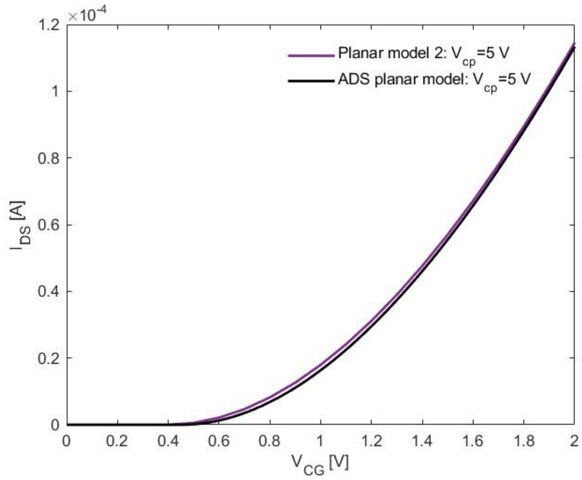

Figure 3.11: Transfer characteristics of the FGFET-based sensor with an additional planar electrode. In dry conditions, the second mathematical coplanar model is compared to the coplanar ADS model. The dielectric between floating and planar electrode is air. The applied voltage is V_{DS}=100mV.

Table 3.5: System of equations describing the operation of an FGFET with an integrated pseudoreference electrode

Parameter	Equation	Description
Geometry-related		
C_{SG}	$A_s \frac{\epsilon_{TiO_2}}{t_{TiO_2}}$	Sensing gate capacitance [F]
C_{CF}	$A_{CF} \frac{\epsilon_{ox}}{t_{p1p2}} + C_{fringe} P_{CF}$	Control gate-Floating gate capacitance [F]
C_{FB}	$A_{CF} \frac{\epsilon_{ox}}{t_{ox}}$	Floating gate-Silicon body capacitance [F]
C_{GS}	$A_{GS} \frac{\epsilon_{ox}}{t_{ox}}$	Floating gate-Source terminal capacitance [F]
C_{GD}	$A_{GD} \frac{\epsilon_{ox}}{t_{ox}}$	Floating gate-Drain terminal capacitance [F]
C_{mixed}	$C_{mixed} = A_{mixed} \epsilon_{ox} \epsilon_{poly} + \frac{1}{\epsilon_{poly} t_{p1p2} + \epsilon_{ox} t_{poly}}$	Mixed dielectric capacitor [F]
C_{cp}	$\frac{2\epsilon_r \epsilon_0 l}{\pi} ln\left[\left(1 + \frac{w}{a}\right) + \sqrt{\left(1 + \frac{w}{a}\right)^2 - 1}\right]$	Coplanar capacitance between sensing
	$+ \frac{\epsilon_r \epsilon_0 wh}{2a}$	and planar electrode [F]
C_{Stern}	$A_s \frac{10\epsilon_0}{50nm}$	Stern layer capacitance [F]
Model Input	$\sigma_0 = \frac{Q_s}{A_s}$	Sensing area surface charge [C/m^2]
Model Output		
V_{FG}	$\frac{C_{SG}}{C_{tot}}(\Psi_0 - V_{ref}) + \frac{C_{cp}}{C_{tot}} V_{ref} + \frac{C_{CF}}{C_{tot}} V_{CG} + \frac{C_{GD}}{C_{tot}} V_D + \frac{Q_{F0}}{C_{tot}}$	Floating gate voltage [V]
ΔV_{TH}	$\frac{C_{SG}}{C_{tot}} \Delta\Psi_0$	Threshold voltage shift [V]
I_D	$\frac{1}{2} \mu_n C_i \frac{W}{L} (V_{FG} - V_{TH})^2$	Drain current [A]
Ψ_{DL}	$\Psi_0 - \frac{\sigma_{DL}}{C_{Stern}}$	Double layer potential [V]
Ψ_0	$V_{FG} + \frac{\sigma_0 - \sigma_{DL}}{C_{SG}}$	Sensing surface potential [V]
σ_{DL}	$\frac{2\epsilon_w \epsilon_0 kT}{e\lambda_D} sinh\left(\frac{e(\Psi_{DL} - V_{ref})}{2kT}\right)$	Double layer surface charge [C/m^2]
σ_0	$\sigma_{DL} - \sigma_{SG}$	Total surface charge [C/m^2]

rectly, a pseudoreference electrode on MOSFET structures, aiming both for higher miniaturisation and higher sensor performance. In one case, in the study by Prodromakis et al., the effect of the integrated electrode was reported as erratic and substituted by a conventional Ag/AgCl reference electrode [55]. The basic idea behind a reference electrode is that it creates an electrical field, biasing the measurement solution, affecting the sensor's measurement. It is also theorised that reference electrode usage also counteracts the trapped charged in the floating gate configuration [146].

The implementation of an additional planar electrode in the sensing well area can, thus, either be translated as a coplanar capacitance affecting the operation of the sensor, or as the implementation of a pseudoreference electrode. The pseudoreference electrode, usually just a metal wire, does not exhibit stable potential, because it does not operate under thermodynamic equilibrium. Even though there have been efforts towards planar implementation of the conventional Ag/AgCl reference electrode, the fabrication is not CMOS compatible. On the other hand, pseudoreference electrodes are wires or layers made of chemically resistant materials, such as platinum, gold and silver, dipped in the electrolyte. In some cases, very stable potentials were noted for pseudoreference electrodes in ionic liquids, but their operation depends on the measurement conditions. Pseudoreference electrodes operate effectively on a limited range of conditions (such as pH, temperature), where they do not show chaotic behaviour [37], [38].

To sum up, a pseudoreference electrode dipped in an electrolyte creates an electric field that affects the distribution of ions in the electrolyte. However, the electrode voltage V_{ref} is not maintained constant and it is not possible to identify due to thermodynamic imbalance. This renders the pseudoreference-electrolyte-sensing pad interaction a complex system that a closed-form analytical solution might not possibly describe.

3.5.1. Pseudoreference electrode model

A simplistic analytical model is proposed here, combining the theory of the previous chapters. The pseudoreference electrode is a charged electrode, which means that an electrical double layer will be formed on its surface and the exposed sensing pad's surface. As a result, the system of equations that dictate the EDL effect in section 3.2 can be used.

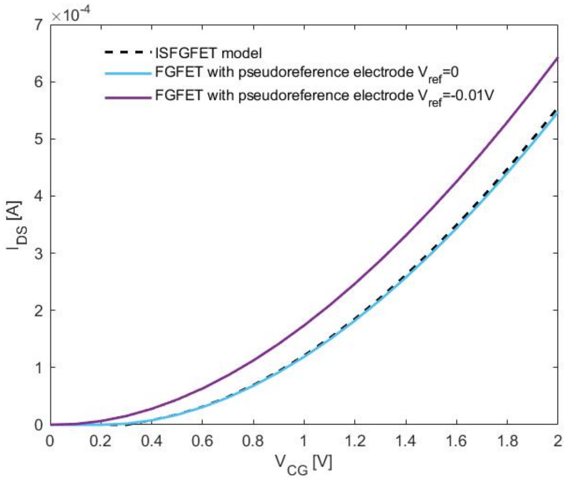

Figure 3.12: Transfer characteristics of the FGFET-based sensor with integrated pseudoreference sensor compared to the ISFGFET mathematical model. The applied voltage is V_{DS}=100mV.

By placing the pseudoreference electrode in proximity to the sensing pad in the coplanar configuration, the attenuation of the electric field is avoided. Consequently, we consider that a coplanar capacitor is still formed between sensing and pseudoreference electrodes. The total capacitance of the system includes the coplanar capacitance C_{cp}. Combining these expressions with the equations from the EDL theoretical model, a new set of mathematical expressions arises, as noted in Table 3.5.

The system of equations results in the transfer characteristics illustrated in Figure 3.12. The difference between the original ISFGFET model and the pseudoreference model is the inclusion of the coplanar capacitance. For V_{ref}=0 the pseudoreference electrode does not affect the distribution of charged species in the electrolyte and the coplanar capacitance acts as a parasitic capacitance. Thus, the drain current I_D values are lower for the new model compared to the ISFGFET one. On the contrary, by applying even a low voltage on the pseudoreference electrode, there is a significant shift towards higher I_D values and lower threshold voltage V_{TH}.

It is expected that biasing the pseudoreference electrode will induce a measurable change of the sensor's output, but not as drastic as in Figure3.12. The threshold voltage shift ΔV_{TH} predicted by the model is 0.72 V per 1V change of V_{CG}. The expected ΔV_{TH} for such sensors is in the order of mV, as also indicated by the summarising tables in Appendix A. It is possible that the theoretical model by Kaisti et al.[31], on which the simulations are based, is not designed for biasing both control gate and pseudoreference electrode. For future suggestions, physics-based simulations might yield more realistic results.

3.6. Final Remarks

As indicated by the literature study, a common drawback of biosensor-related studies is the lack of focus on the underlying operation mechanisms of FET-based devices. To counter-act this effect, the purpose of this chapter is to introduce the theoretical background behind four areas of interest:

- The operation of the conventional floating gate-based FET sensor
- The effect of the electrical double layer formation on the behaviour of the FGFET sensor
- The implementation of an additional planar electrode as a second control gate to the conventional FGFET sensor
- The integration of a planar pseudoreference electrode on the FGFET sensor

Each theoretical section composes a system of equations to establish mathematical models. An insight on the results of the models follows:

- **FGFET model:** The mathematical and ADS models successfully predict the characteristics of the conventional FGFET in absence of sensing charge Q_S. It is indicated that the effect of the added parasitic capacitances and the interconnect dimensions is negligible.
- **ISFGFET model:** The mathematical and ADS models exhibit distinct behaviours. Measurements in wet conditions will show the effectiveness of the models.
- **Coplanar capacitance model:** Two mathematical models were created, indicating very similar behaviour. By biasing only the coplanar gate the device exhibits transistor characteristics, but with low drain current values. The optimum operation is noted for the dual-gate mode.
- **Pseudoreference model:** A simplified model is proposed for the pseudoreference operation mode, combining elements from the previous models. Drastic threshold voltage shifts are predicted when biasing the pseudoreference electrode.

The first two models aim at clarifying if the effect of the electrical double layer should be included in mathematical models for floating gate-based FETs. Comparison between the established models and experimental measurements will indicate which model captures the sensor's behaviour more accurately. Similarly, two different cases were studied for the implementation of a planar electrode in proximity to the sensing electrodes. Future measurements will show whether it forms a coplanar capacitor or acts as a pseudoreference electrode.

Overall, the created models were validated and are going to be used as the basis for the designing process. In the next chapter, the dimensions of the sensor elements are optimised aiming towards higher sensitivity and maintaining operation in the saturation regime. Here, the C_{CG}/C_{tot} ratio was indicated as a critical design criterion.

4

Design

This chapter describes and thoroughly details the decisions that led to the final design of the BBB-on-chip. The sequence of the current chapter reflects the design flow that was followed during the stages before the fabrication of the final platform. Initially, the conventional structure of the floating-gate based FET is examined. New dimensions are suggested based on the developed models for the next generation sensor. On the next step, the implementation of an additional electrode in the centre of the sensing well is studied to determine an optimal geometry. Said structure was modelled both as an electrode of a coplanar capacitor and a pseudoreference electrode. Finally, ten die designs and their placement on the wafer are presented for the new photolithography masks.

4.1. Dimension Optimisation

At the first step, the dimensions and their effect on the performance of the sensor are studied. By optimising the dimensions of the sensor, higher sensitivity is expected while still operating under the saturation regime. The key elements of this procedure follow:

- The MOSFET dimensions (drain and gate terminal areas, gate oxide thickness) are maintained for both practical and cost-related reasons. Firstly, MOSFETs with these dimensions have been fabricated and tested, and by maintaining the dimensions the risk of non-operating transistors is minimised. Secondly, high-resolution masks are used for the fabrication of the MOSFETs and their replacement would prove rather costly.

- Three parameters are optimised, the dielectric thickness between floating and control gate t_{CF}, the thickness of the first metal layer (Al) t_{Al} and the control-gate area A_{CG}.

- As indicated in the theory chapter, the C_{CF}/C_{tot} ratio regulates the output of the sensor. According to other studies that implement the floating gate configuration, the control-gate capacitance should be 80-90% of the system's total capacitance [23], [16], [147]. C_{CF} controls the state of the floating gate and should be high enough to minimise charge variation between floating and control electrodes.

- The so called parasitic capacitances, do not contribute to the transductive part of the sensor and should be minimised. The previous MOSFET dimensions compose a capacitance between drain terminal area and silicon substrate $C_{GD} \ll C_{tot}$, reinforcing the decision of maintaining them for the new design.

- Similarly to the drain capacitor, the capacitor that is formed between the floating electrode on top of a polyimide (PI) layer and the silicon body is insignificant. As a result, regulating the thickness of the polyimide layer will be of no consequence to the sensor's performance.

- The effect of the interconnects is considered negligible based on the results of the previous chapter and are not examined during the dimension optimisation.

To check the effect of the critical design parameters t_{CF}, t_{Al} and A_{CF} on the sensitivity of the sensor, a sensing charge Q_s between $0.0001and10pC$ is assumed for the models. The selected Q_s values were determined based on the paper by Barbaro et al., where a similar theoretical study was conducted. The design parameters were examined with the ADS tuning tool, aiming at higher sensitivity $\Delta I_D/\Delta Q_s$.

4.1.1. Simulation Results

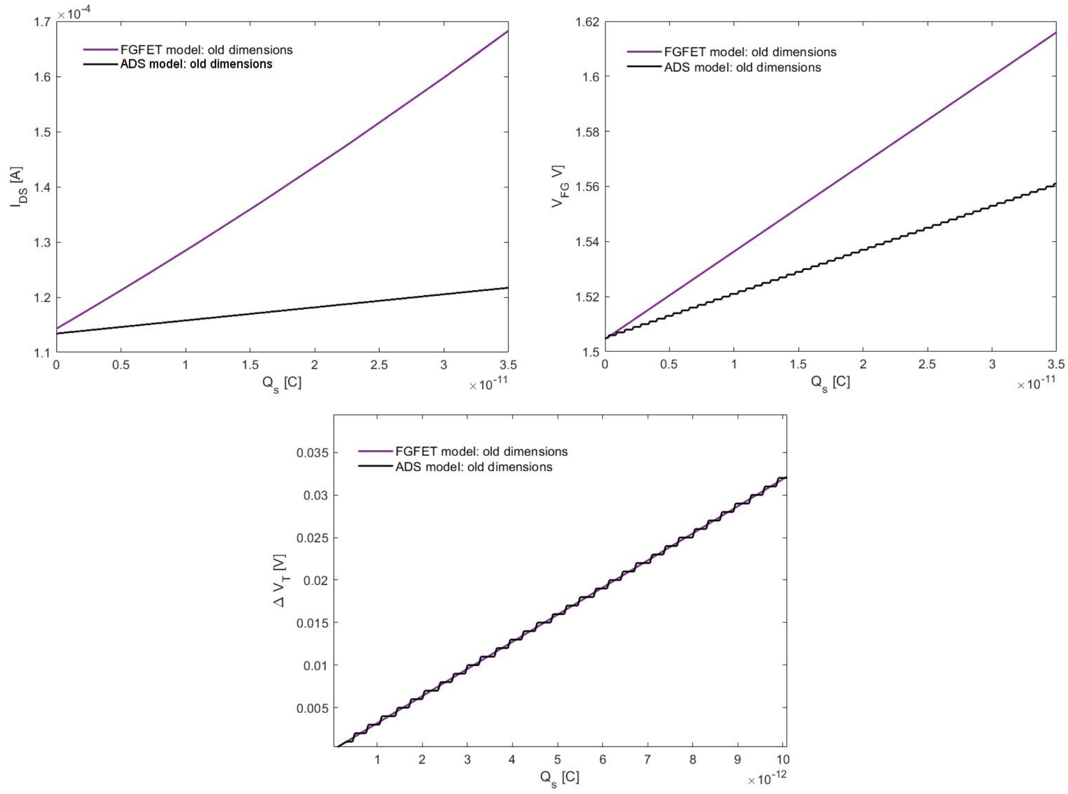

Figure 4.1: ADS simulation results compared to the FGFET mathematical model. The sensor's sensitivity can be studied both as the response of the drain current I_D and floating-gate voltage V_{FG} to the sensing charge Q_s. Both ADS and FGFET model derive the threshold voltage shift V_{TH} from the same equation. The sensor is biased under V_{CG} =2 V and V_{DS} =0.1 V.

Sensitivity as the current response of the sensor to an initial stimuli is experimentally easy to identify, but the threshold voltage shift ΔV_{TH} in relation to the sensor's input is also commonly used (look in Appendix A). It is experimentally challenging to identify the threshold voltage, which is the intercept between the linear extrapolation of the $I_D - V_{gate}$ curve at the maximum slope and the x plot axis. A third method of studying sensitivity is observing the $V_{FG} - Q_s$ slope (see table 4.2).

The ADS simulation predicts slightly different results from the FGFET mathematical model when Q_s is the input, as shown in Fig 4.1. Both drain current I_D and floating-gate voltage V_{FG} resulting from the ADS simulations are compared to the results of the mathematical equations. The plots indicate that the mathematical model predicts both higher I_D and V_{FG} sensitivity. It is possible that the part of the ADS model which introduces the sensing charge to the system does not accurately replicate its effect.

In the $\Delta V_{TH} - Q_s$ plot, the step-like behaviour of the ADS graph is apparent. The values of the threshold voltage shift result from the same equations in both models, explaining why they follow the same trend. It is assumed that the reason for the step-like behaviour is not the step size (in this case $5 \cdot 10^{-14}$ C) of the simulations, but rather the numerical analysis capacity of ADS. Nevertheless, ADS was used for the determination of the optimised dimensions.

Table 4.1: Parameters studied during the optimisation process. The values used in each model are noted.

Parameter	**Old Dimensions**	**Optimised Dimensions**	**Final Design Dimensions**	**Description**
t_{Al}	600 nm	600 nm	1000 nm	Floating gate thickness
t_{CF}	45 nm	170 nm	170 nm	SiO_2 thickness between CG and FG
A_{FG}	490x490 nm^2	400x400 nm^2	490x490 nm^2	Floating-gate area
A_{CG}	490x490 nm^2	400x400 nm^2	400x400 nm^2	Control-gate area

4.1.2. Effect of examined parameters on sensitivity

It is already mentioned that the value of the C_{CF} capacitance is a crucial design criterion for floating-gate based sensors. On one-hand, minimisation of the control-gate capacitance C_{CF} lowers the total capacitance of the system C_{tot}, so that a slight variation of the sensing charge Q_s causes higher alteration of the V_{FG} and ΔV_{TH} values. As a consequence, the I_D/Q_s sensitivity is also higher. On the other hand, a low C_{CF} capacitance in the same order with the parasitic capacitances of the system, will not modulate the behaviour of the floating gate. The effect of the capacitance between floating-gate and silicon body C_{FB}, and between drain terminal and silicon body C_{GD} will no longer be negligible, and the channel might not be formed.

Table 4.2: Sensitivity of the sensor based on the FGFET and the ISFGFET model, resulting from different sensor dimensions.

	$\Delta I_D/\Delta Q_s$		$\Delta V_{FG}/\Delta Q_s$	
	FGFET	**ISFGFET**	**FGFET**	**ISFGFET**
Old Dimensions	1.526 μA/pC	-0.030 μA/pC	3.186 mV/pC	2.805 mV/pC
New Dimensions	4.025 μA/pC	-0.060 μA/pC	10.44 mV/pC	7.490 mV/pC
Final Dimensions	2.225 μA/pC	-0.032 μA/pC	8.386 mV/pC	6.202 mV/pC

Both the dielectric thickness between floating and control gate t_{CF} and the area of the control-gate A_{CG} are parameters that highly affect the performance of the sensor. Both parameters are directly associated with the C_{CF} that regulates the values of floating gate voltage V_{FG} and the threshold voltage shift ΔV_{TH}. So, taking both phenomena into account the final dimensions of the control-gate oxide thickness and area are shown in Table 4.1.

The thickness of the floating-gate t_{Al} is also examined. A thicker floating-gate not only servers fabrication purposes, but also plays a role in the fringe-effect capacitance between control and floating gate. However, this role does not significantly alter the sensitivity of the device. ADS simulations indicated that an increase from 600nm to 6000nm results in 0.001% sensitivity increase.

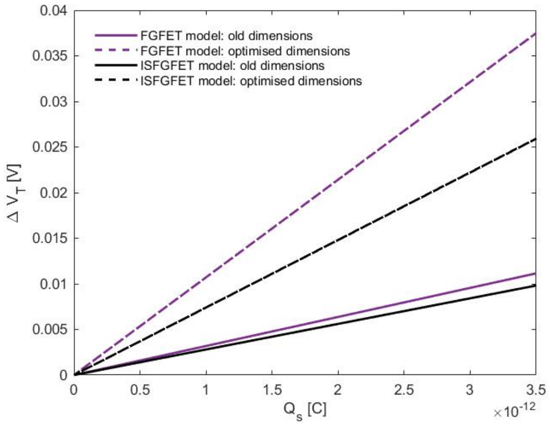

Figure 4.2: Threshold voltage shift ΔV_{TH} in relation to sensing charge Q_s resulting from the FGFET and ISFGFET models. The ISFGFET model, including the effect of the electrical double layer predicts lower performance. Both models indicate higher sensitivity for the optimised dimensions, derived from ADS simulations. The sensor operates under V_{CG} =2 V and V_{DS} =0.1 V.

The optimised dimensions are inserted in the FGFET and ISFGFET mathematical models to study how they predict the effect of the sensing charge. As depicted in Fig 4.2, the model including the effect of the electrical double layer (ISFGFET model) predicts lower performance than the conventional FGFET model. In both cases, the optimised dimensions yield improved performance, as also indicated in Table 4.2, where the slopes of $\Delta I_D/Q_s$ and $\Delta V_{FG}/Q_s$ are noted.

4.1.3. Optimised design limitations

On the next step, the compatibility of the optimised dimensions with the fabrication process of the sensor was cross-checked. A thicker aluminum layer for the floating-gate pad and a thicker SiO_2 layer over the floating-gate can be easily formed during the fabrication process. However, a high-resolution mask was previously used for the patterning of the floating-gate layer with an area of 490x490 nm^2, and such a mask provides better-defined patterns with no need for manual alignment. The purchase of a new high-resolution mask would be rather costly, while a lower resolution mask could lead to alignment issues and rougher patterns. For this reason, the response of the sensor is studied in the case of the control-gate area being smaller than the floating-gate area.

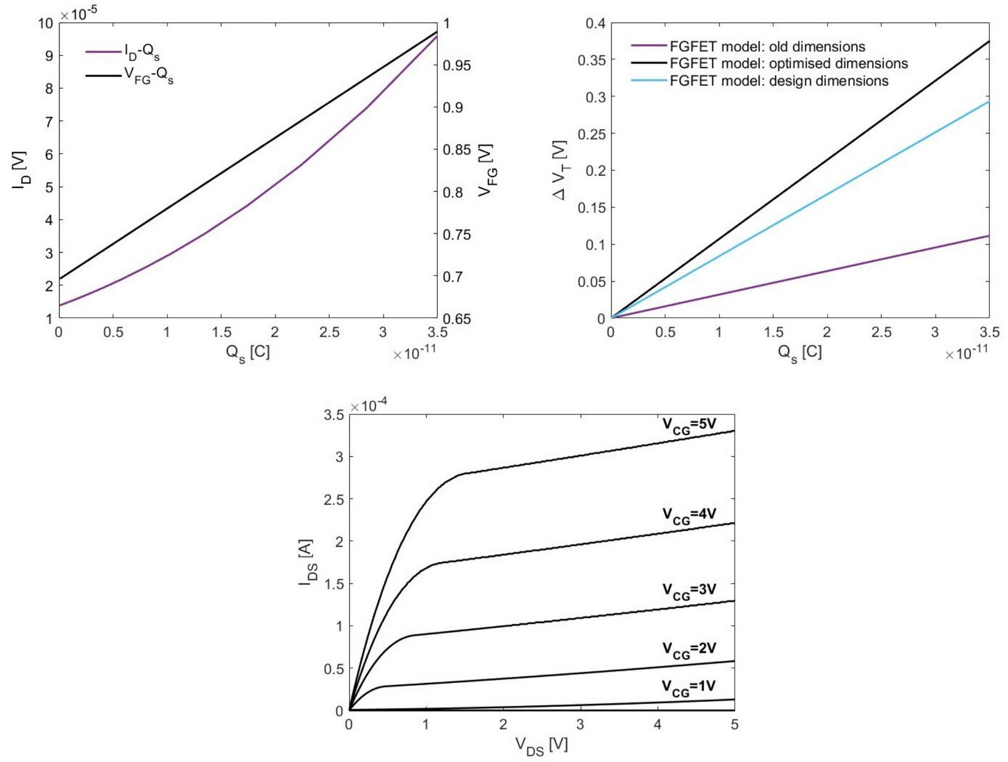

Figure 4.3: The response of the sensor to different values of sensing charge Q_s predicted the FGFET mathematical model. The first graph shows the response of the sensor for the final design dimensions, with the area of the floating-gate being bigger than the control-gate area. The threshold voltage shift ΔV_{TH} is plotted for all studied sensor dimension, demonstrating their effect on the sensor's sensitivity. The sensor is biased under V_{CG} =2 V and V_{DS} =0.1 V. The output characteristics of the sensor with the final design dimensions result from ADS simulations and indicate that the sensor can operate on saturation mode.

A floating gate area of 490x490 nm^2 and a control gate area of 400x400 nm^2 are applied in both the FGFET mathematical model and ADS simulations (as noted in Table 4.1). This translates to a direct-field capacitor with an area of 400x400nm between floating- and control-gate, with an altered fringe-effect capacitance due to the larger surface of the floating gate. An overview of the simulation results are shown in Fig 4.3. The voltage shift graph indicates that a sensor with the final dimensions shows improved performance compared to the initial sensor, but lower than that of the optimised dimensions. It was decided that just altering the dimensions of the control-gate, is an efficient design to achieve improved sensitivity.

The values of the C_{CF}/C_{tot} ratio are noted in Table 4.3, where in all cases the ratio remains higher than 0.3. This value is the limit of considering the effect of parasitic effects negligible. The change of the ratio is drastic between the initial and the optimised dimensions, but not as much in the case of the final dimensions.

Table 4.3: Critical capacitance ratios for the studied dimension cases.

		Old Dimensions	**Optimised Dimensions**	**Final Design Dimensions**
FGFET model	C_{CF}/C_{tot}	0.7523	0.4445	0.3479
ISFGFET model	C_{SG}/C_{tot}	0.9647	0.9892	0.9863

The ISFGFET model is characterised by the ratio between sensing gate capacitance C_{SG} and total capacitance C_{tot}. Even though the sensitivity of an ISFGFET is highly affected by the electrolyte capacitance, the sensing capacitance C_{SG} should be in the same order with C_{tot}, achieving both high sensitivity and control over the output of the sensor [34]. For the ISFGFET simulations a sensing area A_{SG} of 150x150 ^{2} was used.

4.2. Implementation of planar/pseudoreference electrode

The innovation of this project is the implementation of a planar/pseudoreference electrode on the sensing PDMS well during the fabrication of the chip. It is expected that this additional structure will lead to increased sensitivity. The models of the previous chapter were studied in an effort to comprehend the way the additional electrode functions. Figure 4.4 depicts how the electric potential is distributed between two coplanar electrodes immersed in an electrolyte. The capacitance between coplanar electrodes is based on the fringe-field, which results in the non-uniform voltage distribution. The electric-field distribution is depicted in Fig 4.5 by the arrows and the contour plot shows the electric-potential distribution.

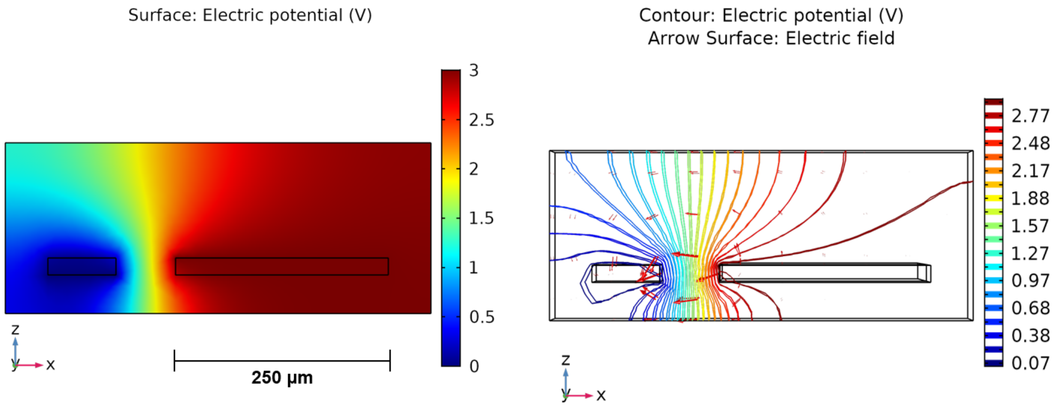

Figure 4.4: Electric potential distribution between two coplanar electrodes. Arrows indicating the distribution of the electric-field between two coplanar electrodes. The contour plot depicts the distribution of the electric- potential.The schematics are extracted from COMSOL.

In an effort to avoid the use of a conventional Ag/AgCl reference electrode, most studies utilize a gold wire dipped in the electrolyte. Other studies, identified during the literature study, implemented planar gold or platinum structures as pseudoreference electrodes. Three possible scenarios were identified as shown in Fig 4.5: planar electrodes resembling flattened wires [117], [148], disk-shaped electrodes [84],[121], [138], [149] or electrodes surrounding the sensing area [55]. The most common is the disk-shaped electrode and according to literature, different dimensions were studied varying from the μm to the mm-range [38].

One pseudoreference electrode can be used to gate several transistors or, like in the third case, one electrode corresponds to one transistor. In the case of the studied BBB-on-chip, extended electrodes connected to eight different transistors are suspended on a PDMS membrane. The suspended electrodes can easily break during the fabrication process, so the implementation of a planar electrode for each extended-gate will be troublesome. Adding to that, fabricating multiple disk-shaped electrodes can hinder the transparency of the sensing well, an essential factor for an OoC platform. Consequently, it was decided that one disk-shaped pseudoreference electrode will be utilised in the centre of the well, modulating the behaviour of all eight sensing pads.

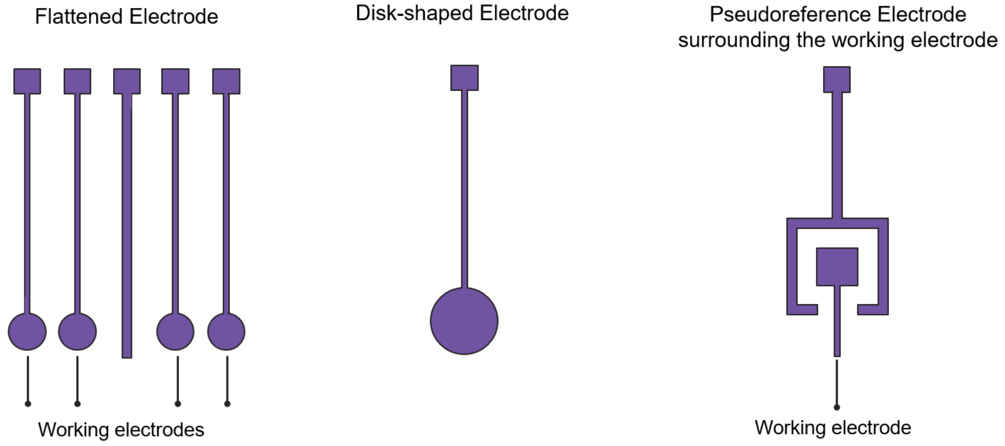

Figure 4.5: Schematic representing the three different types of pseudoreference electrode structures identified though the literature study.

The general principle is that the reference electrode is placed in close proximity with the working electrode, but the determination of the position gets more complicated when more electrodes are at play. According to the book on reference electrodes by Inzelt et al., when there are two working electrodes, the reference electrode should be placed further away in an area with a uniform electric-field. For the final design, the size of the disk-shaped electrode, the distance between sensing-gates and the position of the planar/pseudoreference electrode are determined based on simulations shown in the following section.

4.2.1. Determination of planar/pseudoreference dimensions

The characteristics of the planar electrode are determined based on the following factors:

- To consider the formation of the coplanar capacitor of Section 3.4, the electrode's finite width should be negligible in comparison with its length and the width should be higher than the half separation, $w/a \gg 1$.
- The radius of the PDMS well based on the previous design is 3mm meaning that the sensing electrodes can extend in the mm range.
- The coplanar capacitance C_{cp} is in proportion to the natural logarithm of the w/a ratio, which attenuates the effect of the ratio to the capacitive signal.
- A disk-shaped planar electrode is chosen to create a concentric electric-field, accommodating thus the same interaction between the central electrode and the sensing gates. For the models it is considered that a coplanar capacitor is formed between sensing and central electrode with a width equal to that of the sensing gate w_s.

The final dimensions of the planar electrode are determined based on the models of the previous chapter. The results of the pseudoreference model are presented in Fig 4.6, being the model that includes the sensing area A_s term in the system of equations. The effects of sensing electrode width w_s, length l_s and half-separation from the pseudoreference electrode a are illustrated. It is indicated that w_s has the most significant effect on sensitivity, with higher width leading to lower slopes. It was

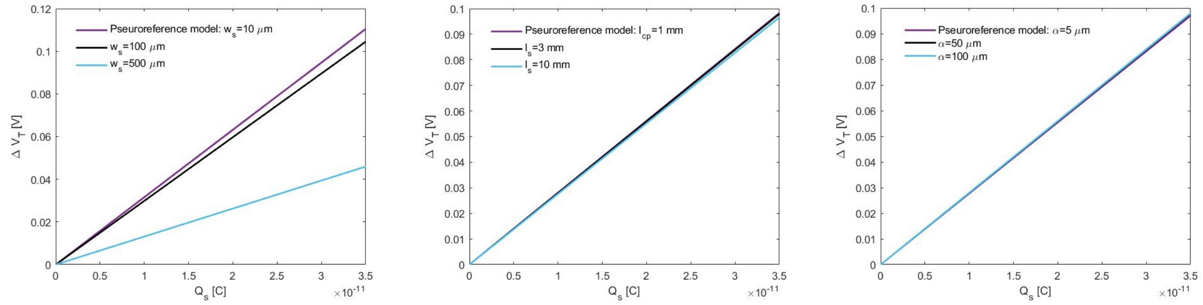

Figure 4.6: Effect of the sensing electrode width w_s, length l_s and distance a to the threshold voltage shift ΔV_{TH}, based on the pseudoreference mathematical model. The applied potentials are V_{DS}=0.1V, V_{CG}=2V and V_{pseudo}=2V.

expected that ΔV_{TH} would be optimal in a range of w_s values, where the sensing area would achieve a balance between high surface charge and avoiding high electrolyte capacitances.

The effect of the electrode length l_s and the half-separation a do not significantly effect sensitivity (see Fig 4.6). Longer electrodes contribute to a higher C_{tot} and lead to slightly lower sensitivity, while the effect of a is the opposite compared to the electrode width w_s. The coplanar capacitance C_{cp} is analogous to the logarithm of the w_s/a ratio, but only w_s is inserted to the equations describing the EDL effect. Thus, parameter a is less significant than the electrode width w_s. Still, the pseudoreference model is based on the limitation $w_s \gg a$. Studying the behaviour of the sensor outside the range of this limitation is an interesting design idea.

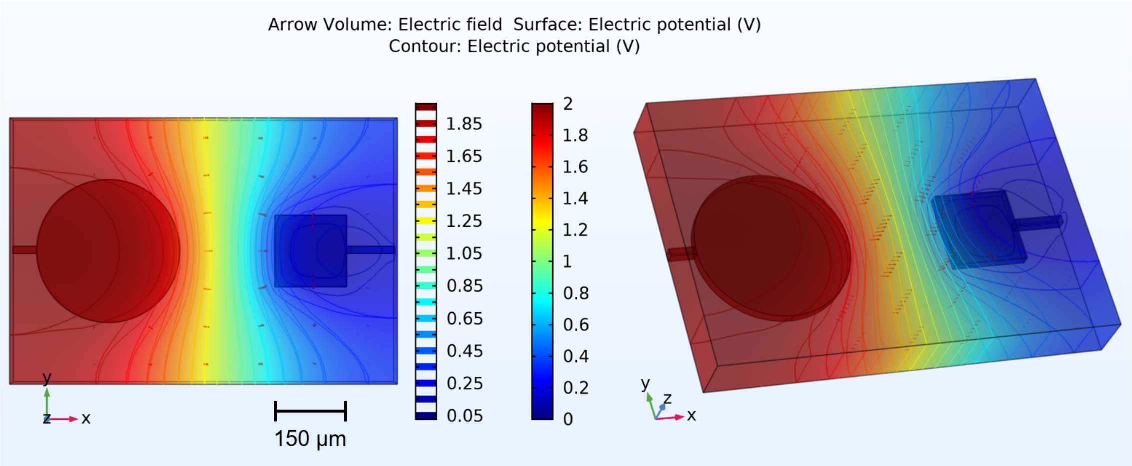

Figure 4.7: Electric potential distribution and electric-field direction between the planar pseudoreference electrode and sensing electrodes in close proximity, as extracted from COMSOL. The electric potential contour shows the effect of one pseudoreference electrode to all the surrounding electrodes.

4.2.2. Overview of optimised dimensions

In order to both validate the predictions of the models and aim towards higher sensitivity the following dimensions were chosen for the new sensor.

- **Sensing area:** Two types of sensing pads are implemented with areas of 80x80 μm^2 and 150x150 μm^2 for comparison purposes. These dimensions do not inhibit the visibility in the PDMS well.
- **Extended electrode length:** Long electrodes of 2.6 mm place the sensing pads in close proximity to the central electrode, as illustrated in Fig 4.7, assuming the formation of a coplanar capacitor. In the second case, shorter electrodes with 2 mm length are chosen to study the interaction between the central electrode and the sensing pads, when the equation for C_{cp} is not valid.

- **Planar electrode area:** A disk-shaped electrode with a diameter of 300μm, based on literature, will be implemented in the center of the well. It is expected that one electrode in the centre of the well can affect the binding phenomena on all the surrounding sensing pads, as indicated by the COMSOL schematic in Fig 4.7.

An overview of the results of the theoretical models for a pseudoreference electrode with a diameter of 300μm and sensing electrodes with length 2.6mm, width 150μm and separation a=80μm is presented in Fig 4.8. The $\Delta I_{DS}/Q_s$ slopes predicted by the coplanar models (approximately 1.7 μA/pC) are lower than the FGFET model slope (at 3.7 μA/pC), where no coplanar electrode is implemented. Even for bias V_{cp} higher than 2V the slopes do not reach the level of the original structure, which means that according to the models that ignore the effect of the EDL, the coplanar capacitance plays a parasitic role rather than significantly affecting the V_{FG} value in combination with C_{CF}. In the case of the model implementing the EDL role, depicted with the purple line, the I_{DS} values are in the order of 26 mA showing a sensitivity of 4.7 μA/pC. This model is based on the equations by Kaisti et al. and has been applied to describe the behavior of sensors when a Ag/AgCl reference electrode, an Au or an Pt wire is dipped in the measurement medium. Thus, the model gives a promising indication for optimised sensor performance with the addition of the planar electrode.

The results of all the models are compared on the top right of Fig 4.8. In terms of ΔV_{TH} sensitivity, the conventional FGFET model without the planar electrode exhibits the highest slope and the pseudoreference model the lowest one. Finally, for the dimensions mentioned above, and for a bias V_{cp}=2V, the output characteristics of the sensor are shown at the bottom left graph, as extracted by the ADS simulation. While the sensor is double-biased, it still operates as a MOSFET and reaches saturation.

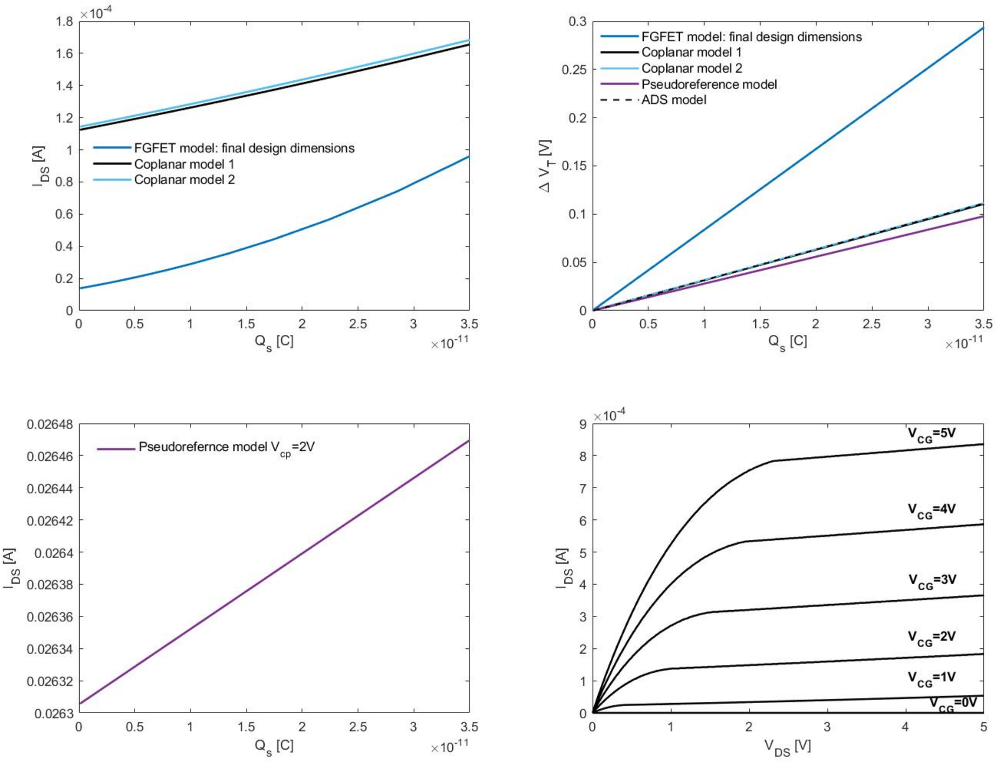

Figure 4.8: Overview of results from simulation models for the implementation of a pseudoreference electrode interacting with a sensing gate of width 150μm at a distance of 80μm. On the left, the effect of the sensing charge Q_s on the drain current I_{DS} is studied for different cases. On the top right, the threshold voltage shift ΔV_{TH} is investigated and on the bottom right the output characteristics of the sensor operating on double bias V_{CG} and V_{cp}=2V are plotted, as extracted by ADS.

4.3. Final mask design

For the next generation sensor, three new masks were designed using L-EDIT (Layout Editor) by Tanner. The design of the OoC remains the same up to the step of the first metallic layer, maintaining the dimensions of the eight transistors and their floating gates.. As a result, the three new masks involve the patterning of the control-gate structure, the extended-sensing electrodes and the coplanar electrode in the centre of the sensing well. The main mask corresponds to the second metallic layer (for titanium structures) and includes all the above-mentioned structures. Based on the second metallic mask, two more masks are designed for the polyimide (PI) layers that are going to encapsulate the extended-sensing electrodes. The ideas behind designing the new masks are explained step by step.

Each 100mm wafer consists of 52 dies, as seen in Fig 4.9, offering the opportunity of having many different designs on one wafer. During the dimensions optimisation step, it was hypothesised that a control-gate of smaller dimensions than in the original sensor, yields higher sensitivity. To experimentally study this hypothesis, the top 26 dies of the wafer are designed with the old control-gate of 490x490 μm^2 and the bottom 26 with a 400x400 mum^2 control-gate area, as illustrated in Fig 4.9.

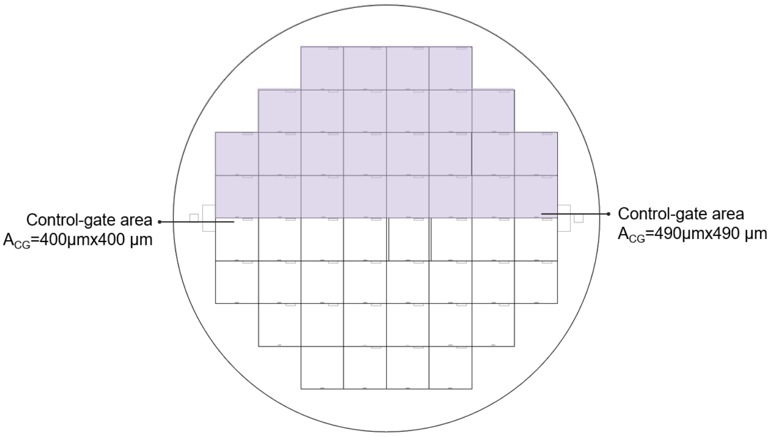

Figure 4.9: Schematic of 100 mm wafer including 52 dies. The coloured part corresponds to the dies with the old control-gate dimensions of 490x490 μm.

Next the length of the sensing-electrode extensions is arranged. Extensions with a length of 2.6 mm were chosen for the right part of the wafer and on the left, the length of the extensions is 2mm. The comparison between the effects of the two different electrode lengths is possible in one-chip, in the so-called mixed design, as seen in Fig 4.10.

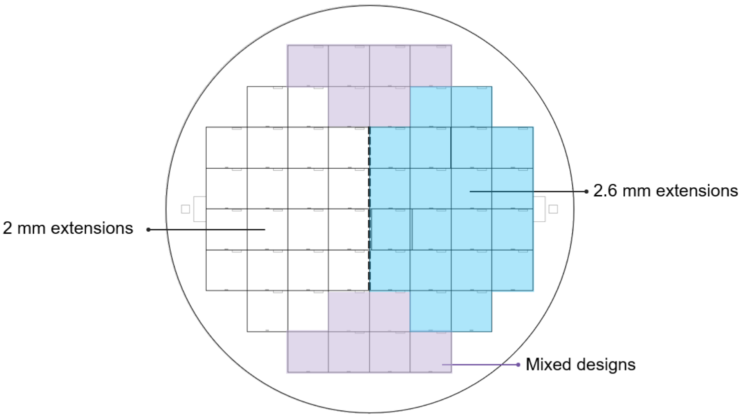

Figure 4.10: Schematic of 100 mm wafer including dies with the longer 2.6mm electrodes (light blue) and the mixed design (purple). The mixed design contains both 2mm and 2.6mm long sensing electrodes.

Finally, the effect of the sensing pad area will be studied by implementing two different pads. As illustrated in Fig 4.11, the sensing pad area for some dies is 80x80 μm^2, while for others is 150x150 μm^2. This distribution of sensing pads is based on achieving all possible design combinations. In the mixed design, sensing pads of both sizes are included. In the end, there are 10 different types of dies based on combinations of all the parameters that were discussed, named as indicated in Table 4.4.

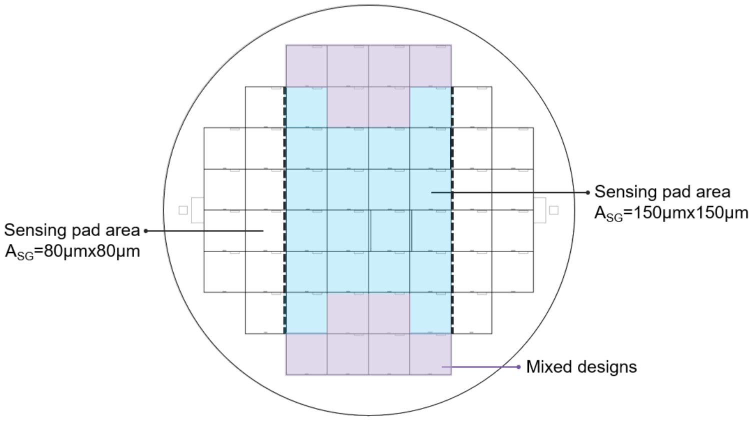

Figure 4.11: Schematic of 100 mm wafer where the light blue part corresponds to the dies with sensing pads of width 150μm, the white to pads of width 80μm, and the purple to the mixed design combining both types of sensing pads.

Furthermore, the width of the electrode extensions that are going to lay on the PDMS layer was altered from 5 to 15 μm to prevent damage or breaking of the electrodes during the fabrication. It was indicated by ADS simulations that even with a width of 15μm the resistance of the electrodes does not significantly affect the sensor's performance. As already mentioned, the sensitivity of the sensor can also be identified as the shift of the floating-gate voltage V_{FG} in response to the sensor's input. Towards this end, electrode connections were implemented between the floating-gates and connection pads at the periphery of the die. The new connection pads have double the area of the pads regulated by the first metallic layer mask to assist wire-bonding. The new planar electrode is connected to a wider connection pad as well.

After taking all of the above into account, the final designs for the second metallic layer mask are shown in Fig 4.12. Based on the length and area of the sensing electrodes, each metallic-mask die design is accompanied by a compatible polyimide design. The purpose of the PI masks is to encapsulate the metallic extensions, protecting them from the measurement medium, while keeping an opening to the metal layer, where the sensing takes place. The alignment between the designs of the metal and PI layers is of high importance to achieve both complete encapsulation of the electrodes and good definition of the sensing areas.

Table 4.4: The designs of the second metallic layer mask, accompanied by the number of dies with each design.

Name:	Control-gate type **O**ld/**N**ew	Extension Length	Sensing-gate area
name	nr of dies	name	nr of dies
Old Mixed	6	New mixed	6
O 2.6mm 80μm	5	**N** 2.6mm 80μm	5
O 2.6mm 150μm	5	**N** 2.6mm 150μm	5
O 2mm 150μm	5	**N** 2mm 150μm	5
O 2mm 80μm	5	**N** 2mm 80μm	5

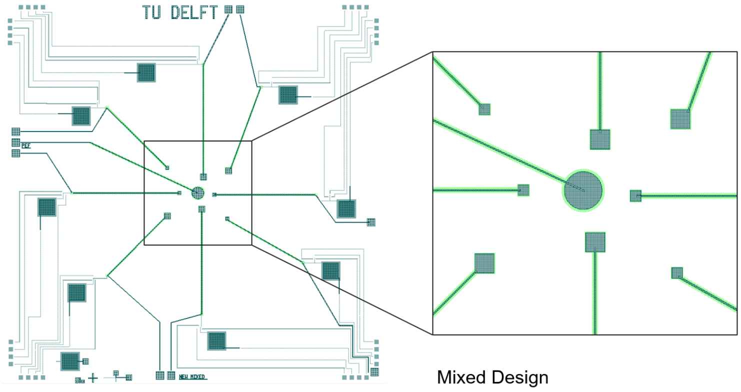

Mixed Design

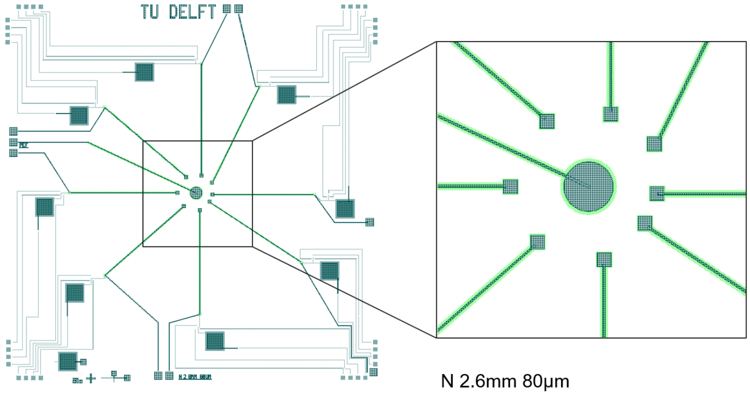

N 2.6mm 80µm

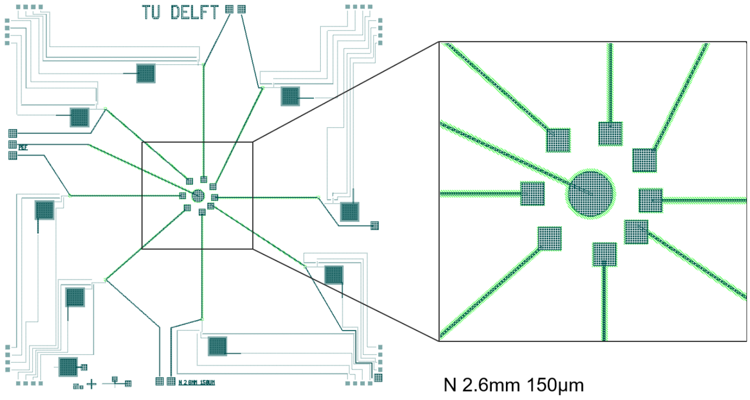

N 2.6mm 150µm

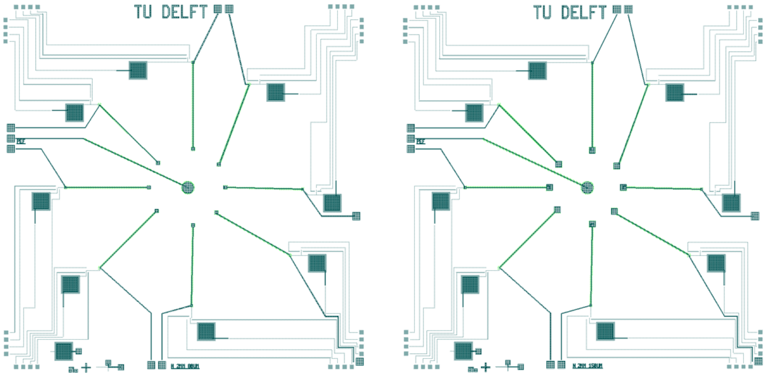

N 2mm 80µm

N 2mm 150µm

Figure 4.12: First metal-layer mask designs in L-EDIT (dark green) accompanied by the first polyimide layer design (light green). The five designs with the new control-gates are shown.

4.4. Final Remarks

The next generation of sensors combine an additional planar electrode with the conventional operation of a floating-gate based FET. Initially, the dimensions of the FGFET structure without the additional electrode were studied and new dimensions were chosen for the control gate electrode and the dielectric between floating and control gate. Half of the dies of the new masks have the new control gate dimensions, so that the dimension effect can be experimentally studied. During the dimension study it was indicated that:

- The ADS model predicts lower sensor response compared to the FGFET model. Nevertheless, it was used for the determination of the final dimensions.
- The mathematical model including the effect of the electrical double layer predict lower threshold voltage shift in response to the sensing charge compared to the FGFET model.
- Parameters that are directly associated with the control gate capacitance C_{CF} drastically affect the sensor's behaviour.
- The final dimension sensor exhibits transistor characteristics and enters saturation mode while showing improved sensitivity.

Concerning the planar electrode integration, there is a leading question in mind, whether the additional electrode acts as a pseudoreference electrode or promotes the formation of a coplanar capacitor. By varying the length of the extended electrodes, the effect of the planar electrode to the sensing gates will be studied. It is assumed that when in proximity a coplanar capacitor is formed, while for bigger distance the planar electrode acts more like a pseudoreference electrode. The results of the planar electrode dimension investigation showed that:

- Higher ΔV_{TH} sensitivity is predicted for smaller sensing areas, a behaviour to be cross-checked with experimental measurements.
- The predicted effect of the sensing electrode length and the half-separation from the planar electrode is very low, according to the defined coplanar capacitance.
- The coplanar mathematical models fit to the ADS predicted ΔV_{TH} sensitivity, with the pseudoreference model exhibiting lower results. On the contrary, the pseudoreference model predicts higher drain current slope compared to the previous models.
- A FGFET sensor with an integrated planar electrode of the defined dimensions shows transistor behaviour on dual-gate operation mode.

Overall, the results of the dimension investigation led to the design of 10 different types of dies as described in Section 4.3.

5

Fabrication

In this chapter the fabrication process of the second generation OoC is presented and discussed. The fabrication took place at the Else Kooi Lab (EKL) cleanroom facilities of the Electrical Engineering, Mathematics and Computer Science (EEMCS) Department, at TU Delft. Initially, the process flow is introduced step-by-step, accompanied by cross-sectional schematics of the wafer and depictions of the resulting structures. Fabrication process impediments that hindered the final devices are then presented in visual form and further discussed. The chapter ends with a visual overview of the fabricated chips, including defects that might render them impractical for further study.

5.1. Process Flow

The fabrication of the second-generation electrochemical OoC follows a designated flowchart, based on a standard BiCMOS process. On the grounds of saving time, four wafers were prepared up to the step of gate oxide deposition, before the start the actual fabrication process. A brief description of the preceding steps follows.

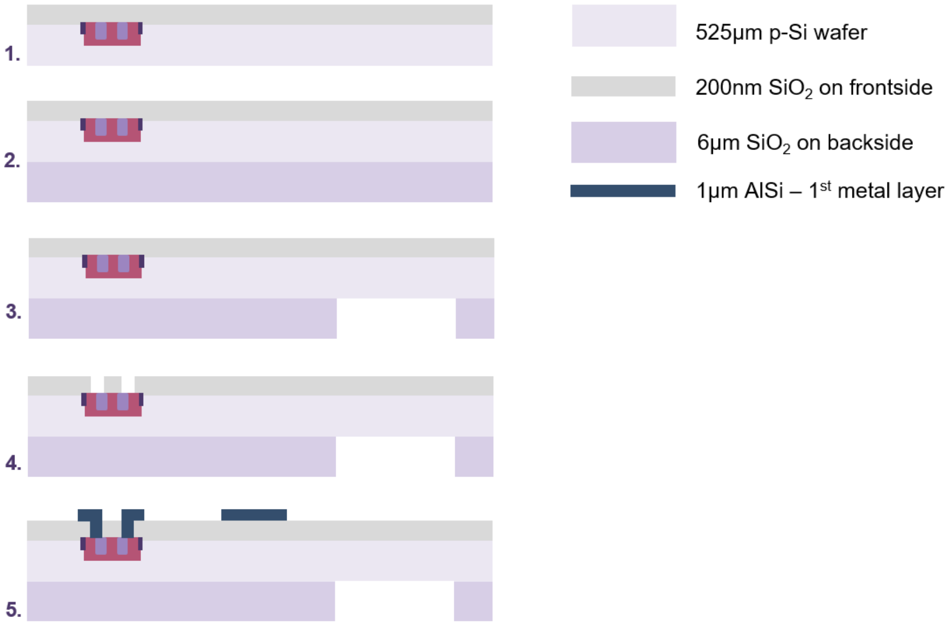

Figure 5.1: Cross-sectional schematics representing the fabrication steps from the gate oxide definition (step 1) to the patterning of the first metal layer (step 5). The layer materials are indicated on the side.

Four 100 mm, 525 μm thick, double-sided polished p-type silicon wafers were used for the fabrication of both n-type and p-type transistors. The zero-layer was patterned on the frontside of the wafers for alignment purposes. On the following steps, the n-well and the source and drain terminals were defined by ion implantation. Finally, thermally grown silicon dioxide of 200 μm was deposited as the gate oxide. A cross-sectional illustration of the structure is shown in step 1 of Fig 5.1.

The proceeding fabrication steps are accompanied by the schematics of Fig 5.2, for illustrative purposes. A layer of 6 μm thick PECVD silicon dioxide layer was deposited on the backside of the wafers (step 2), patterned to form an etching hard mask (step 3). The periphery of the backside hard mask is shown in Fig 5.3.(a). PECVD oxide was chosen over thermally grown oxide for the hard mask, aiming at fast deposition of poorer quality oxide that will be etched during the final fabrication steps for the formation of the sensing well. On the following step, contacts were opened on the frontside by wet etching in BHF, landing on the drain, source and gate terminals (step 4). Contact openings accommodate the connection between the mentioned terminals and the first metal layer .

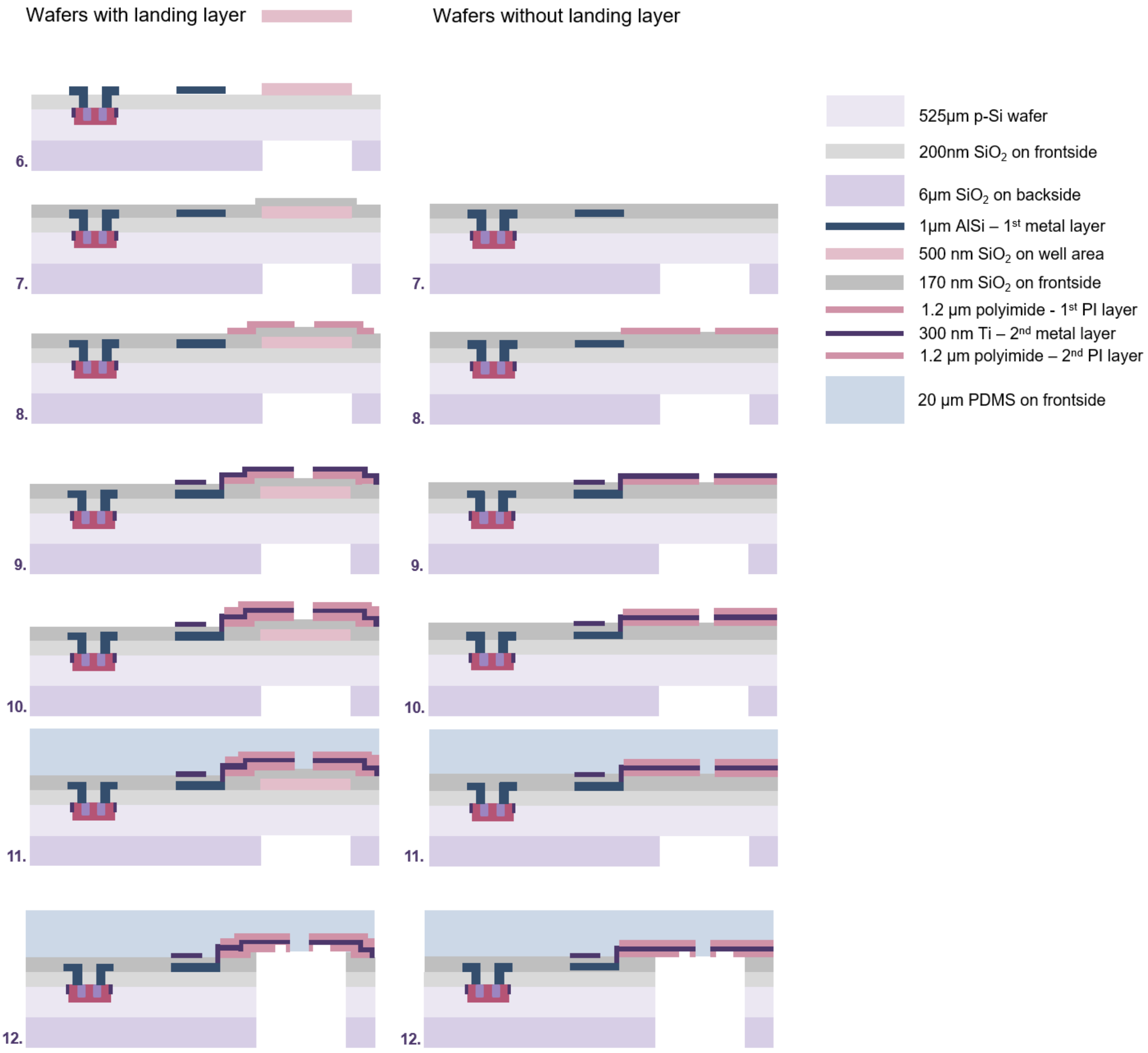

Figure 5.2: Cross-sectional illustrations representing the fabrications steps for the process wafers. Two strategies were followed, thus the two structure columns. A landing layer of oxide is deposited on two of the process wafers (step 6), while the fabrication continues without this step for the remaining wafers. The details of the patterned layers are noted on the side.

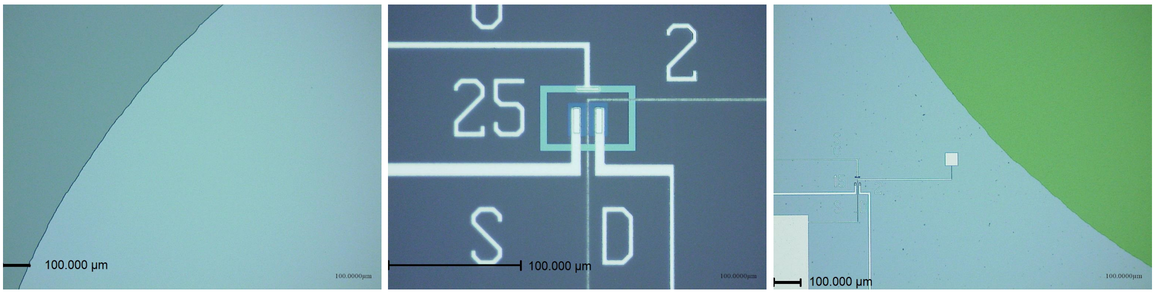

(a) Backside hard mask (b) Al transistor structures (c) Frontside landing layer

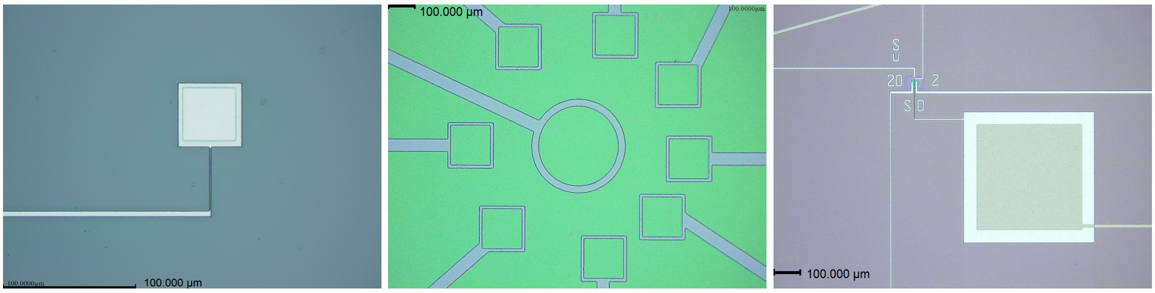

(d) Frontside via opening (e) 1^{st} polyimide layer on well area (f) Ti control-gate over floating-gate

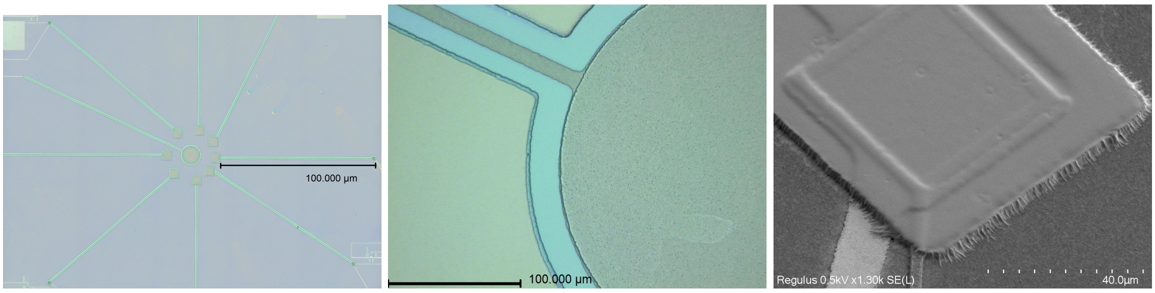

(g) PI sandwiched Ti electrodes (h) PI layers on central Ti electrode (i) Pi sandwiched Ti pad

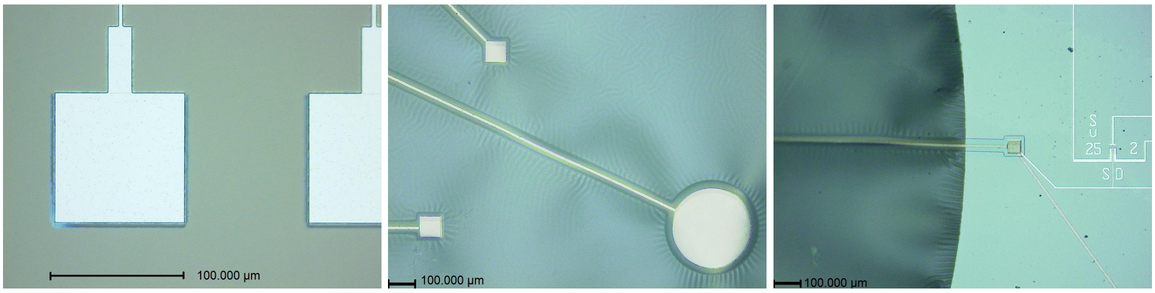

(j) Bond pad openings (k) Electrodes suspended on PDMS (l) PDMS sensing well

Figure 5.3: Optical microscopy and SEM pictures captured during the fabrication process.

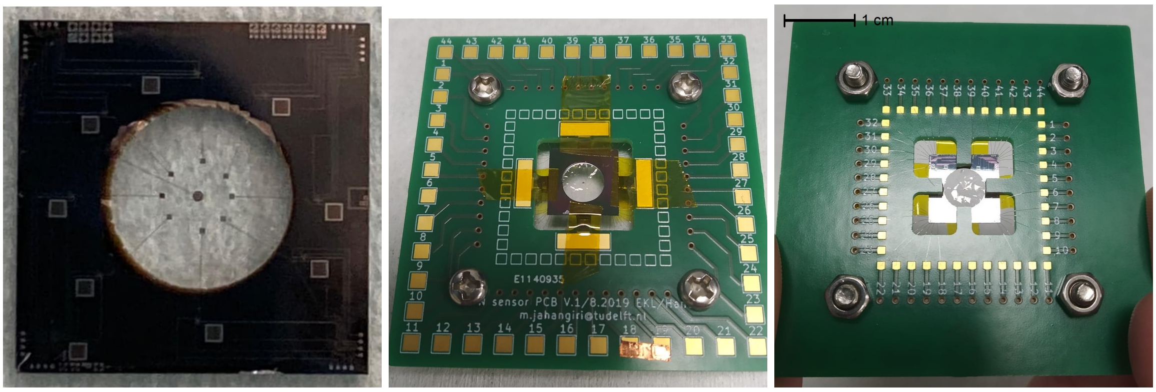

(a) OoC Frontside (b) PCB frontside (c) PCB backside

Figure 5.4: The organ-on-chip platform after wafer dicing has a width of 1 cm. The backside of the chip facing upwards when connected to the custom-designed PCB and the frontside of the OoC where the bond pads are wire-bonded with the PCB pads.

The first metal layer was formed by sputtering 1000 nm of Al/Si (step 5). The high-resolution mask for patterning the floating-gate pad and interconnects includes thin structures, such as electrodes with a width of 5 μm, as it was designed for plasma etching. The corresponding equipment was not available and the structures were patterned by wet etching in PES. The side-effects of this alternative fabrication strategy are further discussed in the next section. In Fig 5.3.(b), the resulting transistor terminals after Al wet etching are shown.

A 500 nm PECVD silicon dioxide layer was deposited on the frontside of two wafers for the formation of a landing layer (step 6). It was hypothesized that a landing layer in the area of the sensing well will hinder damage to the suspended sensing electrodes during fabrication. This soft landing layer was patterned by plasma etching and the resulting structure (green) is seen in Fig 5.3.(c). The following steps are common for all wafers. A 170 nm thick PECVD oxide layer is deposited on the frontside for the definition of the dielectric between floating- and control-gate electrodes (step 7). Next, vias are opened on the frontside by plasma-etching, removing the oxide and landing on the Al layer, as seen in Fig 5.3.(d). Wet-etching was avoided to protect the Al layer, as BHF also etches aluminum with a slower etching rate.

Before the second metal layer, an approximately 1.2 μm thick polyimide layer (by FUJIFILM) was deposited by spin coating and patterned by manual developing where the titanium electrodes would be formed (step 8)(see Fig 5.3).(e). A 300 nm thick titanium layer was then sputtered at 25^{o}C (step9). The control-gate pads, extended sensing electrodes and the planar/pseudoreference electrode were formed by plasma etching, to avoid isotropic wet etching shortcomings similar to the Al patterns. Ti was chosen instead of Al for the sensing electrodes as a more biocompatible material which is less susceptible to oxidisation. Noble metals would also serve as sensing electrodes, but are avoided as they limit cleanroom equipment compatibility (red metals). A second polyimide layer of the same thickness is deposited and patterned on top of the Ti structures (step 10), so that the two PI layers ”sandwich” the metallic electrodes. This scheme, as seen in Fig 5.3.(g),(h) and (i), provides electrical insulation and mechanical robustness for the metallic electrodes, while leaving the sensing pads in contact with the environment.

Contacts were opened on the bonding pads, removing the silicon dioxide layer and landing on the Al layer (see Fig 5.3.(j)). Due to unavailability of the equipment for plasma etching, the contacts were opened by wet etching in BHF without damaging the PI layers. A low-power plasma treatment followed to enhance the adhesion of the PDMS membrane. Polydimethylsiloxane (PDMS) was prepared by mixing with its curing agent (10:1 ratio), degassed and spin coated on the frontside of the wafers (step 11). After the treatment, a 20 μm PDMS layer is formed, where the extended electrodes will be suspended constituting the transparent sensing area of the OoC (see Fig 5.3(k) and (l)).

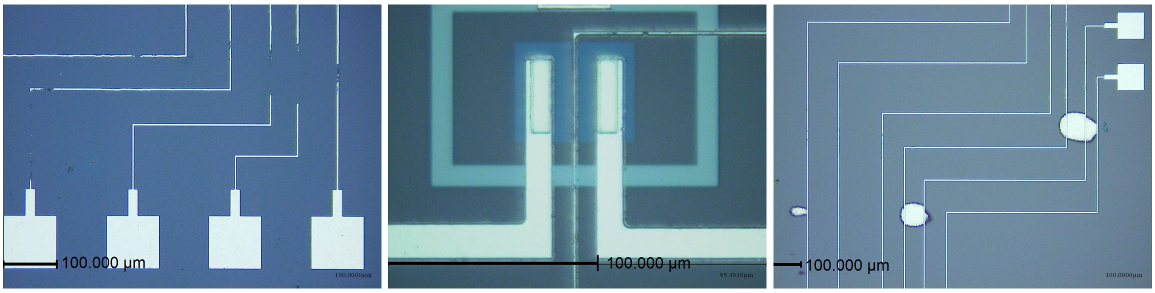

Figure 5.5: Disrupted connections due to overetching, overetched gate structure and micro-masking effect on interconnects after the first attempt of Al wet etching.

The PDMS layer was then covered by 200 nm of sputtered AlSi, thus forming a protective layer. This AlSi hard mask protects the PDMS membrane during the deep reactive ion etching (DRIE) of the Si substrate. After the removal of Si from the backside by DRIE and landing on the oxide layer, the residual oxide and the AlSi hard mask are removed by wet etching in BHF and PES, correspondingly. By the end of the process the PDMS membrane with the suspended electrodes is released, forming the sensing well as a part of the chip (step 12). Finally, each wafer was diced into 52 equal, square chips with an area of 1 cm^2. A chip is shown in Fig 5.4. For measurements, the chips are connected to custom-designed PCBs and the chip bond pads are connected to the PCB corresponding pads by wire-bonding (see Fig 5.4).

5.2. First metal layer wet etching (Al)

As already mentioned, due to equipment unavailability, the patterning of the first metal layer, after the AlSi sputtering, was realized by wet etching in PES. Each wafer was etched individually and visually inspected. During the first round of wet etching, at approximately 8 minutes to remove 1 μm of Al, overetching and micromasking was noticed at some areas of the wafers, as shown in Fig 5.5. It was decided that the AlSi layer should be completely removed by wet etching and the process repeated. After Al removal some superficial cracks were visible on the frontside of the wafers, probably resulting from the stresses due to the last sputtering process.

For the second attempt of Al wet etching, the non-uniform material removal is taken into account. Each wafer is placed with a different orientation on the wafer holder to avoid overetching of the same dies for all wafers. Al etching for 6.5 to 7 minutes followed by 10 sec of poly-Si etch to remove Si residues of the AlSi sputtering took place. Even though the wet etching procedure was carefully monitored, overetching was still noticed (Fig 5.6). One wafer was baked for 30 min at 100 ^{o}C to examine whether baking hardens the photoresist enough to maintain the thin metal structures. The baking step did not seem to have an effect on overetching, but led to increased micromasking, as indicated in Fig 5.6. Unfortunately,preliminary transistor characterization measurements after the step of bond pad openings indicated that the transistors were non-responsive, as further discussed in the following chapter. A back-up wafer was fabricated when Al plasma etching was available, producing the final dies presented in section 5.4 and depicted in Fig 5.4.

5.3. Landing layer and vias opening plasma-etching

Before the definition of the dielectric between floating and control-pads, a landing layer was formed on the area of the sensing well for two of the process wafers. The oxide forming the layer was etched by plasma-etching using the Drytek Triode 384T. It was already noticed that the equipment showed operational instabilities, including very low etching rate (up to 17 min for etching 6 μm of SiO_2) and system errors. Each wafer was etched individually, after determining the etching rate by using a dummy wafer, but the equipment instabilities rendered multiple etching cycles necessary. After the second etching cycle, non-uniform etching was noticed for the dies at the periphery of one wafer, resulting in the colour gradients seen in Fig 5.7 even after photoresist removal.

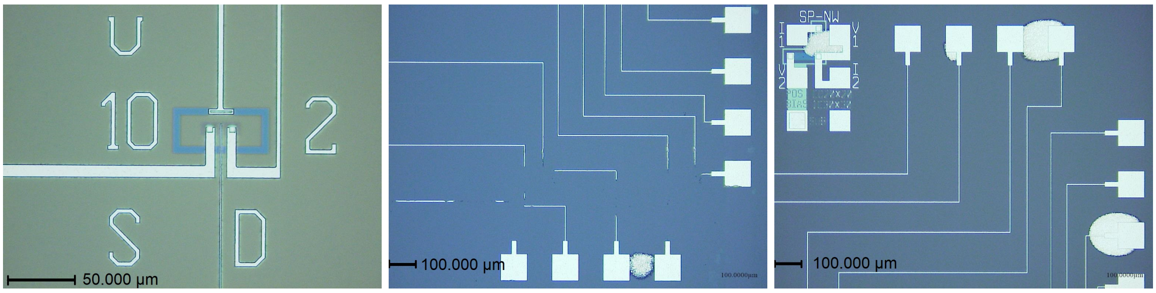

Figure 5.6: On the left, overetched gate structure after second attempt of Al wet etching. The other two pictures show overetched interconnects and micro-masking effect on the baked-wafer after Al wet etching.

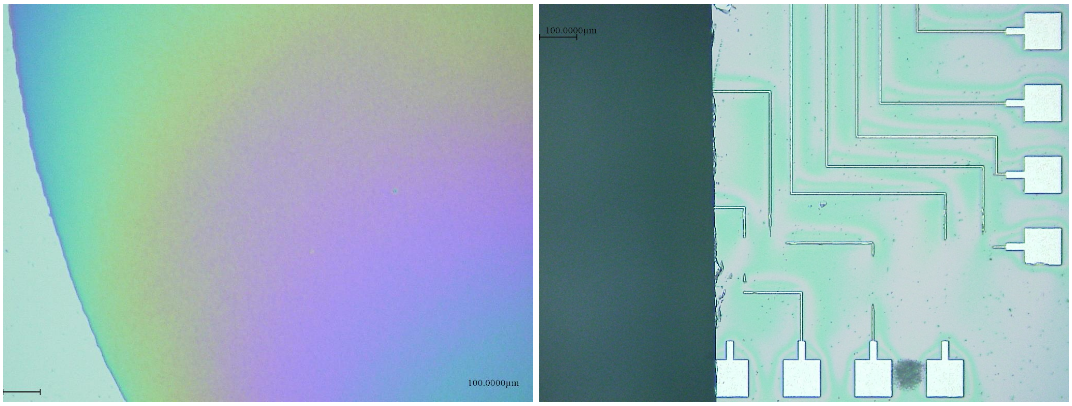

Figure 5.7: On the left, non-uniform landing layer after plasma etching and photoresist removal. On the right, picture of the broken wafer showing the direction of the fracture, still coated with photoresist.

The next fabrication step, for the vias openings, necessitated the use of the Drytek Triode as well. Similar operation issues were noted and in the case of the non-uniformly etched wafer the process was stopped numerous times because of system errors. This wafer broke in half during visual inspection at the direction shown in Fig 5.7. The broken wafer was identified as the baked-wafer of the Al wet etching process, which can be easily deducted by comparing the picture of the broken wafer with the picture in the middle of Fig 5.6. Nevertheless, the baking step is not considered to have caused the breaking. It is more plausible that accumulated stresses due to the continuous plasma etching repetitions were the culprit.

5.4. Overview of fabricated chips

By the end of the fabrication process, 6 dies from the back-up wafer were prepared, which are presented and commented on in this section. The implementation of wider extended electrodes on the PDMS membrane and the careful monitoring during the several cycles of DRIE silicon removal seemed to be effective strategies towards avoiding electrode breaking. However, due to the dysfunction of the initial 4 wafers, the effect of the landing layer on protecting the suspended electrodes was not studied. Visual inspection of the fabricated chips indicated no overetching on the transistor areas, and a more detailed overview follows.

Two dies, namely die 6 and 9 have the same extended electrode design with a length of 2 mm and 80μm wide sensing pads, as indicated by the overview pictures in Fig 5.8. Some holes at the top of the sensing well and a PDMS fracture are noted for die 6, better captured in Fig 5.8.(b). The difference between the two dies lays on the dimensions of the control-gate, as die 9 implements the new gate dimensions. The overview picture of the die renders it a good candidate for measurements. Die 36 carries the design of longer electrodes and wider sensing pads, but shows a PDMS discontinuation on the top right part of the well that might affect measurements in wet conditions (see Fig 5.8.(d),(e)).

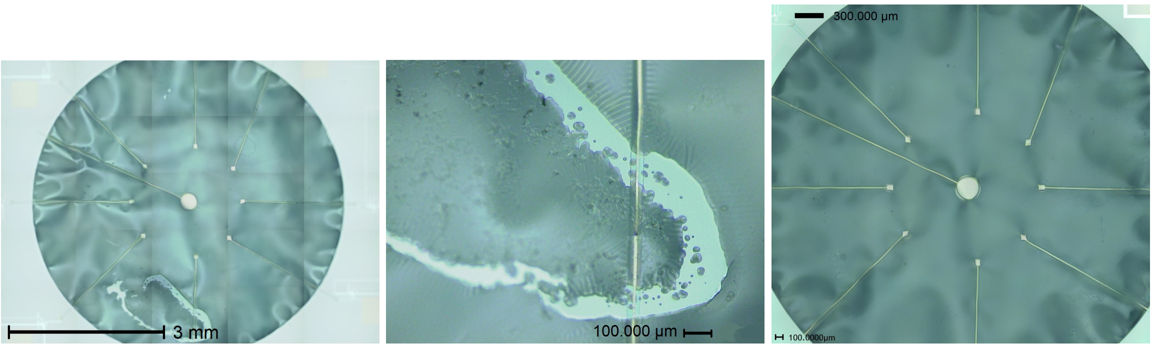

(a) Die 6: **O** 2mm 80μm overview (b) Die 6: PDMS fracture, PI intact (c) Die 9: **N** 2mm 80μm overview

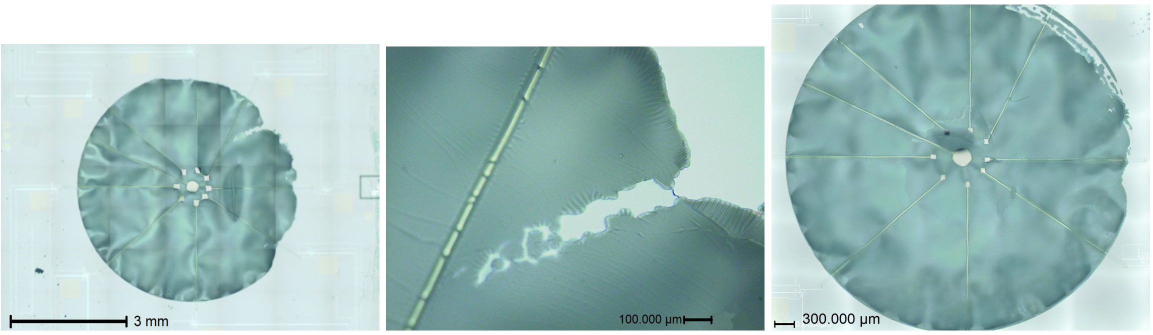

(d) Die 36: **O** 2.6mm 150μm overview (e) Die 36: PDMS fracture, top right well (f) Die 43: **O** 2.6mm 80μm overview

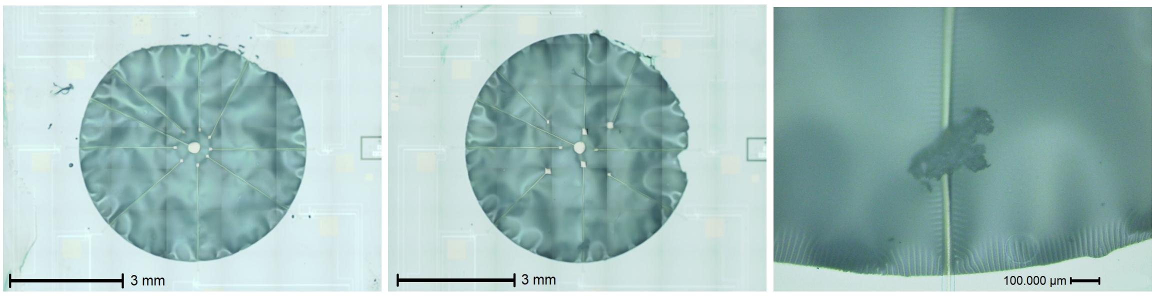

(g) Die 44: **O** 2.6mm 80μm overview (h) Die 47: Old Mixed design overview (i) Die 47: residue spot on electrode

Figure 5.8: Overview depictions of the fabricated chips, including defects on the PDMS sensing area. The design is noted for each die. All pictures capture the chip frontside.

The following couple of dies, 43 and 44, are characterized by long extensions and 80μm wide sensing pads utilizing the old control-gate pads. As seen in Fig 5.8.(f), the top right part of the PDMS released membrane is not well defined, but the PDMS layer is still supported by the Si substrate, making the chip measurement compatible. Similar appearance is noted for die 44 in Fig 5.8.(g). In Fig 5.8.(h), the only die with a mixed design is die 47 with old control-gate dimensions. The PDMS well is supported by the substrate on the side, so wet measurements can take place. Some residues are observed on the sensing well, like the one in Fig 5.8.(i), probably Al hard mask residues or PI that was not removed before the PDMS spin coating, that fortunately do not significantly inhibit the transparency of the well.

Visual inspection utilising scanning electron microscopy (SEM) was attempted as well, presented in Fig 5.9. The thick transparent PDMS layer hampers the effect of SEM microscopy, resulting in low resolution and distorted images. The PDMS membrane is easily charged, leading to dark images and necessitating low energy electron beams. Especially in the case of sample tilting, optical phenomena take place due to the thick transparent layer, resulting in the curved electrodes depicted in Fig 5.9.(b). Overall, capturing clear SEM images of the samples proved challenging, even though most of the fabricated structures belong to the μm range. For future attempts, gold sample coating is suggested, taking into account that the sample is not going to be further used for measurements.

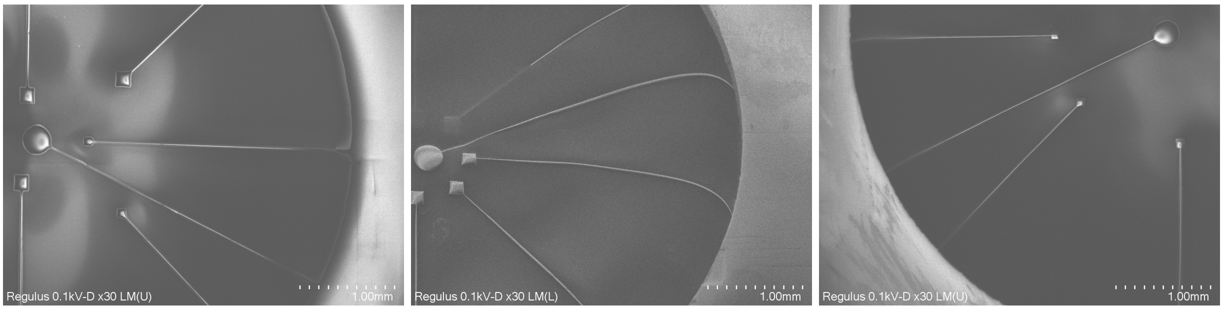

(a) Die 47: Old mixed design (Frontside) (b) Die 44: **O** 2.6mm 80μm (Backside) (c) Die 9: **N** 2mm 80μm (Backside)

Figure 5.9: SEM pictures of dies 47, 44 and 9 from left to right. Tilting the sample leads to distortion of the electrode shape for die 47.

5.5. Final Remarks

In this chapter, the fabrication process for the OoC is described and issues that appeared during the fabrication were discussed. Overall the defect of the process wafers is seemingly correlated to the wet etching during the formation of the first metal layer, indicating firstly that the high-resolution photolithography mask of the first metal layer is not compatible with wet etching. Secondly, the additional baking step towards photoresist hardening did not solve the overetching issues and led to increased micromasking.

Further study on the overetched transistors is presented in the next chapter. One of the process wafers broke during inspection, possibly due to accumulated stresses as a result of plasma etching equipment malfunction. Finally, the fabricated chips from the plasma etched wafer are presented, with die number 9 (N 2mm 80 μm) selected for further examination in Chapter 6.

6

Results and Discussion

Here, the fabrication and measurement results are presented and further discussed. Initially, the preliminary electrical characterisation measurements of the process wafers are examined, followed by additional investigation. In search of the process wafer failure source, microscopy pictures are introduced and a comparison between wet-etched and plasma-etched structures takes place. Additional trouble-shooting measurements are analyzed with the implementation of ADS models. Next, the measurements of the final OoC in both dry and wet conditions are presented and the behaviour of the sensor is analytically discussed. The advantages and drawbacks of the theoretical models are written down accompanied by some notes for future efforts.

6.1. Process wafers defect

As briefly discussed in the previous chapter, preliminary measurements showed that the chips on the three remaining process wafers, with the wet-etched Al layer, were not functional. After the bond-pad opening step, transistor characterization measurements can take place without wafer dicing, using a 4-probe Cascade microtech measuring station. During the measurements, the selected voltage can be applied on the source and drain terminals, the substrate and the control-gate. The formation of the Al structures during the wet etching was non-uniform, so the same nmos transistor was examined on every row of dies, along the length of the wafer. A drain voltage V_{DS} of 0.1V was applied to avoid the drain-induced lowering (DIBL) effect, resulting in the raw measurements of Fig 6.1.

The third process wafer, the one with the optimal Al structures after wet etching, yielded the depicted results. In the case of most transistors, including the ones on the other process wafers, the drain current I_D forms an arbitrary plot resembling noise in the range of pA. However, some transistors, show a slight effect of the control gate electrode bias on the sensor's output in the range of 10^{-11} A. Further investigation was followed to find the culprit of the wafer's impediment.

6.1.1. Visual Inspection

The first step of the investigation was visual inspection of the process wafers under SEM. Any deformities of the aluminum structures, such as extrusions, fractures or voids are associated with transistor dysfunction, while also the possibility of bringing phenomena was examined. Furthermore, the connections between the source and drain electrodes with the corresponding terminals were investigated for open circuit defects. An insight on the quality and structure of the gate oxide may also be constructive. In Figures 6.2 and 6.3 the results of the investigation are shown.

The transistor depicted in the first three images was previously used for measurements. Even though the gate electrode in between the source and drain electrodes is thinner than the 4 μm wide gate design on the high-resolution mask, it is well defined. The gate electrode structure is continuous with no shorts or fractures, but its width is not uniform along the length of the structure, most probably affecting the formation of the channel. Some spherical-like particles are also noticed on the high magnification

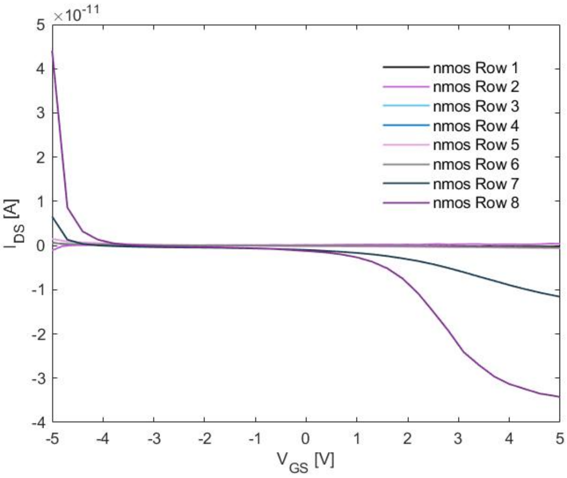

Figure 6.1: Raw transfer characteristics measurements from identical transistors along the length of the third process wafer. The source and substrate terminals are grounded and drain voltage of 100 mV is applied.

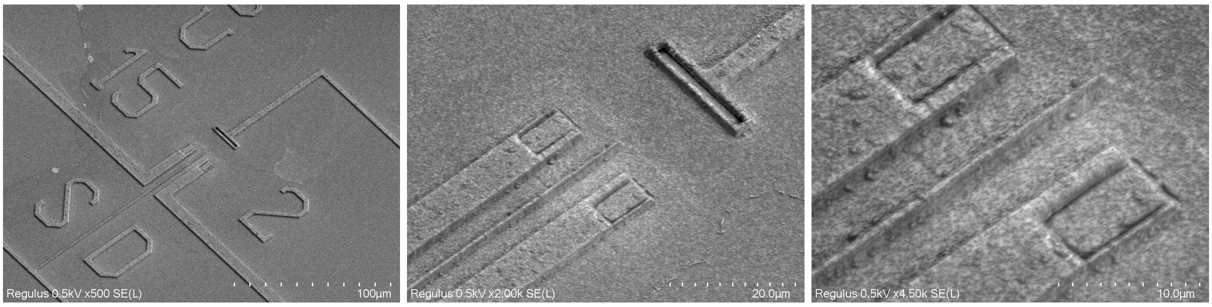

Figure 6.2: SEM pictures of the nmos transistor that was examined during the preliminary measurements. Higher magnification is used to thoroughly inspect the Al structures, with focus on the gate electrode in the middle. The sample was tilted at 35^o.

picture that are not identified. Finally, the connection between the upper electrodes through the contact openings and the terminals appear to be effective. On the next set of pictures, another nmos transistor of the same die is examined. Similarly to the previous transistor, the gate electrode is very thin without any other visible deformities and similar spherical debris is observed. Here, the effect of wet etching is visible on the aluminum layer on top of the contract openings.

Overall, no structural deformities were noted other than some of the effects of wet etching. The difference on the resulting structures between wet and plasma etching is better illustrated in the accumulated pictures of Fig 6.4. Here, transistors from the back-up wafer are compared to identical transistors from the process wafers. The first think to observe is the difference between the wet etched and plasma etched gate electrodes. The dimensions of said electrodes are significantly altered by wet etching, while the rest of the Al structures are also better defined in the case of plasma etching.

6.1.2. Additional measurements

To identify whether the sole factor of the transistor dysfunction is the over-etched gate electrode, the third process wafer was further used for measurements. The same nmos transistor was investigated on the third row of dies, aiming at higher output signals. It was observed that the over-etching was more intense on the periphery of the wafer compared to the central dies. Firstly, it should be noted that even though the dimensions of the gate electrode have been altered from the initial design, the gate still has an effect on the drain current as seen in Fig6.6. High values of applied potentials are needed to acquire some relatively meaningful signals, reaching at the higher an output of 1.4 nA. In both cases, biasing the gate seems to have negative effect on the sensor's signal.

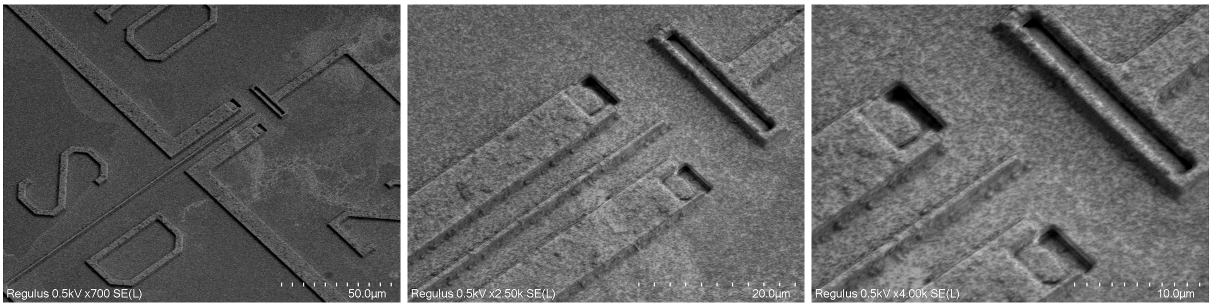

Figure 6.3: SEM pictures of another nmos transistor of the same chip for Al structure inspection. The sample was tilted at 35^o.

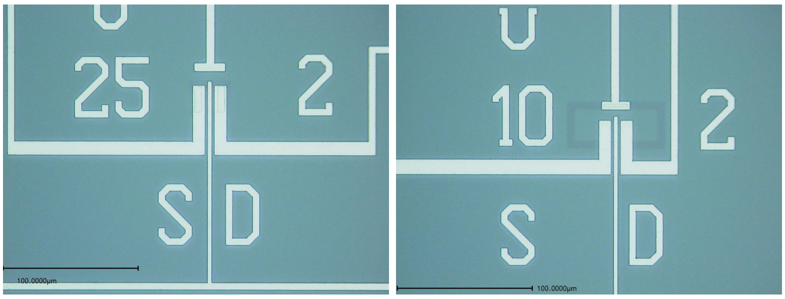

(a) Back-up wafer: nmos (b) Back-up wafer: pmos1

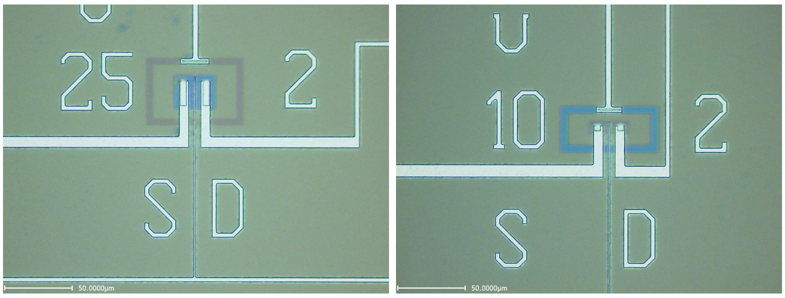

(c) Second process wafer: nmos (d) Second process wafer: pmos1

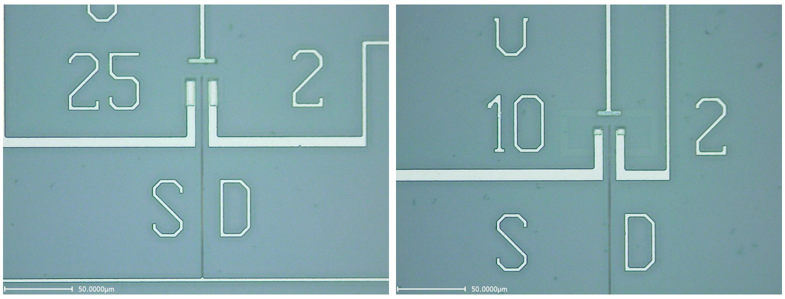

(e) Baked process wafer: nmos (f) Baked process wafer: pmos1

Figure 6.4: Comparison between resulting Al structures after plasma or wet etching for three transistors. The same nmos transistor structure was investigated under SEM and was characterized by the initial measurements.

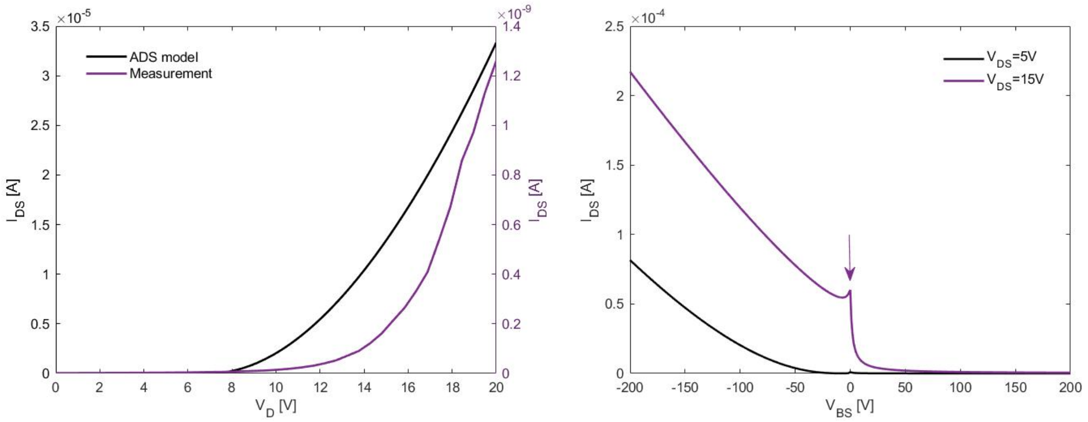

Figure 6.5: Response of the drain current I_D while aiming at channel inversion by biasing the drain or substrate terminals with zero gate voltage V_{CG}. On the left, an experimental measurement of the nmos is compared to the ADS model-predicted behaviour, indicating a significant deviation in the order of the I_D values. On the right, the ADS model predictions for channel inversion by biasing the channel indicate the need of very high applied voltage V_{sub}. The arrow shows the effect of the applied drain voltage V_{DS}.

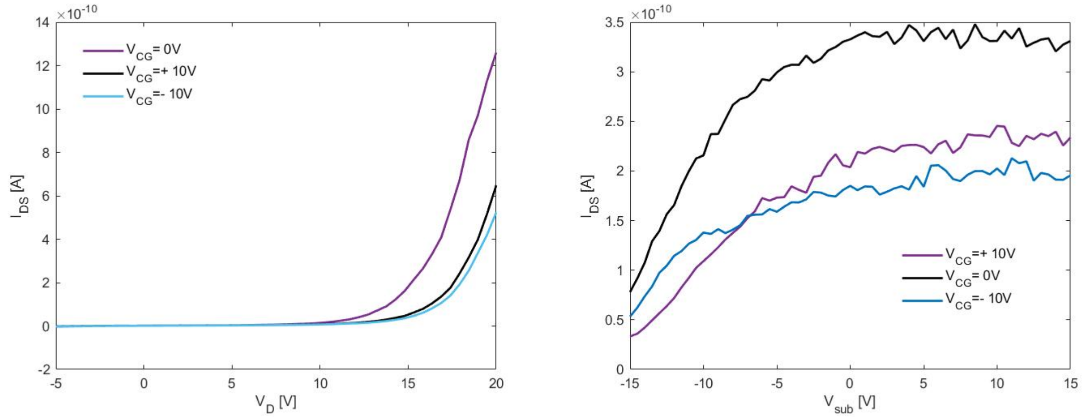

Figure 6.6: Drain current I_{DS} measurements indicating the effect of the gate electrode on the operation of the nmos wet-etched transistor. The substrate is grounded for the drain voltage V_D measurements. To achieve higher I_{DS} values when applying a range of substrate voltage V_{sub} values, a 20V voltage was applied on the drain.

If the rest of the transistor's structure is intact, without suffering from other shortcomings, biasing the drain or the substrate should create a p-n junction with a measurable signal. Towards this end, the effect of biasing the substrate V_{sub} was investigated, as seen in Fig 6.6, but no channel inversion was achieved for this voltage range. According to the ADS model for the FGFET sensor with dimensions fitting the measured transistor with the over-etched gate electrode, very high values of V_{sub} are required to achieve a significant I_D response. This explains the arbitrary plots of the I_D-V_{sub} diagram. Simultaneously biasing the drain to assist the p-n junction formation results in the small peak of Fig 6.5.

Regarding the drain voltage behaviour, in Fig 6.5 it is shown that for very high voltage values the drain current I_D significantly increases. The measurement I_D values in the range of nA do not correspond to the predicted behaviour by the ADS model, with the model indicating a difference of 4 orders of magnitude. However, the plot trends are similar and it is considered that I_D shows a diode-like behaviour between the drain terminal and the grounded source terminal.

Overall, the visual inspection indicated that the dimensions of the Al structures significantly change after wet etching, mainly because the used mask was intended for dry etching. If wet etching is selected as the Al layer patterning, a new photolithography mask with wider structures should be designed, taking

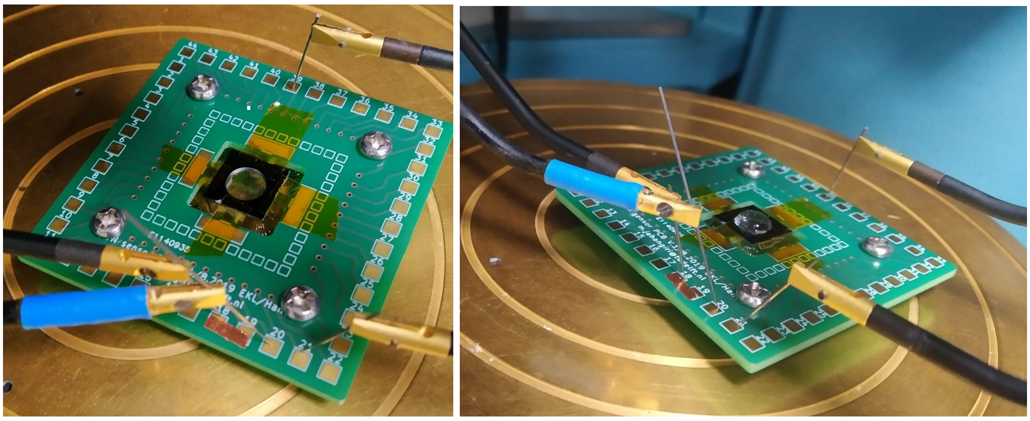

Figure 6.7: Pictures showing the 4-probe measurement station used for measurements in dry (left) and wet conditions (right). The PCB is placed on the station and the position of the needles is manually selected.

into account the excess material removal due to the isotropic etching. Nevertheless, the ADS model with the dimensions of the over-etched structures predicts a similar behaviour for the I_D response to the V_{DS}, with a significant difference in the order of magnitude. This deviation can either derive from ADS model inaccuracies or some visually non-identified transistor dysfunctions.

Due to the over-etched gate electrode, a bigger part of the gate oxide is exposed, leaving it vulnerable during the rest of the fabrication process. In general, the dimensions and quality of the gate oxide play a significant role on the transistor's operation and impurities can hinder its function. By applying low bias during the preliminary measurements, gate oxide related impeding phenomena such as hot-carrier injection and oxide breakdown are avoided. However, some fabrication steps like plasma-related and implantation processes also affect the quality of the gate oxide, by exposing them to stresses and charges [150]. In conclusion, gate oxide failures might partially explain the low drain current response of the sensors, but it should be noted that (other than the Al etching method) the same steps and recipes were applied during the fabrication of the back-up wafer.

6.2. Final organ-on-chip measurements

After the visual investigation of the diced chips in the previous chapter, die number 9 (N 2mm 80μm) was chosen for further measurements thanks to the well-defined PDMS sensing area and the implementation of the new control-gate dimensions. The chip is set on the PCB with Kapton tape, as seen in Fig 6.7, with thin wires connecting the chip bond pads with the PCB pads. A 4-point measurement Cascade station is used for measurements (Fig 6.7) by manually selecting the position of the needles. The pads corresponding to the source and substrate terminals are connected by a metalised tape and are grounded by using one probe station. The remaining probe stations are connected to the drain, control-gate and pseudoreference electrode pads. To examine the behaviour of the OoC measurements in both dry and wet conditions were taken.

6.2.1. Measurements in dry conditions

Initially the characteristics of the transistor were identified in dry conditions for the third nmos transistor of the OoC. The same ADS model that was used for examining the effect of the over-etched gates is utilised in Fig 6.8. It is shown that the ADS model can successfully predict the transfer characteristics, just by inserting the value of the threshold voltage V_{TH} and the dimensions of the nmos. On this operation mode, no bias is applied through the pseudoreference electrode so that the characteristics of the FGFET structure are studied.

The measured output characteristics of the nmos, as seen in Fig 6.8, show that the transistor does not enter saturation mode for the applied drain voltage of 2V. On the contrary, the ADS model predicts lower drain current I_{DS} response with the transistor entering saturation mode. Thus, even though the

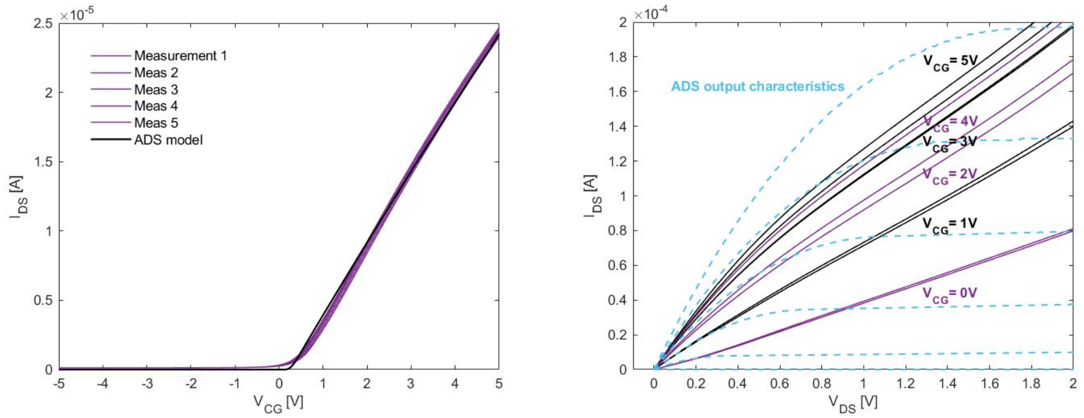

Figure 6.8: Transfer (left) and output (right) characteristics of the third nmos transistor on the ninth OoC during dry conditions, compared to the results of the corresponding ADS model. The characteristics are extracted without biasing the pseudoreference electrode. For the transfer characteristics, the drain applied voltage V_{DS} is 100 mV.

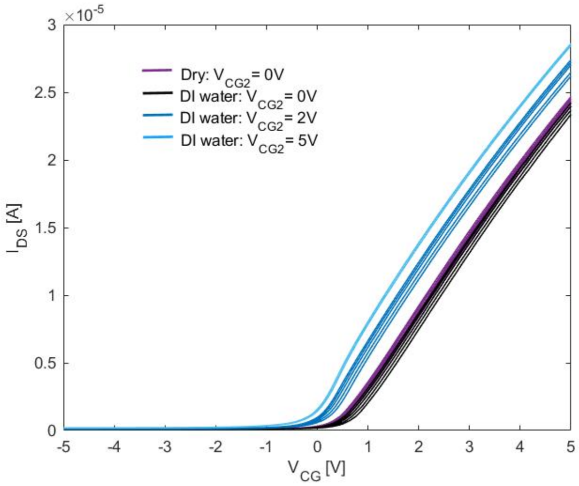

Figure 6.9: Transfer characteristics of the nmos for dry and DI water measurements. The effect of the pseudoreference bias V_{CG2} is shown. The applied drain voltage V_{DS} during the measurements is 100 mV.

ADS model can match the transfer characteristic behaviour of the sensor, it yields unreliable output characteristics plots. The model unreliability also hinders the process wafer failure in Fig 6.5. Replicating the same measurements in the future will show if the problem lies with the measurement or the ADS model.

6.2.2. DI water measurements

For wet measurements, a pipettor is used to deposit 10 μL of the selected liquid on the sensing well, thus forming a droplet like the one seen in Fig 6.7. After the removal of the liquid medium, the sensing area is left to dry for 10 minutes. Firstly, the OoC was tested with DI water, thus assisting the coupling effect between the planar electrode and the sensing pad. The results of the measurements are shown in Fig 6.9.

In the case of zero pseudoreference electrode voltage V_{CG2}, dry and DI water measurements show similar behaviour, with the indication that DI water measurements yield slightly lower drain current I_D values. Based on the theory, when in the presence of water the coplanar capacitance is increased, leading to a higher total capacitance. The effect of the coplanar capacitor contributes to the operation of the sensor when a voltage V_{CG2} is applied, with higher voltages leading to higher I_D values and a shift of the threshold voltage towards lower values. Even though the theoretical models did not predict

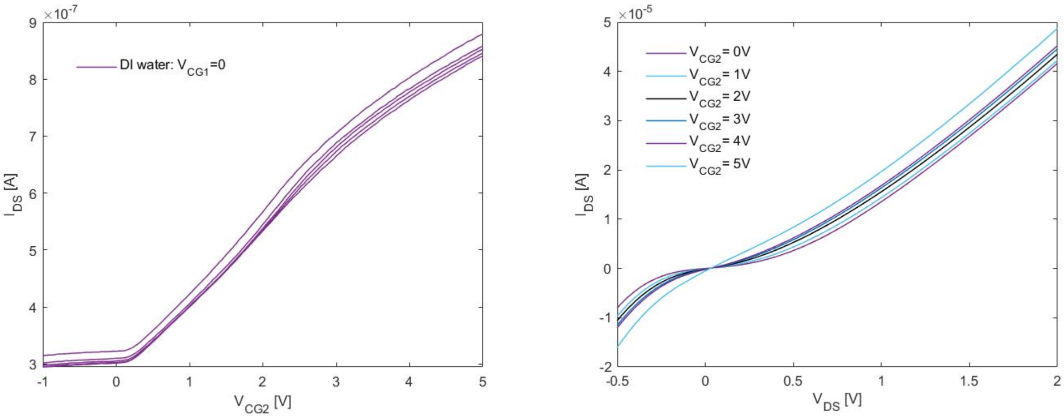

Figure 6.10: Characteristics of the nmos operating based on the coplanar gate voltage V_{CG2} for DI water measurements. No voltage is applied through the control-gate (V_{CG}= 0V).

a visible effect of the pseudoreference potential on the transfer characteristics, the measurements indicate otherwise.

So far, during dry measurements the control-gate operation mode was examined, and during DI water measurements both the afore-mentioned and the dual-gate operation mode were examined. In an effort to investigate the pseudoreference electrode operation mode and study whether the transistor is operational when only controlled by this electrode, the characteristics of the nmos were acquired. In Fig 6.10, the I_{DS} response to the pseudoreference voltage resembles transfer characteristics, showing that the sensor in this mode, even though operational, does not yield a significant signal. The transfer characteristics indicate I_{DS} values one order of magnitude lower than the ones on the control-gate operation mode for dry measurements. Both indicate that the sensor does not enter saturation mode.

6.2.3. KCl measurements

KCL was diluted in DI water with a ratio of 1:4, resulting in a 0.6 M KCl solution. A droplet of 10 μL was placed on the sensing well with the help of the pippetor. This solution was chosen to study the effect of ions on the sensor's output. The same line of investigation with the DI water measurements is followed.

The transfer characteristics of the nmos in Fig 6.11 clearly show the effect of the pseudoreference electrode bias. As a result of the ionic solution, the response of the sensor is higher compared to the dry measurement results, even in the case of zero applied V_{CG2}. In absence of the pseudoreference electrode effect, ion binding on the sensing area is enough to trigger an increased drain current. In this ionic environment, higher applied V_{CG2} leads to higher $\Delta I_{DS}/\Delta V_{CG}$ sensitivity. This effect is further amplified with higher V_{CG2} values. In this graph the threshold voltage shift is visible.

The effect of the ionic solution is also translated in the sensor's CG_2 characteristics in Fig 6.12. The transfer characteristic response is higher compared to the DI water measurements, while maintaining the same trend. The output characteristics do not show such a drastic I_D value increase and support the absence of saturation.

For comparison purposes, measurements on the dual-operation mode are plotted together in Fig 6.13. From dry to KCl conditions, the ions in the measurement medium increase accompanied by an increase of the output signal and a ΔV_{TH}. Measurements in ionic solutions of various concentrations are suggested to examine whether higher concentrations continue shifting the I_{DS} plot and if there is a saturation point. It is hypothesized that for high ionic concentration or after a time period the sensing pads will be saturated with ions.

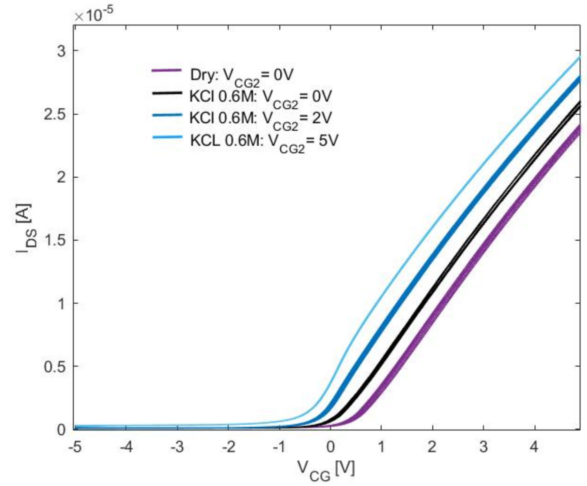

Figure 6.11: Transfer characteristics of the nmos for dry and wet measurements. An ionic solution KCl of 0.6M is used. The effect of the pseudoreference bias V_{CG2} is shown. The applied drain voltage V_{DS} during the measurements is 100 mV.

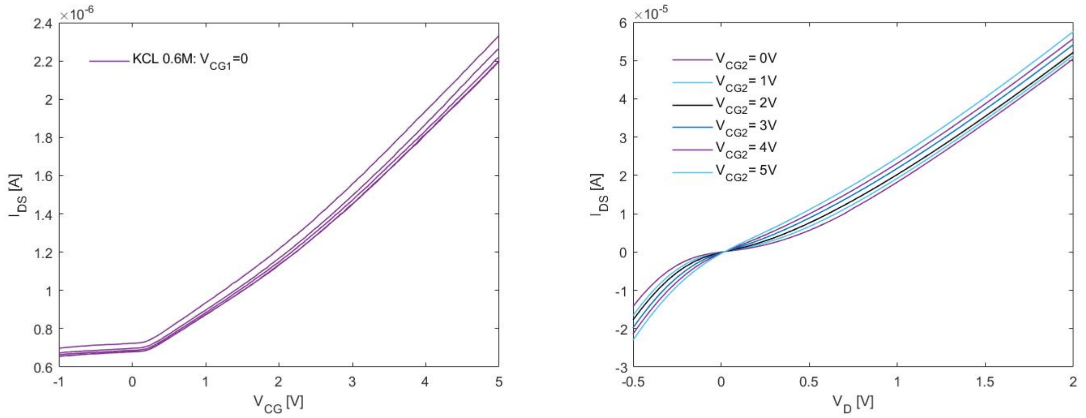

Figure 6.12: V_{CG2} characteristics of the nmos for wet measurements in 0.6M KCl. No voltage is applied through the control-gate (V_{CG}= 0V).

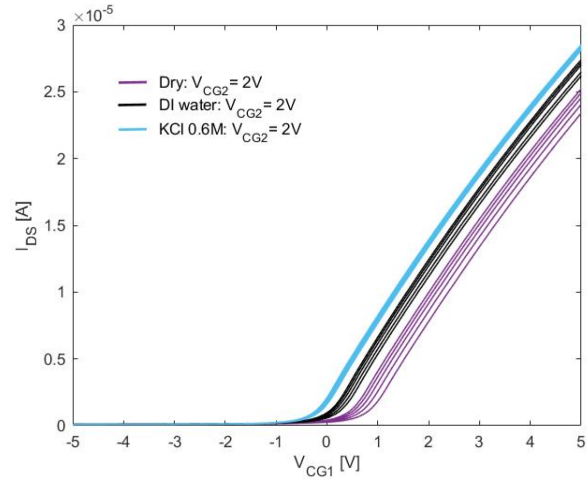

Figure 6.13: Overview of transfer characteristics of the nmos for dry and wet measurements. The same measurement conditions (V_{CG2}= 2V,V_{DS}= 0.1V) are applied.

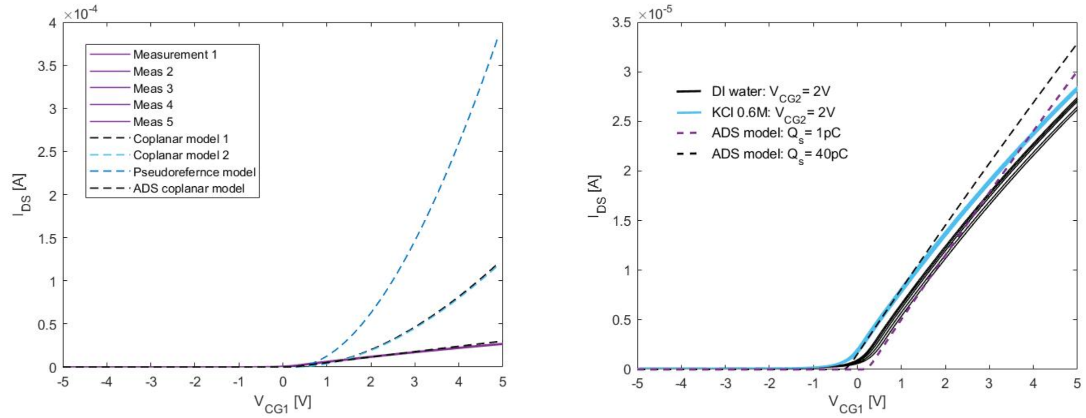

Figure 6.14: On the left, comparison between the DI water measurements with V_{CG2}=2V and the results of the mathematical models. On the right, the ADS model fit to the DI water and KCl measurements. In all cases the applied drain voltage is V_{DS}= 100 mV

6.3. Discussion

As indicated by the output characteristics presented in the previous section, the ADS model including the effect of the coplanar capacitor does not effectively predict the response of the system in relation to the drain voltage V_{DS}. The determination of the optimised dimensions for the new sensor design was based on this model. As a result, the new, 170 nm wide oxide thickness between the control and floating gates might not lead to the optimised sensor operation. The oxide thickness might be the factor that the sensor does not enter the saturation regime under V_{DS}=2 V.

Regarding the implementation of the planar/pseudoreference electrode, the theoretical models indicated that the V_{CG2} operation mode would not be effective, while a dual-gate mode (biasing both C_{CG} and C_{CG2}) can lead to increased $\Delta I_{DS}/\Delta V_{CG}$ slopes. However, it was experimentally shown by the characteristics of the V_{CG2} operation mode that the planar/pseudoreference electrode can modulate the charge distribution in the floating-gate electrode, but resulting in a lower signal compared to the conventional control gate. The combination of both gates in the ionic environment measurements (in KCl) led to a 16% $\Delta I_{DS}/\Delta V_{CG}$ increase for a pseudoreference voltage V_{CG2}= 5V.

Other definitions of sensitivity such as the response of the floating-gate voltage V_{Fg} or the threshold voltage shift ΔV_{TH} to the sensor's input were also studied with the mathematical models. Practically extracting the threshold voltage V_{TH} from measurements in wet conditions can be cumbersome, even though it is noted in many studies (see AppendixA), and thus was not under investigation after the measurements. In the design chapter it was mentioned that connection pads to the floating gate were included aiming at directly measuring V_{FG} during the experiments. Unfortunately, the current configuration of the 4-probe measuring system can not measure a signal without adding an input on the measurement point, meaning that in order to measure I_{FG} or V_{FG} the gate electrode would no longer be floating.

The big question remains, how does the coplanar/pseudoreference electrode affect the sensing gate and consequently the floating gate charge distribution. Applying the created mathematical and ADS models to the measurements, may provide an answer to this question. Fig 6.14 shows how the models fit to the studied measurement results. On the left, the mathematical models fail at predicting the sensor's behaviour during DI water measurements and resulting in higher drain current values. It is important to note that these models are based on the assumption that the sensor operates under the saturation regime and the measurements indicated that the fabricated sensor is not.

On the right of Fig 6.14 the fit between the ADS models and the measurements in wet conditions is depicted. The created models of the study use the sensing charge Q_s as input, so the concentration or pH of liquid measurement media is translated into the binding charge. In the case depicted in the figure, the models use a charge of 1 pC and 40 pC, corresponding to DI water and KCl measurements, respectively. Nevertheless, the ADS models still predict higher sensitivity than the measurements and do not predict the enhanced sensitivity for higher V_{CG2}.

Overall, the ADS models can be used for predictive purposes, but they show a deviation from experimental data on the prediction of the drain voltage V_{DS} effect. None of the models successfully describes the interaction between the coplanar/reference electrode and the sensing electrode, which in the design with the shorter extended electrodes was expected to deviate from the coplanar model. The latter necessitates that the half-distance between the two planar electrodes (in this design 400 μm) is shorter than the width of the electrodes. Investigation of more chips is believed to give a better insight on the predictability and improvement of the models.

6.4. Final Remarks

The first part of this chapter focuses on the investigation of the process wafers failure and it was indicated that:

- The wet etching significantly affected the formation of the Al structures, resulting in very thin gate electrodes with non-uniform width. SEM inspection and comparison with plasma etched structures support this argument.
- Despite the overetching, measurements show that the gate electrode still slightly affects the behaviour of the transistor.
- Investigative measurements proved the functionality of the transistor, but ADS simulations predicted higher drain current response. This disagreement is attributed to either ADS inaccuracies or non-identified transistor dysfunctions. Transistor impediments might be associated with gate oxide failures.

Next, measurements in dry and wet conditions took place for the selected OoC. Among the results of the measurements it is noted that:

- The output characteristics of the nmos for dry measurements do not agree with the ADS model and show that the nmos does not enter the saturation mode. Repeating this process will test the reliability of the measurements.
- In the case of DI water measurements, the mathematical models did not predict a drastic effect of the planar electrode bias on the the transfer characteristics. In contrast, the measurements show a visible shift on the drain current and threshold voltage values.
- Measurements in DI water and KCl show that the nmos is operational on the planar electrode bias mode, but yields a low output signal. The output characteristic support the finding that the nmos does not enter the saturation mode.
- During KCl measurements, the nmos responds to the binding of charges on the sensing pad without biasing the planar electrode. However, dual-gate operation mode results in higher drain current and $\Delta I_D/V_{CG}$ values.
- The mathematical models fail at predicting the behaviour of the sensor in wet conditions. This is attributed to the fact that the models describe the operation of the sensor under the saturation regime. The ADS model better fits the measurement results and is suggested for future modeling.
- It is not yet determined whether the planar electrode forms a coplanar capacitor or acts as a pseudoreference, as both models are far from predicting the sensor's behaviour.
- Similarly, it has not been identified whether the inclusion of the electrical double layer improves the predictive ability of the models.

For future efforts, measurements in ionic environments of various concentrations, including physiologically relevant media, are suggested. This way the sensor's limit of detection can be identified and compared with the concentration of the target-ions in physiological media, while also testing the sensor against the Debye limitation. The effect of ion binding on the sensing gates over time can also be studied.

7

Conclusion

7.1. Conclusions

Organs-on-chip are promising devices that can support real-time monitoring of complex microphysiological environments. Towards this end, a MOSFET-based device that implements flexible electrodes on an optically transparent sensing area was designed and successfully fabricated with an end-point application of in-situ blood-brain barrier (BBB) tissue ion environment monitoring. Before the designing process, a thorough investigation of MOSFET alternative solutions compatible with the BBB-on-chip idea took place, giving an insight on the available technology while also revealing a lack of understanding behind the operation mechanisms of the sensors. Taking the floating-gate MOSFET as a basis, theoretical models were studied and compared to face this absence. A common argument focuses on the inclusion of the electrical double layer (EDL) in the mathematical models for electrochemical sensing, but it only appears in the presence of a reference electrode. By implementing an additional planar electrode on the sensing area of the device, the proposed novel OoC manages to pave the way towards a solution to the EDL problem by combining a reference electrode-like structure with a floating-gate transistor.

Possible scenarios describing the interaction between the two structures were presented and analyzed, forming mathematical and simulation-based models for comparison with experimental data. The next point of focus was designing the second generation of the FGFET-based device while opting for higher sensitivity. It was indicated that the most practical definition of sensitivity for rapid sensor characterization was the response of the easily measurable drain current I_{DS} in relation to the sensor's input, whether be sensing charge, ionic concentration or voltage input. The planar electrode introduces further complexity to the system by adding parameters that contribute to the redistribution of charge in the floating gate, but after dimension tuning it can have an enhancing effect on the sensitivity. Some studies already tried replacing the conventional bulky reference electrode with a planar structure towards higher sensitivity. Here, the innovation lies with the implementation of the planar electrode on a flexible and transparent substrate, while also examining the effect of the electrode proximity to the sensing pads by allocating different designs.

During the fabrication process, the availability of the equipment dominated the time consumed and the technique used on each step. The decision of patterning the first metal layer by wet etching instead of plasma etching for structures that were not designed for this process is an example. This alternative step was identified as the main culprit of the process wafers failure. An identical plasma-etched wafer with operational transistors was successfully fabricated and was processed up to the stage of individual chips. Due to time restrictions only one of the chips was further investigated with a focus on the behaviour of one nmos transistor. The transistor can effectively operate in three modes: conventional control-gate mode, planar/pseudoreference electrode mode, and dual-gate mode. The third mode exhibits up to 16% $\Delta I_{DS}/V_{CG}$ increase compared to the first operation mode. In contrast with the prediction of the models, the nmos transistor does not enter the saturation regime, thus rendering the mathematical models based on this assumption ineffective.

The simulation-based model is promoted for application in the design of the next generation of BBB-on-chip, after some fine-tuning based on current measurements. At the same time, the layout of the mathematical models creates a solid basis to further development and understanding of the complex dual-gate operation. Let us not forget that the majority of biocompatible sensor studies ignore the underlying mechanisms of MOSFET operation and provide a superficial description. By clarifying the effect of the additional electrode and its relation to the electrical double layer formation, the upcoming sensors will be designed to achieve higher sensitivity and possibly overcome the Debye screening limitation.

7.2. Future work

While this thesis composes a full project from literature study and identification of alternative solutions to the modeling, design, fabrication and final characterization of the BBB-on-chip, it is by no means a project that has reached its end. On the contrary, there are several areas of improvement, further pushing the comprehension of the mechanisms behind this complex structure and working towards physiological relevance. A non exhaustive summary of such suggestions is discussed in this section, in hope of providing some direction towards the future of this project.

Electric double layer: To begin with, a possible area of focus can be the formation of the electrical double layer and whether it plays a role on the floating gate voltage in absence of a reference electrode in the measurement medium. The EDL is often mentioned in literature and adds an inhibiting capacitance to the system on the sensing area, while being associated with the Debye screening effect. Some studies have claimed overcoming this impediment, so further research on the techniques and structures utilized in such studies can be of significant assistance.

Selectivity optimisation: Secondly, the literature study provided an overview of available gate materials and coatings for selectivity optimisation. Based on the list provided in Appendix A different materials can be experimentally examined on the BBB-on-chip to increase its selectivity towards physiologically relevant ions, such as K^+ which is critical for biological processes. In a complex microphysiological environment such as the BBB tissue, selectivity is of high importance for the monitoring biological signals.

Study of the integrated planar electrode: Additionally, even though the idea of implementing a planar electrode during the fabrication of a chip has been tried before, it has yet to take the place of the conventional bulky Ag/AgCl reference electrode. Possible issues with utilizing the planar electrode could be identified by repetitive measurements on the fabricated chips, as erratic behaviour has been noticed for such structures. The function of the planar electrode can also be experimentally compared with the effect of dipping an Ag or Au wire, or even a Ag/AgCl reference electrode with the same bias, in the liquid medium, thus giving an insight on whether the planar electrode can be considered a pseudoreference electrode. Furthermore, physics-based models can be applied to predict the planar electrode behaviour, as the coplanar capacitance equation used in the models of this project is restricted by precise dimension limitations.

Study of fabricated OoCs: Due to time restrictions only one OoC was experimentally characterized, while the rest of the devices as seen in the overview of Section 5.4 remain uninvestigated. By comparing the measurements of different designs the effect of the control-gate and sensing pads dimensions as well as the length of the extended electrodes can be studied for all three modes of operation.

Physiological relevance: For wet condition measurements the effect of the same analyte in different concentrations can be examined and the sensor's limit of detection can be identified. In addition to that, measurements using physiological media (with high ionic strength) or ions in physiological concentrations, in the level of 5-105 mM K^+ for brain tissue [151], can be a critical indicator of the sensor's applicability as a BBB-on-chip. The replicability of the devices can be cross-checked as well.

Trans-epithelial electrical resistance (TEER): Finally, an important aspect of the BBB study is measuring trans-epithelial electrical resistance (TEER) across the barrier, which characterises the permeability of the BBB. TEER measurements will give an insight on how drugs enter the central nervous system through the barrier. Future projects should focus on enabling TEER measurements on the BBB-on-chip by either integrating micro-electrodes on the sensing area or utilizing the existing extended electrodes for this purpose. Again, the use of a bulky external measurement electrode should be avoided to maintain the OoC's portability.

A

Appendix - A

During the literature search, several studies of FET-based biosensors were identified. The details of said studies are summarized in the following tables, categorized based on transduction material and geometry. The tables give an overview of the applications of FET-based sensors, including information on functionalization and type of measurement medium.

Table A.1: Analytical characteristics of some silicon-based FET biosensors studies, grouped by structural category. N.A. stands for not available and LOD corresponds to limit of detection.

Device	**Detection Layer**	**Target**	**Medium**	**Sensitivity**	**Reference**
ISFET	Si_3N_4	pH	20:1 buffered HF	56.3mV/pH, pH<6.5 46.8mV/pH, pH>6.5	Bousse *et al.* [46]
ISFET	Ta_2O_5	pH	PBS	ΔI_{DS}= 55.4 $\pm$ 8.14 μ A	Braeken *et al.* [152]
	glutamate oxidase	L-glutamate	PBS	LOD: 100nM, pH=7	
ISFET	platinum silicide	K^+ ions	0.2M NaCl +0-0.1M KCl	56mV per decade	Smith *et al.* [153]
ISFET	Si_3N_4	pH	2% tris buffer solution +HCl or NaOH	59$\pm$0.9mV/pH, pH: 2-10	Castellarnau *et al.* [138]
ISFET	Si_3N_4	pH	N.A.	56mV/pH	Martinoia *et al.* [154]
ISFET	N_2OSi_2	pH	N.A.	40mV/pH	Milgrew *et al.* [40]
ISFET	Ta_2O_5	pH	HCl+NaOH solutions	45mV/pH, pH: 1-14	Cheah *et al.* [155]
ISFET	PI	pH	N.A.	2.6mV/pH	Moser *et al.* [156]
	Si_3N_4			6.35mV/pH	
	SiO_2			21.62mV/pH	
MOSFET	SiO_2	DNA	ss-DNA in PBS, pH 7	ΔV_T=+1.92V	Dashiell *et al.* [115]
MOSFET	PLL +DNA probes	DNA hybridization	825mM for a 5×saline sodium citrate buffer	LOD: 2nM	Fritz *et al.* [116]
MOSFET	thiolated-ssDNA probes	DNA hybridization	PBS	ΔV_T=+1.45V	Kim *et al.* [117]
EGFET	NH_3 plasma treated ITO	pH	0.1M NaOH+0.1M HCl, PBS, pH: 2.1-12.1	50mV/pH	Yang *et al.* [52]
	urease	urea	urea in 5mM PBS	62.4mV/pC, 0.01M	
EGFET	SnO_2/ITO	pH	PBS, pH: 2-9.7	60.9mV/pH	Chen *et al.* [53]
	urease	urea	5mM urea in PBS	0.31-120mg/dl	
EGFET	boronic acid	pH	pH:2-12	65.11mV/pH	Singh *et al.* [51]
	modified RuO_x	glucose	0.5mL serum with 10mM PBS, pH 7.4	6.89mV/mM, 1-8mM	
EGFET	anti-HbA1c	HbA1c	PBS, pH 7.4, 0.1mM	4-24μg/mL	Bian *et al.* [57]
	anti-Hb	Hb		60-180μg/mL	
EGFET	Al_2O_3	H^+	solution pH: 6-8	37.45mV/mM	Lin *et al.* [148]
		glucose	2-8mM, 5%w/w solution	7.00mV/mM	
		urea	1-32mM, 25%w/w solution	8.01mV/mM	
EGFET	monoclonal ab-MA	microalbumin (MA)	1% BSA	1800% at 1μg/mL 7000% at 10μg/mL	Ahn *et al.* [157]
EGFET	SiO_2	pH	10μL drops pH buffer and $H_2SO_4/NaOH$ solution	36.5mV/pH pH 1-14	Prodromakis *et al.* [55]
EGFET	Si_xN_y/Pt TiO_2/Au	pH	buffer solution pH: 1,7,14	35mV/pH 22mV/pH	Prodromakis *et al.* [56]
EGFET	K^+ sensitive membrane	K^+	100mM NaCl+10mM Na_2PO_4 buffer+KCl	15mV/log[K^+]	Odijk *et al.* [54]
FGFET	thiolated DNA strands	DNA hybridization	0.1mM in DI	N.A.	Barbaro *et al.* [58]
FGFET	thiolated DNA strands	DNA hybridization	1M NaCl TE buffer	100pM-100nM	Barbaro *et al.* [118]
FGFET	nitride layer	ions	1μL KCl electrolyte 1μL PLL electrolyte	N.A.	Chengwu *et al.* [119]
FGFET	SiO_2	ions	0.8-1.2μL of 0.01%w/v poly-L-histidine solution	ΔV_T=-0.1V	Chen *et al.* [26]
			of 0.01%w/v PLL	ΔV_T=-0.08V	
			of 0.5%w/v poly-glutamic acid solution	ΔV_T=+1.2V	
			of 0.5%w/v poly-asparatic acid solution	ΔV_T=+0.35V	
CvMOS	poly-Si	ions	water (pH=5.5), acetone (pH=7), saline solutions	See Table 1 from paper	Shen *et al.* [120]
CvMOS	Al_2O_3	pH	TE buffer	50mV/pH,pH 1-12	Jayant *et al.* [142]
CvMOS	PLL+ssDNA probes	DNA hybridization	5μM in TE	ΔV_T=0.25V	Jayant *et al.* [140]
ISFGFET	Al_2O_3	pH	pH 4-7 buffer	ΔV_T=53mV/pH	Kaisti *et al.* [31]
			pH 7-10 buffer	ΔV_T=48.8mV/pH	
ISFGFET	TANI	ammonium gas	N.A.	detection:70ppm	Zhao *et al.* [60]
ISFGFET	Al_2O_3	pH	10μL pH buffer	57mV/pH, pH:4-7	Zhang *et al.* [61]
			pH 7-10 buffer	49.5mV/pH	
	PANI/DNNSA		pH 7-10 buffer	106mV/pH	
DG-ISFET	SiO_2	pH	pH 3-12 solution	124mV/pH, d=100nm 170mV/pH, d=50nm 158mV/pH, d=20nm d: channel thickness	Park *et al.* [65]
DG-ISFET	hafnium oxide	pH	10mM PBS solutions (HCl,NaOH),pH 4-16	mean 45.8$\pm$5.4mV/pH up to 84mV/pH	Duarte *et al.* [66]

Table A.2: Analytical characteristics of some studies working on organic semiconductor-based FET biosensors. N.A. stands for not available, LOD for limit of detection and NCR for normalized current responses. The label EG-FET corresponds to electrolyte-gated FET, while EGFET stands for extended gate FET and there are different categories of structures.

Device	**Detection Layer**	**Target**	**Medium**	**Sensitivity**	**Reference**
OTFT	Ta_2O_5	pH glucose	pH buffers 10^{-5}-10^{-2}M solutions	0.3 μ A/pH unit, V_{DS}=-0.8V 0.3 μA/decade, V_{GS}=-0.5V, V_{DS}=-1V	Bartic *et al.* [158]
OTFT	ss-DNA ds-DNA	DNA hybridization	2.0 μM DNA in 75 mL PBS	N.A.	Yan *et al.* [152]
OTFT	Biotinylated semiconductor polymer (F8T2)	bovine serum albumin (BSA) avidin	$8 \cdot 10^{-7}$ in DI water or buffer solution $6 \cdot 10^{-7}$ in DI water or buffer solution	N.A.	Kim *et al.* [159]
OTFT	thiol-modified ss-DNA	DNA hybridization	$100\mu M$ in DI	ΔV_T=+0.5V, ΔI_{DS}=+0.44 μA LOD: 100 nM	Park *et al.* [160]
OECT	PEDOT:PSS	cell activity	Human cancer cell-lines Fibroblast cell-lines in incubator	ΔV_G=150mV, V_{DS}=-0.1V ΔV_G=70mV, V_{DS}=-0.1V	Lin2010 *et al.* [32]
OECT	MWCNT-CHIT/GE electrode Au electrode Pt electrode	Dopamine oxidization	50 nM in PBS, pH 7.2	NCR: 0.01, V_D=-0.2V NCR: 0.037, V_D=-0.2V NCR: 0.042, V_D=-0.2V LOD: 5 nM	Tang *et al.* [161]
OFET	Ta_2O_5	pH	solution pH:8-14	ΔI_{DS}/pH=0.36 μA/pH, V_{DS}=-7V	Gao *et al.* [121]
ISOFET	Mylar insulator	pH	solution pH:4-10	10%/pH	Loi *et al.* [122]
ISOFET	SiN:H on parylene-C	pH	solution pH:4-10	0.8 μA/pH, V_D=-60V, V_G=-50V Relative: 8%/pH	Diallo *et al.* [123]
EG-OFET	CA-BA-based SAM	Dopamine (DA)	DA in 50 mM PBS, 1 pM, 1 nM, 1 μM, 1 mM pH 8.5	ΔV_T=350mV, 1mM, V_{DS}=-0.1V See study's fig.4b	Casalini *et al.* [79]
OCMFET	DNA probes	DNA hybridization	PBS, pH 7, 50mM NaCl	LOD: 1pM	Lai *et al.* [147]
OCMFET	O_2 plasma-activated Parylene-C	pH	500 μL PBS	1.4V/pH, pH 6-8	Spanu *et al.* [81]
OCMFET	hairpin-shaped DNA probes	DNA hybridization	10nM, 1nM, 100pM, 10pM in solution	LOD: 100pM	Napoli *et al.* [162]
OCMFET	HS-ssDNA	DNA hybridization	3μL drop of DNA-TE (1M NaCl) solution	detection 10nM	Demelas *et al.* [16]
ISFGFET	PANI-ES	cationic PEI	0.5 μL PEI aqueous solution	500pg/mL	Zhang *et al.* [163]
EGOFET	streptavidin	biotinylated IgG	D-PBS solution with 0.1 wt.%BSA	LOD: 1.2 μg/mL=8nM	Minamiki *et al.* [84]
EGOFET	anti-human IgA antibody	IgA	0-50 μg/mL in PBS with 0.1 wt% HSA	LOD: 2.1 μg/mL	Minamiki *et al.* [86]
EGOFET	PANI functionalization	pH	PBS + pH 4 citrate buffer, diluted HCl solution	9.1mV/pH, pH 4-7	Kaisti *et al.* [164]
EGOFET	PANI-DNNSA	K^+	Nacl + KCl diluted in DI	58.2 ± 0.9mV/dec, KCl 59.4 ± 0.6mV/dec, KCl+NaCl	Kaisti *et al.* [85]
EGOFET	artificial phosphoprotein receptor	α-casein	HEPES solution and pH 7.4 buffer solution with NaCl (100mM)	LOD: 0.22ppm	Minamiki *et al.* [124]
EGOFET	anti-CgA antibody	hCgA	PBS+0-50 μg/mL with HSA (0.1wt%) artificial saliva	LOD: 0.31μg.mL (6nM) LOD: 0.11μg/mL (2nM)	Minamiki *et al.* [125]
EGOFET	ITO/PET	pH	solution pH 2-12	good linearity V_{out}/pH	Tang *et al.* [126]
EGOFET	PEGs	GFAP	0.5-100ng/mL solution	LOD: 1ng/mL	Song *et al.* [127]
EGOFET	NH_2-group SAM	pH	$C_6H_8O_7$, Na_2HPO_4 solution pH 2.5-6	N.A.	Caboni *et al.* [83]
EG-FGFET	ssDNA probes	DNA hybridization	10nM-10μM in TE buffer, 1.0M NaCl	LOD:10nM	White *et al.* [128]
EG-FGFET	DNA aptamer	ricin	1ng/mL in PBS 10ng/mL in orange juice, milk	LOD:30pm LOD:300pM	White *et al.* [129]
EG-FGFET	carboxylic acid-terminated SAM	pH	pH 4-11 solution 1mM-1M	75mV/decade	Thomas *et al.* [130]

Table A.3: Analytical characteristics for the alternative technology field-effect sensors studied within this literature study. N.A. stands for not available, LOD for limit of detection and ΔG for conductance change. The noted voltage shifts ΔV_{GS} correspond to the effective gate voltage shifts.

Device	**Detection Layer**	**Target**	**Medium**	**Sensitivity**	**Reference**
HFET	biotin	streptavidin (SA)	aqueous solution	N.A.	Kang *et al.* [88]
HFET	single stranded DNA (ss-DNA)	DNA hybridization	1μM/1M in NaCl buffer solution	N.A.	Kang *et al.* [131]
HFET	biotin SA	SA interferonγ (MIG)	Phosphate buffered saline (PBS)	25-250 ng/mL	Gupta *et al.* [87]
HFET	biotin	SA	0.1×PBS 0.25×PBS 1×PBS	15.2% 11.3% 5.8%	Wen *et al.* [135]
HFET	CRP-antibodies	C-reactive protein CRP	PBS	10ng/mL	Lee *et al.* [136]
HFET	SA MIG antibodies	biotin MIG	PBS serum urine sample	LOD 16aM/163mM 100 ng/mL $\Delta I_{DS} = 8\%$	Wang *et al.* [89]
EIS		pH	Titrisol, Merck pH:4-8	54 mV/pH	Schöning *et al.* [93]
	penicillinase	penicillin	0.01-100 mM solution	45 mV per decade	
EIS	penicillinase	penicillin	polymix buffer	90 mV/mM at 0.01–1 mM	Schöning *et al.* [165]
EIS	mouse IgG antibodies	goat anti-mouse IgG	0.05M PBS	80 μg/mL at pH:7.2	Betty *et al.* [165]
EIS	anti-rabbit IgG	rabbit IgG antibodies	5 μg/mL in acetic/ acetate buffer, pH:5	LOD 10 ng/mL	Meskiny *et al.* [95]
DMFET	biotin	SA	300nM SA/PBST	N.A.	Im *et al.* [98]
SiNWFET	biotin	SA	250nM SA/PBS	at least 10 pM	Cui *et al.* [106]
SiNWFET	peptide nucleic acid (PNA)	DNA mutation site	100fM MU DNA solution	LOD 10fM	Hahm *et al.* [104]
SiNWFET	Abl protein	ATP binding or inhibition	ionic strength of buffer 10-1000×analyte concentrations	at least 100 pM	Wang *et al.* [132]
SiNWFET	monoclonal antibodies (mAbs)	cancer markers	multiplexed detection, see paper's Table 1	at least 0.9 pg/mL in undiluted serum	Zheng *et al.* [133]
SiNWFET	biotin	anti-biotin	1mM NaCl/1mM PBS solution 100 ng/mL in solution	$\Delta G = 0.02 \pm 0.01$nS, V_{DS}=-0.4V $\Delta G = 45 \pm 0.1$nS, V_{DS}=-0.9V $\Delta V_{GS} = 7.2 \pm 0.3$mV	Chen *et al.* [101]
SWNTFET	glucose oxidase (GO_x)	pH glucose	$pH \simeq 5.5$ (0.1 mM KCl in milli-Q water) $pH \simeq 4$ (0.1 mM HCl in milli-Q water) 0.1 M in milli-Q water	ΔV_{GS}=20mV, ΔG=0.3 nS for pH:4-5.5 ΔG=+10%	Besteman *et al.* [166]
SWNTFET	Aminated ssDNA	DNA hybridization	0.1 mg/mL C-ssDNA in 2×SSC buffer (300mM NaCl, 30mM sodium citrate)	N.A.	Martinez *et al.* [107]
CNTFET	IgE aptamers	immunoglobulinE (IgE)	PBS	efficient detection: 250 pM-160 nM	Maehashi *et al.* [105]
SWNTFET	PSA antibodies	prostate specific antigen (PSA)	physiological concentration PBS	efficient detection: 5 ng/mL, $\Delta I_{DS} = 2\%$	Li *et al.* [134]
SWNTFET	T-PSA-mAb	Total PSA (T-PSA)	Milli-Q water	LOD 0.25 ng/mL	Okuno *et al.* [167]
SWNTFET	DNA probes	DNA hybridization	10 fM-10 μM in PBS	$\Delta G/G_0 = 8\%$, 1nM, 1 floating electrode $\Delta G/G_0 = 21\%$, 1nM, 7 floating electrodes	Kim *et al.* [168]
GFET	graphene amines (GAs) ssDNA	single bacterial cell DNA	N.A. N.A.	$\Delta G = +42\%$, single cell $\Delta G = +71\%$	Mohanty *et al.* [110]
GFET	BSA antibodies	bovine serum albumin (BSA)	PBS	10 mM, pH=6.8	Ohno *et al.* [109]
GFET	DNA probes	DNA	40 μL in PBS	efficient detection: 0.01 nM	Dong *et al.* [108]
GFET	CD36 receptors	singular malaria-infected red blood cell	N.A.	$\Delta G = 5.1 \pm 0.3\%$ trophozoite-cell $\Delta G = 8.4 \pm 1.3\%$ schizont-cell	Ang *et al.* [169]
GFET	anti-E.coli antibodies	E.coli activities	PBS	10 cfu/mL E.coli detection	Huang *et al.* [170]

B

Appendix - B

Here, the ADS schematics that correspond to the models described in the Theoretical Background and Design chapters are presented. The ADS models were used to extract transfer and output characteristics of the floating-gate based sensors. They same models were used for sensitivity studies by activating the parameter sweep components.

In the ADS models, the floating gate is grounded through a large resistor in series with a voltage source. To replicate the effect of charge binding on the floating electrode, a voltage-controlled voltage source was implemented. The model parameters that were not directly derived from the geometry of the sensor, such as channel dimensions and control gate dimensions, were determined from measurement data. Thus, MOSFET-related parameters such as transconductance coefficient k and channel length modulation λ were extracted from measurement plots and the rest of the parameters, bulk threshold γ, mobility modulation θ, and so forth, derived from fitting of simulation to measurement data.

A previous effort, again from the same bachelor graduation project, focused on creating an ADS model for the FGFET operation, including the EDL effect. By implementing the equation system written down by Kaisti et al. [31], the transistor operation is correlated with the electrolyte characteristics. The electrolyte dissociation constants, pH and molarity, modulate the sensor's output. These chemical parameters are expressed in relation to the double layer surface charge $sigma_0$ and state the difference between the mathematical and ADS models.

In the ADS model, the surface potentials Ψ_{DL} and Ψ_0 are coupled to behavioural voltage sources connected to the floating gate (Fig B.2). Symbolically Defined Devices (SDDs) are used to implement the behavioural voltage sources. The output potential of an SDD can be defined as a combination of input potentials in complex equations. In this way, the voltage sources solve the system of non-linear equations resulting in the output drain current I_D.

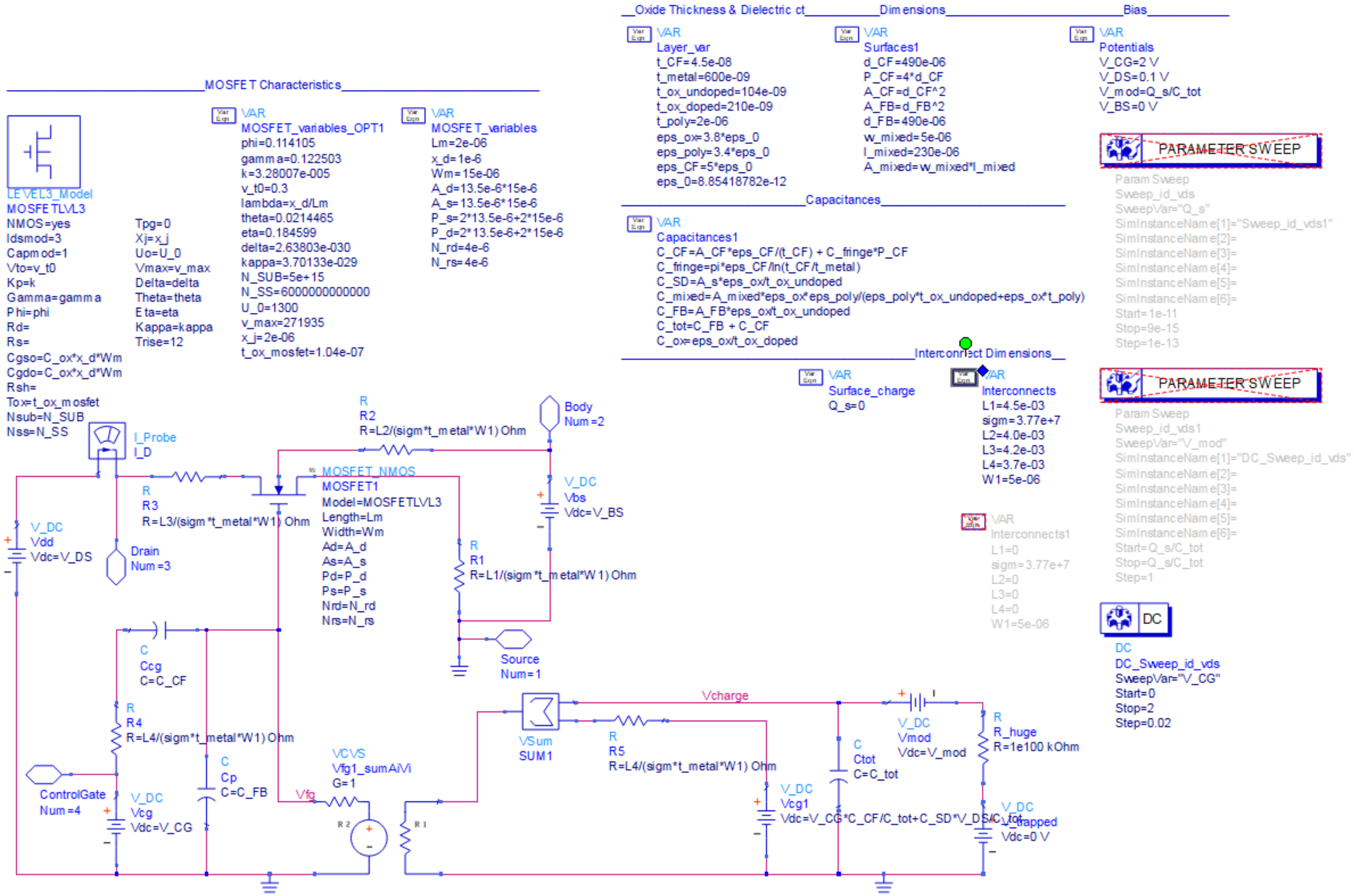

Figure B.1: ADS model implementing a floating gate. This model was used for extracting MOSFET characteristics and replicating the operation of the sensor with the sensing charge Q_s as input. The MOSFET parameters were determined based on previous measurements.

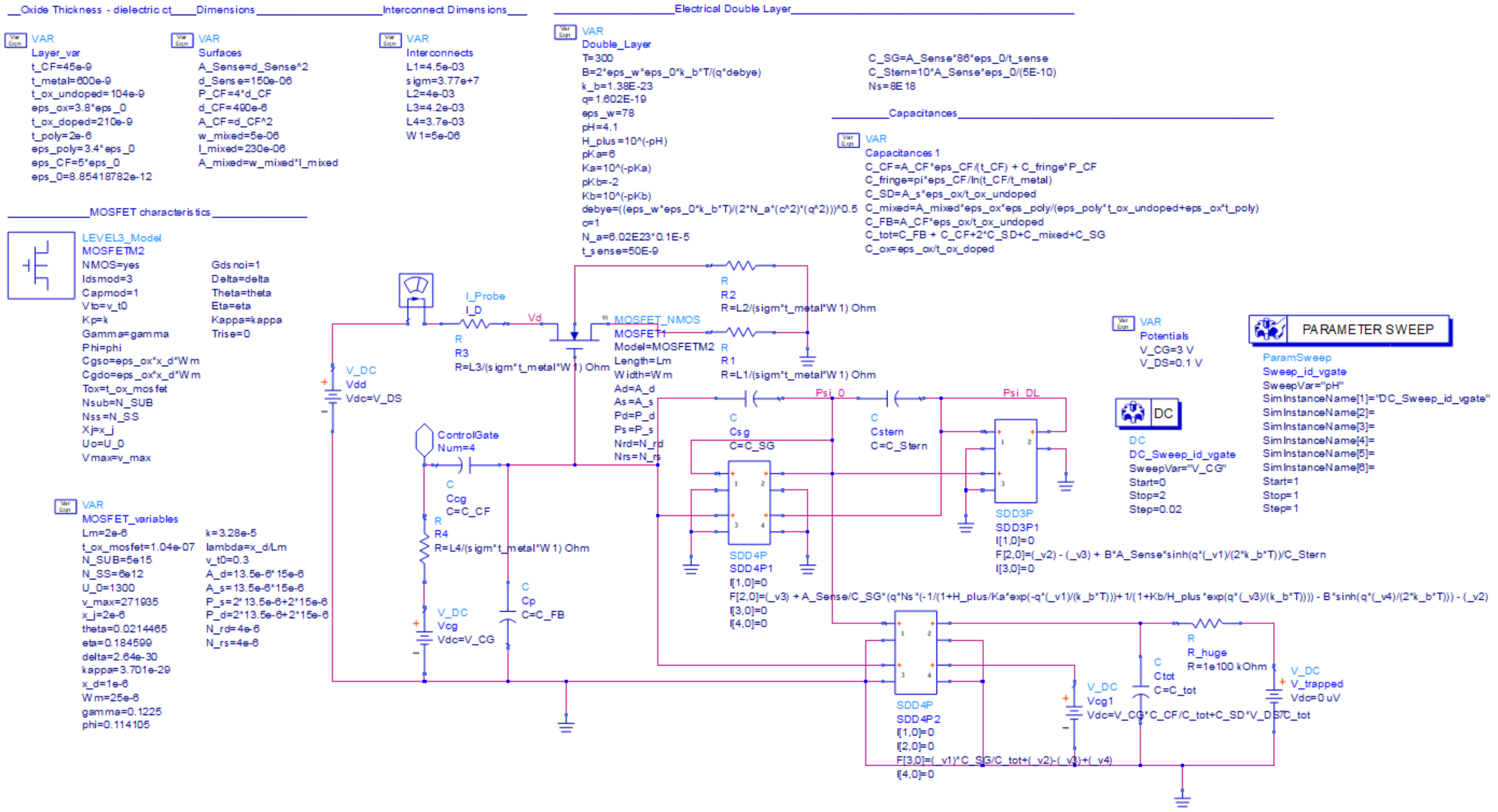

Figure B.2: ADS model implementing the floating gate coupled to Symbolically Defined Devices (DDVs) that insert the equations of the electrical double layer. This model simulates the response of the sensor when in contact with a liquid of defined pH. The MOSFET parameters were determined based on the previous model.

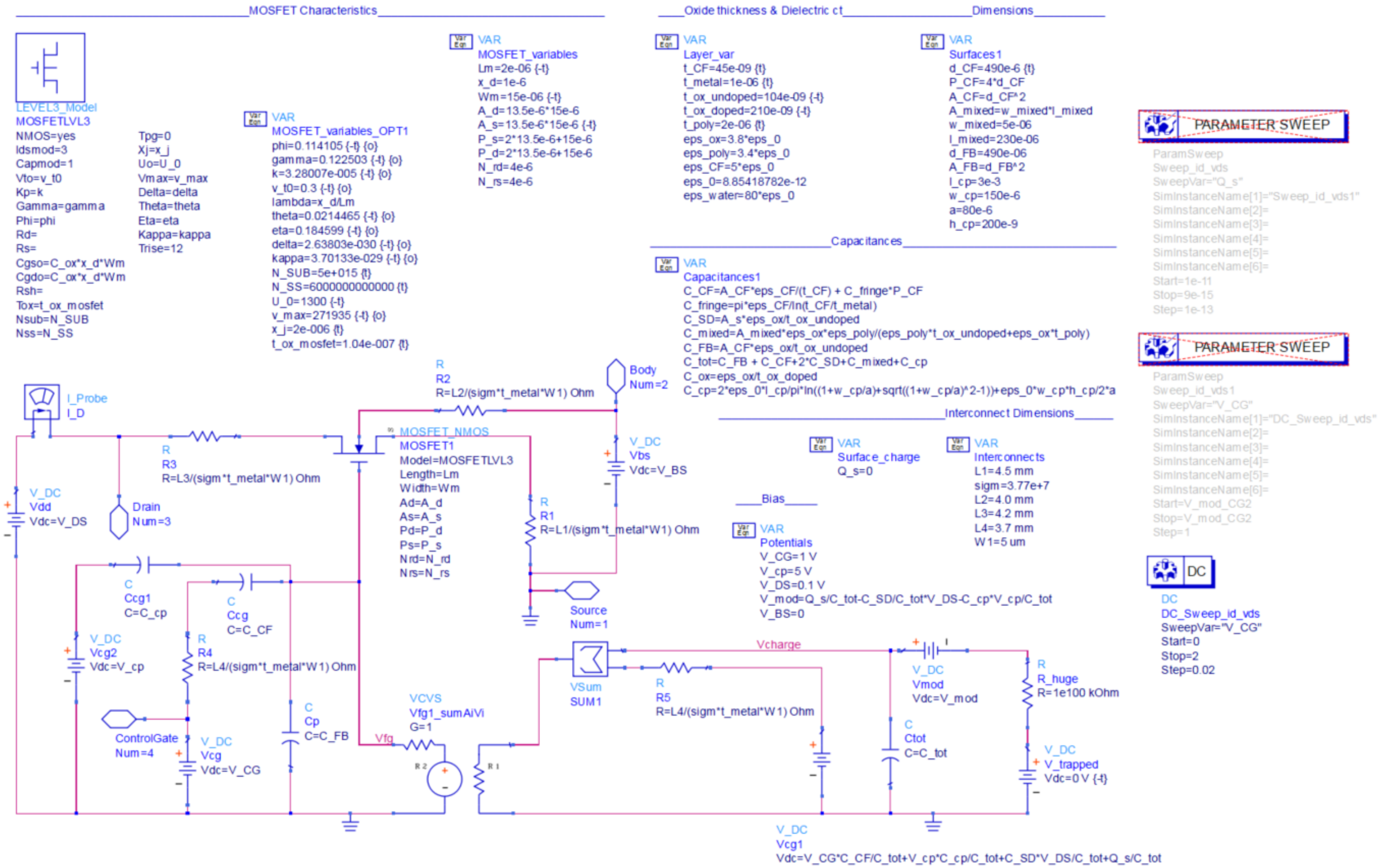

Figure B.3: Coplanar ADS model based on the FGFET model with an additional parasitic capacitance C_{cp} connected to the floating gate node. The equations of the coplanar model are incorporated in the ADS model. This model simulates the response of the sensor to a bound charge on the sensing pad.

Bibliography

[1] Sangeeta N Bhatia and Donald E Ingber. “Microfluidic organs-on-chips”. In: *Nature biotechnology* 32.8 (2014), p. 760.

[2] Kacey Ronaldson-Bouchard and Gordana Vunjak-Novakovic. “Organs-on-a-chip: a fast track for engineered human tissues in drug development”. In: *Cell stem cell* 22.3 (2018), pp. 310–324.

[3] Uwe Marx et al. “‘Human-on-a-chip’developments: a translational cutting-edge alternative to systemic safety assessment and efficiency evaluation of substances in laboratory animals and man?” In: *Alternatives to laboratory animals* 40.5 (2012), pp. 235–257.

[4] Boyang Zhang et al. “Advances in organ-on-a-chip engineering”. In: *Nature Reviews Materials* 3.8 (2018), pp. 257–278.

[5] N Beißner, T Lorenz, and S Reichl. “Organ on chip”. In: *Microsystems for pharmatechnology*. Springer, 2016, pp. 299–339.

[6] N Joan Abbott et al. “Structure and function of the blood–brain barrier”. In: *Neurobiology of disease* 37.1 (2010), pp. 13–25.

[7] Elaine Nicpon Marieb and Katja Hoehn. *Human anatomy & physiology*. Pearson education, 2007.

[8] Arthur M Butt, Hazel C Jones, and N Joan Abbott. “Electrical resistance across the blood-brain barrier in anaesthetized rats: a developmental study.” In: *The Journal of physiology* 429.1 (1990), pp. 47–62.

[9] DJ Begley. “Structure and function of the blood–brain barrier”. In: *Enhancement in drug delivery. CRC Press, Boca Raton* 575 (2007).

[10] N Joan Abbott, Lars Rönnbäck, and Elisabeth Hansson. “Astrocyte–endothelial interactions at the blood–brain barrier”. In: *Nature reviews neuroscience* 7.1 (2006), p. 41.

[11] Brian T Hawkins and Thomas P Davis. “The blood-brain barrier/neurovascular unit in health and disease”. In: *Pharmacological reviews* 57.2 (2005), pp. 173–185.

[12] Hande Aydogmus et al. “FET-Based Integrated Charge Sensor for Organ-on-Chip Applications”. In: *2020 IEEE Sensors*. IEEE. 2020, pp. 1–4.

[13] Loïg Kergoat et al. “Advances in organic transistor-based biosensors: from organic electrochemical transistors to electrolyte-gated organic field-effect transistors”. In: *Analytical and bioanalytical chemistry* 402.5 (2012), pp. 1813–1826.

[14] Magnus Berggren and Agneta Richter-Dahlfors. “Organic bioelectronics”. In: *Advanced Materials* 19.20 (2007), pp. 3201–3213.

[15] Valentina Benfenati et al. “A transparent organic transistor structure for bidirectional stimulation and recording of primary neurons”. In: *Nature materials* 12.7 (2013), pp. 672–680.

[16] Monia Demelas et al. “An organic, charge-modulated field effect transistor for DNA detection”. In: *Sensors and Actuators B: Chemical* 171 (2012), pp. 198–203.

[17] Akifumi Kawamura and Takashi Miyata. “Biosensors”. In: *Biomaterials Nanoarchitectonics*. Elsevier, 2016, pp. 157–176.

[18] Piet Bergveld. “Thirty years of ISFETOLOGY: What happened in the past 30 years and what may happen in the next 30 years”. In: *Sensors and Actuators B: Chemical* 88.1 (2003), pp. 1–20.

[19] Alan D McNaught, Andrew Wilkinson, et al. “Compendium of chemical terminology. IUPAC recommendations”. In: (1997).

[20] Sergei V Dzyadevych et al. “Biosensors based on enzyme field-effect transistors for determination of some substrates and inhibitors”. In: *Analytical and bioanalytical chemistry* 377.3 (2003), pp. 496–506.

[21] Michael J Schöning and Arshak Poghossian. “Recent advances in biologically sensitive field-effect transistors (BioFETs)”. In: *Analyst* 127.9 (2002), pp. 1137–1151.

[22] Jeho Park et al. “Applications of field-effect transistor (FET)-type biosensors”. In: *Applied science and convergence technology* 23.2 (2014), pp. 61–71.

[23] Massimo Barbaro, Annalisa Bonfiglio, and Luigi Raffo. “A charge-modulated FET for detection of biomolecular processes: conception, modeling, and simulation”. In: *IEEE Transactions on Electron Devices* 53.1 (2005), pp. 158–166.

[24] Andreas Offenhäusser and Wolfgang Knoll. “Cell-transistor hybrid systems and their potential applications”. In: *TRENDS in Biotechnology* 19.2 (2001), pp. 62–66.

[25] Qingjun Liu et al. “Cell-based biosensors and their application in biomedicine”. In: *Chemical reviews* 114.12 (2014), pp. 6423–6461.

[26] Baozhen Chen, Archana Parashar, and Santosh Pandey. “Folded floating-gate CMOS biosensor for the detection of charged biochemical molecules”. In: *IEEE Sensors Journal* 11.11 (2011), pp. 2906–2910.

[27] Dion Khodagholy et al. “In vivo recordings of brain activity using organic transistors”. In: *Nature communications* 4.1 (2013), pp. 1–7.

[28] Piet Bergveld. “Development of an ion-sensitive solid-state device for neurophysiological measurements”. In: *IEEE Transactions on Biomedical Engineering* 1 (1970), pp. 70–71.

[29] Matti Kaisti, Qi Zhang, and Kalle Levon. “Compact model and design considerations of an ion-sensitive floating gate FET”. In: *Sensors and Actuators B: Chemical* 241 (2017), pp. 321–326.

[30] Jaebin Choi et al. “Field-Effect Biosensors for On-Site Detection: Recent Advances and Promising Targets”. In: *Advanced healthcare materials* 6.20 (2017), p. 1700796.

[31] Matti Kaisti et al. “An ion-sensitive floating gate FET model: operating principles and electrofluidic gating”. In: *IEEE Transactions on Electron Devices* 62.8 (2015), pp. 2628–2635.

[32] Peng Lin et al. “The application of organic electrochemical transistors in cell-based biosensors”. In: *Advanced Materials* 22.33 (2010), pp. 3655–3660.

[33] Denjung Wang, Vincent Noël, and Benoît Piro. “Electrolytic gated organic field-effect transistors for application in biosensors—A Review”. In: *Electronics* 5.1 (2016), p. 9.

[34] Matti Kaisti. “Detection principles of biological and chemical FET sensors”. In: *Biosensors and Bioelectronics* 98 (2017), pp. 437–448.

[35] Simon M Sze and Kwok K Ng. *Physics of semiconductor devices*. John wiley & sons, 2006.

[36] Tanu Wadhera et al. “Recent Advances and Progress in Development of the Field Effect Transistor Biosensor: A Review”. In: *Journal of Electronic Materials* 48.12 (2019), pp. 7635–7646.

[37] U Guth et al. “Solid-state reference electrodes for potentiometric sensors”. In: *Journal of Solid State Electrochemistry* 13.1 (2009), pp. 27–39.

[38] György Inzelt, Andrzej Lewenstam, and Fritz Scholz. *Handbook of reference electrodes*. Vol. 541. Springer, 2013.

[39] Miao Yuqing, Guan Jianguo, and Chen Jianrong. “Ion sensitive field effect transducer-based biosensors”. In: *Biotechnology advances* 21.6 (2003), pp. 527–534.

[40] MJ Milgrew, PA Hammond, and DRS Cumming. “The development of scalable sensor arrays using standard CMOS technology”. In: *Sensors and Actuators B: Chemical* 103.1-2 (2004), pp. 37–42.

[41] JIŘÍ Janata and St D Moss. “Chemically sensitive field-effect transistors.” In: *Biomedical engineering* 11.7 (1976), pp. 241–245.

[42] J.F. Schenck and Peter W Cheung. *in Theory, design, and biomedical applications of solid state chemical sensors*. CRC Press, 1978, pp. 165–173.

[43] Steve Caras and Jiri Janata. “Field effect transistor sensitive to penicillin”. In: *Analytical Chemistry* 52.12 (1980), pp. 1935–1937.

[44] DT Jobling, JG Smith, and HV Wheal. “Active microelectrode array to record from the mammalian central nervous systemin vitro”. In: *Medical and biological engineering and computing* 19.5 (1981), pp. 553–560.

[45] J van der Spiegel et al. “The extended gate chemically sensitive field effect transistor as multispecies microprobe”. In: *Sensors and Actuators* 4 (1983), pp. 291–298.

[46] L Bousse, J Shott, and JD Meindl. “A process for the combined fabrication of ion sensors and CMOS circuits”. In: *IEEE Electron Device Letters* 9.1 (1988), pp. 44–46.

[47] Peter Fromherz et al. “A neuron-silicon junction: a Retzius cell of the leech on an insulated-gate field-effect transistor”. In: *Science* 252.5010 (1991), pp. 1290–1293.

[48] S Schütz et al. “Field effect transistor-insect antenna junction”. In: (1997).

[49] E Souteyrand et al. “Direct detection of the hybridization of synthetic homo-oligomer DNA sequences by field effect”. In: *The Journal of Physical Chemistry B* 101.15 (1997), pp. 2980–2985.

[50] Dong-Sun Kim et al. “Fabrication and characteristics of a field effect transistor-type charge sensor for detecting deoxyribonucleic acid sequence”. In: *Japanese journal of applied physics* 42.6S (2003), p. 4111.

[51] Kanishk Singh et al. “Super Nernstian pH response and enzyme-free detection of glucose using sol-gel derived RuOx on PET flexible-based extended-gate field-effect transistor”. In: *Sensors and Actuators B: Chemical* 298 (2019), p. 126837.

[52] Chia-Ming Yang et al. “Low cost and flexible electrodes with NH3 plasma treatments in extended gate field effect transistors for urea detection”. In: *Sensors and Actuators B: Chemical* 187 (2013), pp. 274–279.

[53] Jia-Chyi Chen et al. “Portable urea biosensor based on the extended-gate field effect transistor”. In: *Sensors and actuators B: Chemical* 91.1-3 (2003), pp. 180–186.

[54] Mathieu Odijk et al. “Microfabricated solid-state ion-selective electrode probe for measuring potassium in the living rodent brain: Compatibility with DC-EEG recordings to study spreading depression”. In: *Sensors and Actuators B: Chemical* 207 (2015), pp. 945–953.

[55] Themistoklis Prodromakis, Yan Liu, and Chris Toumazou. “A low-cost disposable chemical sensing platform based on discrete components”. In: *IEEE electron device letters* 32.3 (2011), pp. 417–419.

[56] T Prodromakis et al. “A novel design approach for developing chemical sensing platforms using inexpensive technologies”. In: *2011 IEEE Biomedical Circuits and Systems Conference (BioCAS)*. IEEE. 2011, pp. 369–372.

[57] Chao Bian et al. “A field effect transistor (FET)-based immunosensor for detection of HbA1c and Hb”. In: *Biomedical microdevices* 13.2 (2011), pp. 345–352.

[58] Massimo Barbaro et al. “Fully electronic DNA hybridization detection by a standard CMOS biochip”. In: *Sensors and Actuators B: Chemical* 118.1-2 (2006), pp. 41–46.

[59] Massimo Barbaro et al. “Active devices based on organic semiconductors for wearable applications”. In: *IEEE Transactions on Information Technology in Biomedicine* 14.3 (2010), pp. 758–766.

[60] Ben Zhao et al. “Floating-Gate Ion Sensitive Field-Effect Transistor for Chemical and Biological Sensing”. In: *MRS Online Proceedings Library Archive* 828 (2004).

[61] Qi Zhang et al. “Polyaniline-functionalized ion-sensitive floating-gate FETs for the on-chip monitoring of peroxidase-catalyzed redox reactions”. In: *Electrochimica Acta* 261 (2018), pp. 256–264.

[62] Andreas Offenhäusser, Jürgen Rühe, and Wolfgang Knoll. “Neuronal cells cultured on modified microelectronic device surfaces”. In: *Journal of Vacuum Science & Technology A: Vacuum, Surfaces, and Films CONF- 1*. Vol. 13. 5. American Vacuum Society. 1995, pp. 2606–2612.

[63] Ariel Cohen et al. “Depletion type floating gate p-channel MOS transistor for recording action potentials generated by cultured neurons”. In: *Biosensors and Bioelectronics* 19.12 (2004), pp. 1703–1709.

[64] Krishna Jayant et al. “Non-Faradaic Electrochemical Detection of Exocytosis from Mast and Chromaffin Cells Using Floating-Gate MOS Transistors”. In: *Scientific reports* 5.1 (2015), pp. 1–15.

[65] Jin-Kwon Park et al. “SOI dual-gate ISFET with variable oxide capacitance and channel thickness”. In: *Solid-state electronics* 97 (2014), pp. 2–7.

[66] Carlos Duarte-Guevara et al. “Characterization of a 1024× 1024 DG-BioFET platform”. In: *Sensors and Actuators B: Chemical* 250 (2017), pp. 100–110.

[67] Henry S White, Gregg P Kittlesen, and Mark S Wrighton. “Chemical derivatization of an array of three gold microelectrodes with polypyrrole: fabrication of a molecule-based transistor”. In: *Journal of the American Chemical Society* 106.18 (1984), pp. 5375–5377.

[68] Takao Someya et al. “Integration and response of organic electronics with aqueous microfluidics”. In: *Langmuir* 18.13 (2002), pp. 5299–5302.

[69] Raúl José Martín-Palma and José Martínez-Duart. “Novel Advanced Nanomaterials and Devices for Nanoelectronics and Photonics”. In: *Nanotechnology for Microelectronics and Photonic*. Elsevier, 2017, pp. 243–263.

[70] Stefano Lai et al. “Ultralow voltage, OTFT-based sensor for label-free DNA detection”. In: *Advanced Materials* 25.1 (2013), pp. 103–107.

[71] Piero Cosseddu et al. “Ultra-low voltage, organic thin film transistors fabricated on plastic substrates by a highly reproducible process”. In: *Applied Physics Letters* 100.9 (2012), p. 61.

[72] A Caboni et al. “Organic-based sensor for chemical detection in aqueous solution”. In: *Applied Physics Letters* 95.12 (2009), p. 253.

[73] Zheng-Tao Zhu et al. “Humidity sensors based on pentacene thin-film transistors”. In: *Applied Physics Letters* 81.24 (2002), pp. 4643–4645.

[74] David Nilsson et al. “Bi-stable and dynamic current modulation in electrochemical organic transistors”. In: *Advanced Materials* 14.1 (2002), pp. 51–54.

[75] Jeffrey T Mabeck and George G Malliaras. “Chemical and biological sensors based on organic thin-film transistors”. In: *Analytical and bioanalytical chemistry* 384.2 (2006), pp. 343–353.

[76] Caizhi Liao and Feng Yan. “Organic semiconductors in organic thin-film transistor-based chemical and biological sensors”. In: *Polymer reviews* 53.3 (2013), pp. 352–406.

[77] Elizabeth von Hauff. “The role of molecular structure and conformation in polymer electronics”. In: *Semiconductors and Semimetals*. Vol. 85. Elsevier, 2011, pp. 231–260.

[78] Daniel A Bernards, Róisín M Owens, and George G Malliaras. “Organic semiconductors in sensor applications”. In: (2008).

[79] Stefano Casalini et al. “Organic field-effect transistor for label-free dopamine sensing”. In: *Organic Electronics* 14.1 (2013), pp. 156–163.

[80] Michela Chiappalone, Valentina Pasquale, and Monica Frega. *In Vitro Neuronal Networks: From Culturing Methods to Neuro-Technological Applications*. Vol. 22. Springer, 2019.

[81] A Spanu et al. “A reference-less pH sensor based on an organic field effect transistor with tunable sensitivity”. In: *Organic Electronics* 48 (2017), pp. 188–193.

[82] Andrea Spanu et al. “A high-sensitivity tactile sensor based on piezoelectric polymer PVDF coupled to an ultra-low voltage organic transistor”. In: *Organic Electronics* 36 (2016), pp. 57–60.

[83] Alessandra Caboni et al. “Flexible organic thin-film transistors for pH monitoring”. In: *IEEE Sensors Journal* 9.12 (2009), pp. 1963–1970.

[84] Tsukuru Minamiki et al. “Accurate and reproducible detection of proteins in water using an extended-gate type organic transistor biosensor”. In: *Applied Physics Letters* 104.24 (2014), p. 243703.

[85] Matti Kaisti et al. “Hand-held transistor based electrical and multiplexed chemical sensing system”. In: *Acs Sensors* 1.12 (2016), pp. 1423–1431.

[86] Tsukuru Minamiki et al. “An organic field-effect transistor with an extended-gate electrode capable of detecting human immunoglobulin A”. In: *Analytical Sciences* 31.7 (2015), pp. 725–728.

[87] Samit Gupta et al. “Detection of clinically relevant levels of protein analyte under physiologic buffer using planar field effect transistors”. In: *Biosensors and Bioelectronics* 24.4 (2008), pp. 505–511.

[88] Byoung Sam Kang et al. “Electrical detection of immobilized proteins with ungated AlGaN/ GaN high-electron-mobility Transistors”. In: *Applied Physics Letters* 87.2 (2005), p. 023508.

[89] Yuji Wang et al. “Planar Field Effect Transistor Biosensors: Toward Single Molecular Detection and Clinical Applications”. In: *ECS Transactions* 61.4 (2014), p. 139.

[90] Georg Steinhoff et al. “Recording of cell action potentials with Al Ga N/ Ga N field-effect transistors”. In: *Applied Physics Letters* 86.3 (2005), p. 033901.

[91] Leanne Friedrich and Dirk Gillespie. “Improving charge-sensitive biomolecule sensors with the right choice of electrolyte”. In: *Sensors and Actuators B: Chemical* 230 (2016), pp. 281–288.

[92] Arshak Poghossian et al. “Possibilities and limitations of label-free detection of DNA hybridization with field-effect-based devices”. In: *Sensors and Actuators B: Chemical* 111 (2005), pp. 470–480.

[93] Michael J Schöning et al. “Miniaturization of potentiometric sensors using porous silicon microtechnology”. In: *Electrochimica Acta* 42.20-22 (1997), pp. 3185–3193.

[94] CA Betty et al. “Macroporous silicon based capacitive affinity sensor—fabrication and electrochemical studies”. In: *Sensors and Actuators B: Chemical* 97.2-3 (2004), pp. 334–343.

[95] O Meskini et al. “Porous silicon as functionalized material for immunosensor application”. In: *Talanta* 71.3 (2007), pp. 1430–1433.

[96] Chang-Hoon Kim et al. “Novel dielectric modulated field-effect transistor for label-free DNA detection”. In: *Biochip J* 2.2 (2008), pp. 127–134.

[97] Chang-Hoon Kim et al. “Label-free DNA detection with a nanogap embedded complementary metal oxide semiconductor”. In: *Nanotechnology* 22.13 (2011), p. 135502.

[98] Hyungsoon Im et al. “A dielectric-modulated field-effect transistor for biosensing”. In: *Nature nanotechnology* 2.7 (2007), p. 430.

[99] Aurelia Magdalena Pisoschi. “Biosensors as bio-based materials in chemical analysis: a review”. In: *Journal of Biobased Materials and Bioenergy* 7.1 (2013), pp. 19–38.

[100] Anqi Zhang and Charles M Lieber. “Nano-bioelectronics”. In: *Chemical reviews* 116.1 (2016), pp. 215–257.

[101] Yu Chen et al. “Nanoscale field effect transistor for biomolecular signal amplification”. In: *Applied Physics Letters* 91.24 (2007), p. 243511.

[102] Roey Elnathan et al. “Biorecognition layer engineering: overcoming screening limitations of nanowire-based FET devices”. In: *Nano letters* 12.10 (2012), pp. 5245–5254.

[103] Shengbo Sang et al. “Progress of new label-free techniques for biosensors: a review”. In: *Critical reviews in biotechnology* 36.3 (2016), pp. 465–481.

[104] Jong-in Hahm and Charles M Lieber. “Direct ultrasensitive electrical detection of DNA and DNA sequence variations using nanowire nanosensors”. In: *Nano letters* 4.1 (2004), pp. 51–54.

[105] Kenzo Maehashi et al. “Aptamer-based label-free immunosensors using carbon nanotube field-effect transistors”. In: *Electroanalysis: An International Journal Devoted to Fundamental and Practical Aspects of Electroanalysis* 21.11 (2009), pp. 1285–1290.

[106] Yi Cui et al. “Nanowire nanosensors for highly sensitive and selective detection of biological and chemical species”. In: *science* 293.5533 (2001), pp. 1289–1292.

[107] Maria Teresa Martínez et al. “Label-free DNA biosensors based on functionalized carbon nanotube field effect transistors”. In: *Nano letters* 9.2 (2009), pp. 530–536.

[108] Xiaochen Dong et al. “Electrical detection of DNA hybridization with single-base specificity using transistors based on CVD-grown graphene sheets”. In: *Advanced Materials* 22.14 (2010), pp. 1649–1653.

[109] Yasuhide Ohno et al. “Electrolyte-gated graphene field-effect transistors for detecting pH and protein adsorption”. In: *Nano letters* 9.9 (2009), pp. 3318–3322.

[110] Nihar Mohanty and Vikas Berry. “Graphene-based single-bacterium resolution biodevice and DNA transistor: interfacing graphene derivatives with nanoscale and microscale biocomponents”. In: *Nano letters* 8.12 (2008), pp. 4469–4476.

[111] Allen J Bard et al. *Electrochemical methods: fundamentals and applications*. Vol. 2. wiley New York, 1980.

[112] H Von Helmholtz. “Studien über electrische Grenzschichten”. In: *Annalen der Physik* 243.7 (1879), pp. 337–382.

[113] REG Van Hal, Jan CT Eijkel, and Piet Bergveld. “A novel description of ISFET sensitivity with the buffer capacity and double-layer capacitance as key parameters”. In: *Sensors and Actuators B: Chemical* 24.1-3 (1995), pp. 201–205.

[114] Jacob N Israelachvili. *Intermolecular and surface forces*. Academic press, 2011.

[115] MW Dashiell et al. “The electrical effects of DNA as the gate electrode of MOS transistors”. In: *Proceedings. IEEE Lester Eastman Conference on High Performance Devices*. IEEE. 2002, pp. 259–264.

[116] Jürgen Fritz et al. “Electronic detection of DNA by its intrinsic molecular charge”. In: *Proceedings of the National Academy of sciences* 99.22 (2002), pp. 14142–14146.

[117] Dong-Sun Kim et al. “An FET-type charge sensor for highly sensitive detection of DNA sequence”. In: *Biosensors and Bioelectronics* 20.1 (2004), pp. 69–74.

[118] Massimo Barbaro et al. “Label-free, direct DNA detection by means of a standard CMOS electronic chip”. In: *Sensors and Actuators B: Chemical* 171 (2012), pp. 148–154.

[119] Chengwu Tao et al. “A novel floating-gate biosensing device with controlled charge-modulation”. In: *2007 IEEE/NIH Life Science Systems and Applications Workshop*. IEEE. 2007, pp. 257–260.

[120] NY-M Shen et al. “Charge-based chemical sensors: a neuromorphic approach with chemoreceptive neuron MOS (C/spl nu/MOS) transistors”. In: *IEEE Transactions on Electron Devices* 50.10 (2003), pp. 2171–2178.

[121] Chuan Gao et al. “A disposable polymer field effect transistor (FET) for pH measurement”. In: *TRANSDUCERS’03. 12th International Conference on Solid-State Sensors, Actuators and Microsystems. Digest of Technical Papers (Cat. No. 03TH8664)*. Vol. 2. IEEE. 2003, pp. 1172–1175.

[122] Andrea Loi, Ileana Manunza, and Annalisa Bonfiglio. “Flexible, organic, ion-sensitive field-effect transistor”. In: *Applied Physics Letters* 86.10 (2005), p. 103512.

[123] K Diallo et al. “Flexible pentacene ion sensitive field effect transistor with a hydrogenated silicon nitride surface treated Parylene top gate insulator”. In: *Applied Physics Letters* 93.18 (2008), p. 403.

[124] Tsukuru Minamiki et al. “Antibody-and label-free phosphoprotein sensor device based on an organic transistor”. In: *Analytical chemistry* 88.2 (2016), pp. 1092–1095.

[125] Tsukuru Minamiki et al. “Label-free detection of human glycoprotein (CgA) using an extended-gated organic transistor-based immunosensor”. In: *Sensors* 16.12 (2016), p. 2033.

[126] Wei Tang et al. “Low-voltage pH sensor tag based on all solution processed organic field-effect transistor”. In: *IEEE Electron Device Letters* 37.8 (2016), pp. 1002–1005.

[127] Jian Song et al. “Extended Solution Gate OFET-Based Biosensor for Label-Free Glial Fibrillary Acidic Protein Detection with Polyethylene Glycol-Containing Bioreceptor Layer”. In: *Advanced functional materials* 27.20 (2017), p. 1606506.

[128] Scott P White, Kevin D Dorfman, and C Daniel Frisbie. “Label-free DNA sensing platform with low-voltage electrolyte-gated transistors”. In: *Analytical chemistry* 87.3 (2015), pp. 1861–1866.

[129] Scott P White et al. “Rapid, selective, label-free aptameric capture and detection of ricin in potable liquids using a printed floating gate transistor”. In: *ACS Sensors* 1.10 (2016), pp. 1213–1216.

[130] Mathew S Thomas et al. “Interfacial Charge Contributions to Chemical Sensing by Electrolyte-Gated Transistors with Floating Gates”. In: *The journal of physical chemistry letters* 9.6 (2018), pp. 1335–1339.

[131] Byoung Sam Kang et al. “Electrical detection of deoxyribonucleic acid hybridization with Al Ga N/ Ga N high electron mobility transistors”. In: *Applied Physics Letters* 89.12 (2006), p. 122102.

[132] Wayne U Wang et al. “Label-free detection of small-molecule–protein interactions by using nanowire nanosensors”. In: *Proceedings of the National Academy of Sciences* 102.9 (2005), pp. 3208–3212.

[133] Gengfeng Zheng et al. “Multiplexed electrical detection of cancer markers with nanowire sensor arrays”. In: *Nature biotechnology* 23.10 (2005), pp. 1294–1301.

[134] Chao Li et al. “Complementary detection of prostate-specific antigen using In2O3 nanowires and carbon nanotubes”. In: *Journal of the American Chemical Society* 127.36 (2005), pp. 12484–12485.

[135] Xuejin Wen et al. “AlGaN/GaN HFET biosensors working at subthreshold regime for sensitivity enhancement”. In: *physica status solidi c* 8.7-8 (2011), pp. 2489–2491.

[136] Hee Ho Lee et al. “AlGaN/GaN high electron mobility transistor-based biosensor for the detection of C-reactive protein”. In: *Sensors* 15.8 (2015), pp. 18416–18426.

[137] Hee Ho Lee et al. “Fabrication and Characterization of an Extended-Gate AlGaN/GaN-Based Heterostructure Field-Effect Transistor-Type Biosensor for Detecting Immobilized Streptavidin-Biotin Protein Complexes”. In: *Sensors and Materials* 27.7 (2015), pp. 575–583.

[138] M Castellarnau et al. “Integrated cell positioning and cell-based ISFET biosensors”. In: *Sensors and Actuators B: Chemical* 120.2 (2007), pp. 615–620.

[139] Paul Horowitz and Winfield Hill. *The art of electronics*. Cambridge Univ. Press, 1989.

[140] Krishna Jayant et al. “Programmable ion-sensitive transistor interfaces. II. Biomolecular sensing and manipulation”. In: *Physical Review E* 88.1 (2013), p. 012802.

[141] S Mitra, AK Shukla, and S Sampath. “Electrochemical capacitors with plasticized gel-polymer electrolytes”. In: *Journal of power sources* 101.2 (2001), pp. 213–218.

[142] Krishna Jayant et al. “Programmable ion-sensitive transistor interfaces. I. Electrochemical gating”. In: *Physical Review E* 88.1 (2013), p. 012801.

[143] Prashant N Kambali and Ashok Kumar Pandey. “Capacitance and force computation due to direct and fringing effects in MEMS/NEMS arrays”. In: *IEEE Sensors Journal* 16.2 (2015), pp. 375–382.

[144] PM Faia, CS Furtado, and AJ Ferreira. “Humidity sensing properties of a thick-film titania prepared by a slow spinning process”. In: *Sensors and Actuators B: Chemical* 101.1-2 (2004), pp. 183–190.

[145] Jian Z Chen et al. “Capacitive sensing of droplets for microfluidic devices based on thermocapillary actuation”. In: *Lab on a Chip* 4.5 (2004), pp. 473–480.

[146] Pantelis Georgiou and Christofer Toumazou. “ISFET characteristics in CMOS and their application to weak inversion operation”. In: *Sensors and Actuators B: Chemical* 143.1 (2009), pp. 211–217.

[147] Stefano Lai, Massimo Barbaro, and Annalisa Bonfiglio. “Tailoring the sensing performances of an OFET-based biosensor”. In: *Sensors and Actuators B: Chemical* 233 (2016), pp. 314–319.

[148] Yen-Heng Lin et al. “Extended-gate field-effect transistor packed in micro channel for glucose, urea and protein biomarker detection”. In: *Biomedical microdevices* 17.6 (2015), p. 111.

[149] Chang-Soo Lee, Sang Kyu Kim, and Moonil Kim. “Ion-sensitive field-effect transistor for biological sensing”. In: *Sensors* 9.9 (2009), pp. 7111–7131.

[150] Jaume Segura and Charles F Hawkins. *CMOS electronics: how it works, how it fails*. John Wiley & Sons, 2004.

[151] Gerson Florence, Tiago Pereira, and Jürgen Kurths. “Extracellular potassium dynamics in the hyperexcitable state of the neuronal ictal activity”. In: *Communications in Nonlinear Science and Numerical Simulation* 17.12 (2012), pp. 4700–4706.

[152] Feng Yan et al. “Label-free DNA sensor based on organic thin film transistors”. In: *Biosensors and Bioelectronics* 24.5 (2009), pp. 1241–1245.

[153] Rosemary Smith, Robert J Huber, and JiŘÍ Janata. “Electrostatically protected ion sensitive field effect transistors”. In: *Sensors and Actuators* 5.2 (1984), pp. 127–136.

[154] Sergio Martinoia et al. “Development of ISFET array-based microsystems for bioelectrochemical measurements of cell populations”. In: *Biosensors and Bioelectronics* 16.9-12 (2001), pp. 1043–1050.

[155] Boon Chong Cheah et al. “An integrated circuit for chip-based analysis of enzyme kinetics and metabolite quantification”. In: *IEEE transactions on biomedical circuits and systems* 10.3 (2016), pp. 721–730.

[156] Nicolas Moser et al. “Mechanisms for enhancement of sensing performance in CMOS ISFET arrays using reactive ion etching”. In: *Sensors and Actuators B: Chemical* 292 (2019), pp. 297–307.

[157] Jae-Hyuk Ahn et al. “A nanogap-embedded nanowire field effect transistor for sensor applications: Immunosensor and humidity sensor”. In: *Proceedings of the 14th International Conference on Miniaturized Systems for Chemistry and Life Sciences*. 2010.

[158] Carmen Bartic et al. “Monitoring pH with organic-based field-effect transistors”. In: *Sensors and Actuators B: Chemical* 83.1-3 (2002), pp. 115–122.

[159] Zin-Sig Kim et al. “Biotin-functionalized semiconducting polymer in an organic field effect transistor and application as a biosensor”. In: *Sensors* 12.8 (2012), pp. 11238–11248.

[160] Min-Ho Park et al. “Mechanism of label-free DNA detection using the floating electrode on pentacene thin film transistor”. In: *The Journal of Physical Chemistry C* 120.9 (2016), pp. 4854–4859.

[161] Hao Tang et al. “Highly sensitive dopamine biosensors based on organic electrochemical transistors”. In: *Biosensors and Bioelectronics* 26.11 (2011), pp. 4559–4563.

[162] Corrado Napoli et al. “Electronic Detection of DNA Hybridization by Coupling Organic Field-Effect Transistor-Based Sensors and Hairpin-Shaped Probes”. In: *Sensors* 18.4 (2018), p. 990.

[163] Qi Zhang et al. “Surface functionalization of ion-sensitive floating-gate field-effect transistors with organic electronics”. In: *IEEE Transactions on Electron Devices* 62.4 (2015), pp. 1291–1298.

[164] Matti Kaisti et al. “Low-cost chemical sensing platform with organic polymer functionalization”. In: *IEEE Electron Device Letters* 36.8 (2015), pp. 844–846.

[165] Michael J Schöning et al. “Capacitive microsensors for biochemical sensing based on porous silicon technology”. In: *Sensors and Actuators B: Chemical* 64.1-3 (2000), pp. 59–64.

[166] Koen Besteman et al. “Enzyme-coated carbon nanotubes as single-molecule biosensors”. In: *Nano letters* 3.6 (2003), pp. 727–730.

[167] Jun Okuno et al. “Label-free immunosensor for prostate-specific antigen based on single-walled carbon nanotube array-modified microelectrodes”. In: *Biosensors and Bioelectronics* 22.9-10 (2007), pp. 2377–2381.

[168] Byeongju Kim et al. “DNA sensors based on CNT-FET with floating electrodes”. In: *Sensors and Actuators B: Chemical* 169 (2012), pp. 182–187.

[169] Priscilla Kailian Ang et al. “Flow sensing of single cell by graphene transistor in a microfluidic channel”. In: *Nano letters* 11.12 (2011), pp. 5240–5246.

[170] Yinxi Huang et al. “Graphene-based biosensors for detection of bacteria and their metabolic activities”. In: *Journal of Materials Chemistry* 21.33 (2011), pp. 12358–12362.